Dissertation

submitted to the

Combined Faculties of the Natural Sciences and Mathematics

of the Ruperto-Carola-University of Heidelberg, Germany

for the degree of

Doctor of Natural Science

Put forward by

Diplom-Physiker Mathias Zechmeister

born in: Wippra, Germany

Oral Examination: 2nd February 2011

Precision Radial Velocity Surveys for Exoplanets

Referees: Prof. Dr. Thomas Henning

Prof. Dr. Joachim Wambsganß

Abstract

Since the 90s astronomers have discovered around 500 extrasolar planets. Most of them have been found with the radial velocity method. In this work we present our precision radial velocity measurements for a sample of 40 M dwarfs and 30 solar-like stars. The data sets originate from four different instruments (UVES, CES+LC, CES+VLC, and HARPS) and are investigated for indications of planets. We perform several statistical tests for excess-variability, long-term trends, and periodicities. For the latter purpose, we have developed further a commonly used period analysis tool, the so called Lomb-Scargle periodogram.

Our radial velocity precision of a few m/s is approximately sufficient for the aspired goals, namely the search for terrestrial planets in the habitable zones of M dwarfs and the search for Jupiter analogues around solar-like stars. We demonstrate this with mass upper limits. Our data analysis does not reveal any new planet, while we can confirm the two known planets around the solar-like stars ι Hor and HR 506 as well as the long-term trend for ε Ind A. Moreover, we were able to identify several binaries and one brown dwarf. Our results are in agreement with estimates for the frequency of Jupiter-like planets which is around 1% for M dwarfs and 10% for solar-like stars.

Zusammenfassung

Seit den 90-ziger Jahren haben Astronomen etwa 500 extrasolare Planeten entdeckt. Die meisten von Ihnen wurden mit der Radialgeschwindigkeits-Methode gefunden. In dieser Arbeit präsentieren wir unsere präzisen Radialgeschwindigkeitsmessungen für ein Sample von 40 M-Sternen und 30 sonnenähnlichen Sternen. Die Datensätze stammen von vier verschieden Instrumenten (UVES, CES+LC, CES+VLC, und HARPS) und werden auf Hinweise von Planeten untersucht. Dazu führen wir statistische Tests zu Exzessvariabilitäten, Langzeittrends und Periodizitäten durch. Für letzteren Zweck, haben wir ein häufig genutztes Werkzeug für die Periodenanalyse, das sogenannte Lomb-Scargle Periodogramm, weiterentwickelt.

Unsere Radialgeschwindigkeitsgenaukeit von wenigen m/s ist annähernd ausreichend für die angestrebten Ziele, nämlich die Suche nach terrestrischen Planeten in der habitablen Zone von M-Sternen und die Suche nach Jupiter-artigen Planeten um sonnenähnliche Sterne. Wir demonstrieren dies mit oberen Massengrenzen. Aus unserer Datenanalyse geht kein neuer Planet hervor, während wir die bereits bekannten Planeten für die sonnenähnlichen Sterne ι Hor und HR 506 sowie den Langzeittrend für ε Ind A bestätigen können. Darüber hinaus konnten wir einige Doppelsterne und einen Braunen Zwerg identfizieren. Unsere Ergebnisse stimmen mit den Erwartungen für die Häufigkeit von Jupiter-artigen Planeten überein, welche etwa 1% für M-Sterne und 10% für sonnenähnliche Sterne ist.

Contents

Chapter 1

Introduction

Discovering planets and new worlds has long been a dream of humankind inspiring people to undertake new enterprises. Overcoming old fashioned, anthropocentric world views like the geocentric system or seeing the Sun or the Milky Way as centres of the universe, the idea was at hand that planets may exist around other stars.

The history until the first discovery of an exo-planet is quite eventful and also accompanied by many false detections, e.g. there were early claims of planet detections around 61 Cyg by Strand (1943, 1957) or around Barnard's star by van de Kamp (1963) via astrometry. Later on however, they turned out to be spurious detections (Heintz, 1978). Struve (1952) proposed to use the radial velocity (RV) method to search for planets and outlined that it would be possible to find close-in, massive Jupiters with the precision available at that time ($\sim$200 m/s).

Campbell et al. (1988) noted for the binary star γ Cep (K0IV): "probable third body variation of 25 m/s amplitude, 2.7 yr period". Their precision RV measurements indicated probably for the first time a bona fide exoplanet. Later this team argued that stellar phenomena (rotational modulation of active regions) might be a more plausible explanation than a planetary companion (Walker et al., 1992), but finally Hatzes et al. (2003) reinforced the planetary hypothesis (see also Walker 2008 for a review). Noteworthy is also the RV detection of the companion to HD 114762 (F9V) with a planetary minimum mass (11 $M_{\rm Jup}$) by Latham et al. (1989). However, the authors themselves pointed out that this object is probably a brown dwarf which was later corroborated by an estimate of the stellar rotation axis (Cochran et al., 1991).

The first, widely accepted planet detection was around the pulsar PSR B1257+12 by Wolszczan & Frail (1992). It was an amazing discovery for four reasons: (i) The planet host is a neutron star. (ii) It is a planetary system with two planets[1]. (iii) The planet masses are only a few Earth masses. (iv) It was a very lucky detection. "Thanks" to a mechanical tracking problem of the 305 m Arecibo radio telescope in Puerto Rico, Wolszczan and his group were allocated time for a programme to search for pulsars off the galactic plane. Indeed, they found new pulsars and collected an unusually large number of pulse time-of-arrival observations to characterise them. The data set for PSR B1257+12 could not be explained with a pulsar model alone, but when accounting for two orbiting planets the signal was well described. So these planets were found as a by-product of a programme that did not aim to search for planets (Wolszczan, private communication, manuscript for Astronomy and Astrophysics Review in prep., editor Lissauer). So far only a second pulsar (PSR B1620-26, Thorsett et al. 1993; Backer et al. 1993) is known to host a planet. The progress in this field of pulsar timing is hampered by the requirements of extensive data sets and large radio telescopes in order to find planets with this method.

Nowadays, the detection of 51 Peg b by Mayor & Queloz (1995) is mostly referred to as the first exoplanet discovery. It is the first planet found around a solar-like star (G5V) and was immediately verified by an American group (Marcy & Butler, 1995; Marcy et al., 1997). 51 Peg b has an orbital period of just 4.2 d and a minimum mass of 0.47 $M_{\rm Jup}$. This was evidence that close-in Jovians, i.e. those planets proposed by Struve (1952) for search programmes, indeed exist. From then on, many similar

[1] Later a third planet (Wolszczan, 1994) and fourth unconfirmed object were announced in this system.

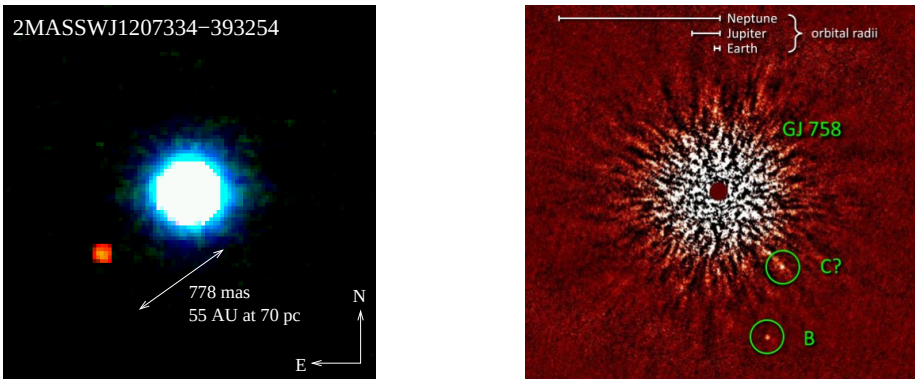

Figure 1.1: Examples for direct imaging detections. (Left) Planet to a brown dwarf (Chauvin et al., 2004). (Right) Putative planets of the solar-like star GJ 758 with a scale for the solar system (Thalmann et al., 2009).

objects have been found and belong to a class called hot Jupiters. These systems are very different from our solar system where Jupiter has an orbital period of 12.3 yr. The method, which Mayor & Queloz (1995) employed, was the radial velocity technique that measures the Doppler shift introduced by the gravitational pull of an orbiting companion (Sect. 1.2).

In October 2010, the exoplanet list[2] counts ∼500 planets and planet candidates which were discovered by the different methods briefly explained in Sect. 1.1. So far, the most successful technique is the RV method which has revealed more than 350 exoplanets. The RV technique is the basic method in this thesis and is explained in more detail in Sect.1.2.

1.1 Methods for exoplanet detection

1.1.1 Direct imaging

It is very challenging to directly image a planet orbiting around a star. One has to overcome the huge brightness contrast and the small angular separation between the bright star and the faint planet. Several techniques, such as coronography, nulling interferometry, or angular differential imaging, have been developed to solve the technical difficulties.

To enhance the detection probability astronomers have focussed on young, nearby systems, because in their early stages planets are relatively bright compared to their host stars. Indeed, some groups have successfully imaged some wide giant planets. Chauvin et al. (2004) imaged for the first time directly a 5 $M_{\rm Jup}$-mass planet accompanying a brown dwarf (Fig. 1.1). Another example is the substellar companion of the K dwarf GQ Lup which might have a planetary mass (Neuhäuser et al., 2005). Further exciting detections are the planet around the A3V star Fomalhaut (Kalas et al., 2008) and the planetary system to the A5V star HR 8799 (Marois et al., 2008). GJ 758 b is the first planet-like object imaged to a sun-like star (Thalmann et al., 2009) in a separation of only 29 AU and with a temperature of only 600 K. For HR 8799c Janson et al. (2010) demonstrated that even direct spectroscopy is possible. However, the mass estimates rely often on age estimates based on evolutionary models and, e.g., new asteroseismologic measurements indicate an older age for HR 8799 and imply that the imaged companions are brown dwarfs (Moya et al., 2010).

1.1.2 The transit method

The principle of the transit technique is well known, because it has been applied since almost hundred years to study eclipsing binary systems, and with today's photometric precision it is also applicable to

[2] `http://exoplanet.eu/`

study planets. The technique is easy to understand. If the orbit of a companion has such a favourable inclination ($i \approx 90°$) that the companion can cross the line of sight between the star and the observer, it blocks light of the star so that the star appears dimmer during this time. The process will occur repeatedly at intervals given by the orbital period and the light curve of the star exhibits periodically recurring dips (Fig. 1.2).

Since the first detection of a transiting planet by Charbonneau et al. (2000) around HD 209458, which was already known from RV measurements to harbour this planet, more than 100 transiting planets have been found. The Kepler mission, currently operating in space, has already revealed hundreds of candidates and, when they are confirmed, the number of transiting planets will increase considerably (Borucki & the Kepler Team, 2010). Thus the transit technique is very successfully and might soon overtake the RV method in number of planet detections.

The transit method is sensitive to very short period planets and usually requires confirmation by RV measurements[3] to exclude false positives, since e.g. grazing binaries or blend scenarios (eclipsing binary + background star) can mimic the transit light curves of planets. The application of the RV method to transiting planets is particularly interesting when used to measure the Rossiter-McLaughlin effect (Schlesinger, 1910; Rossiter, 1924; McLaughlin, 1924; Ohta et al., 2005). With this effect it is possible to investigate the alignment between the spin of the planetary orbit and the spin of the stellar rotation. The star must rotate for the Rossiter-McLaughlin effect to be measurable. Due to the rotation the stellar lines are rotationally broadened which is the contribution of the blue shifted and red shifted hemisphere of the star. When a planet crosses in front of the star, then it can be distinguished whether it occults first the blue shifted or the red shifted part leading to a distortion in the stellar line profile and an effective red or blue shift, respectively, in the RV of the star. Thus it is possible to reconstruct the path of the planet across the stellar disk. Since the effect scales with the stellar rotation velocity, rapidly rotating stars are more amenable for the Rossiter-McLaughlin effect and there are even systems where the Rossiter-McLaughlin amplitude is larger than the orbital amplitude (Anderson et al., 2010). Interestingly also, planets were found whose orbit is misaligned or even retrograde (e.g. Hébrard et al., 2008; Winn et al., 2010).

The fortunate case of transiting planets allow a determination of the radius and density of the planet from the transit parameters. Their densities can be as low as 0.13 g/cm^3, i.e. only 10% of the density of Jupiter (e.g. WASP-17b, Anderson et al., 2010), or as high as 9.6 g/cm^3 (e.g. Corot 7b, Guenther et al., 2010 and references therein; cf. the density of the Earth of 5.52 g/cm^3). The temperature of the planets can be derived and Knutson et al. (2007) even reconstructed a temperature map for the surface of the exoplanet HD 189733b.

Furthermore it is even possible to study the atmospheres of these hot Jupiters via transit spectroscopy. Several elements have been detected in their atmospheres, e.g. sodium (Na), water (H_2O), methane (CH_4), carbon dioxide (CO_2), or carbon monoxide (CO) (e.g. Charbonneau et al., 2002; Tinetti et al., 2007; Swain et al., 2008; Snellen et al., 2008). Snellen et al. (2010) reported even the detection of winds in the atmosphere of the exoplanet HD 209458 b via a blueshift of CO lines.

The transit community has also established the method of transit timing (e.g. Holman & Murray, 2005; Agol et al., 2005). If there are further planets in the system (or exomoons around the transiting planet, Simon et al., 2007), they may influence the time of transit centre due to their gravitational interaction. The effect of such Transit Time Variations (TTVs) is of the order of just a few seconds or minutes, i.e. only a fraction of the transit duration, and a large number of transits is required to detect TTVs. E.g. Lendl et al. (2010) or Maciejewski et al. (2010) announced to have found TTVs.

1.1.3 Astrometry

Astrometry is the oldest subfield of science (not only of astronomy). So far however, this method has not delivered a planet discovery, but lots of spurious detections. A recent example is the planet VB10b

[3]E.g. this is difficult for A stars which are not suitable for high precision RV measurements because they have only few and broad absorption lines. In some cases the planet hypothesis can be confirmed with spectroscopic line-profile tomography (Cameron et al., 2010a,b).

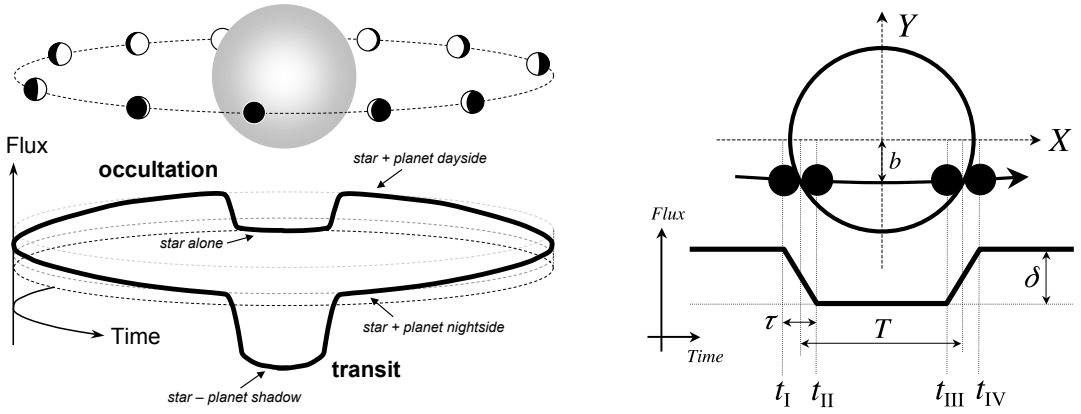

Figure 1.2: Basic principle of a transit. (Left) Flux as a periodic function of time (light curve). (Right) Basic transit parameters: the four contact points t_i, ingress/egress duration τ, transit duration T, and transit depth δ (from Winn, 2010).

(Pravdo & Shaklan, 2009), which was disproved with RV measurements in the near-infrared (Bean et al., 2010a).

Astrometry is more sensitive to long period planets, because the reflex displacement of the star is the larger the more distant the planet is (similar to a lever). This means that a long timebase is required to establish a significant signal. However, astrometry was able to provide helpful contributions by constraining the orbital inclinations i for a few known planetary systems (e.g. GJ 876, Benedict et al., 2002). For some systems the true mass of the planet candidates turned out to be in the brown dwarf or stellar regime (e.g. Bean et al., 2007). In the future, astrometric planet discoveries can be expected with the μas precision of the interferometric facilities such as PRIMA (Phase-Referenced Imaging and Microarcsecond Astrometry) or the planned GAIA (Global Astrometric Interferometer for Astrophysics) space mission.

1.1.4 Gravitational microlensing

Gravity can deflect light. This was suggested by Newton and correctly predicted by Einstein. Similar to the refractive characteristic of an optical lens, the gravitational field of a massive body can focus passing light from a background source depending on the geometric dimensions. At rare occasions, the Earth is close to such a focus and the source appears brighter than usual. The magnification

$$A(u) = \frac{u^2+2}{u\sqrt{u^2+4}}$$

depends on the angular seperation u between the lensing object and the source which is measured in terms of the angular Einstein ring given by

$$\theta_E = \sqrt{\frac{4GM_L}{c^2}\frac{d_S - d_L}{d_s d_L}}.$$

The Einstein ring is a characteristic scale for the geometric dimensions and is determined by the lensing mass M_L and the distance of the source d_S and lens d_L.

In the case of planet searches with microlensing the source is usually a background star in the galactic bulge of our galaxy, while a foreground star serves as the lens. If the lensing star has a planet, the additional gravitation of the planet acts as an imperfection of the lens leading to peculiarities in the light curve of the lensing event (see Wambsganss 2006 for a review).

About 11 planets were found by microlensing. OGLE 2003-BLG-235 was the first measured planetary microlensing event (Bond et al., 2004). Because each microlensing event is unique and unrepeatable,

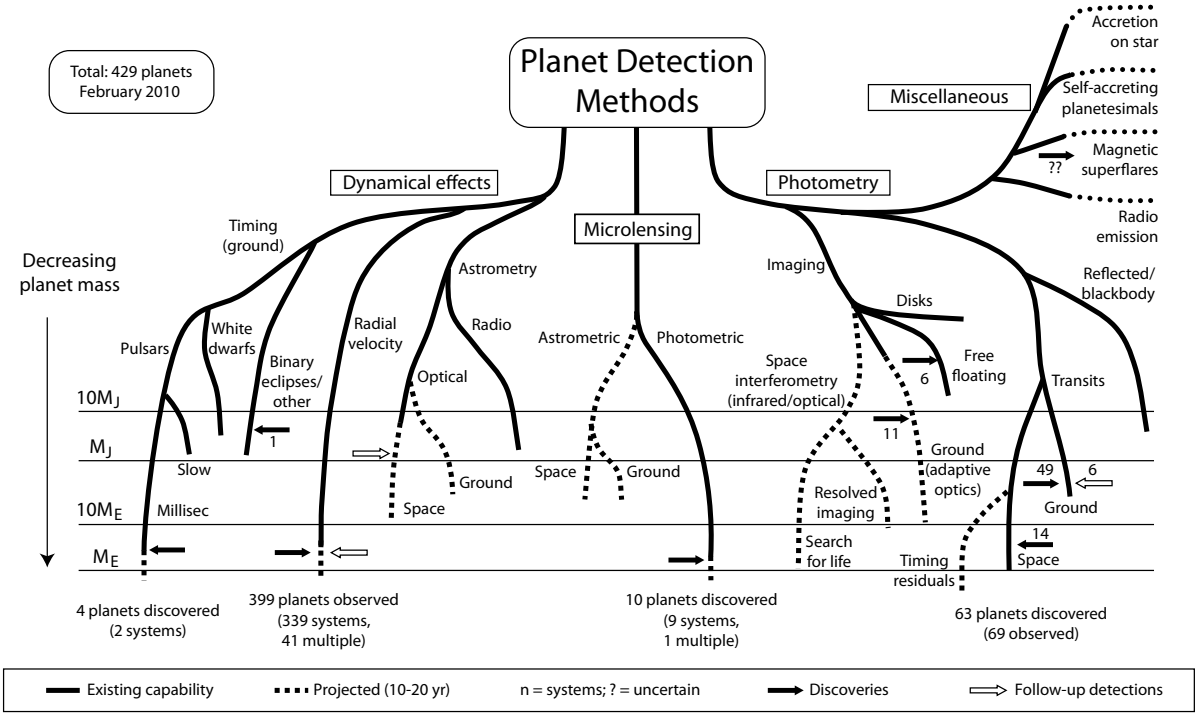

Figure 1.3: Overview of exoplanet detection methods their status and sensitivity (from Perryman).

follow-up observations are difficult. However, the method is sensitive to Earth-mass planets at seperations of 1–5 AU and contributes to the statistics of the planet frequency. The planetary system of OGLE-06-109L, with a Jupiter-like and a Saturn-like planet, constitutes an analogue of the solar system (Gaudi et al., 2008; Bennett et al., 2010), and three detected cool Super-Earths (3-10 $M_\oplus$) suggest that low mass planets are common (Gould et al., 2006). Microlensing has also the potential to detect exomoons (Liebig & Wambsganss, 2010) or even planets in other galaxies via "pixel lensing" (gravitational microlensing of unresolved stars, Gould 1996; Ingrosso et al. 2009).

1.1.5 Other methods

There are two more successful timing methods, besides the already mentioned transit and pulsar timing. Timing measurements of stellar pulsations revealed a 3 $M_{\rm Jup}$ object around the white dwarf V 391 Peg (Silvotti et al., 2007). The method of TTV (Sect. 1.1.2) can of course also be applied to eclipsing binaries and found two long-period Jupiters to the short-period eclipsing binary NN Ser (P=0.13 d, DAO1[4]–M4V) (Beuermann et al., 2010).

The structure of debris disks around stars allows us to come to conclusions about the presence of planets. Based on this argument Quillen & Thorndike (2002) presumed a planet around ε Eri. In the case of the directly imaged Fomalhaut b (Sect. 1.1.1), Kalas et al. (2008) argued that the dust belt structure constrains the planet mass to be at most three Jupiter masses.

There are further proposed methods which are less suited for planet searches but helpful to study them. E.g. searching for the star light reflected from the close-in hot Jupiter τ Tau b can put limits on the orbital inclination and on the planet albedo (e.g. Rodler et al. 2010, and references therein). Other groups try to detect the radio emission of exoplanets (Grießmeier et al., 2007) which is expected from

[4]Hydrogen-helium hybrid white dwarf. Spectral classification according to Sion et al. (1983): degenerated star D (white dwarf), primary spectral type A (only Balmer lines; no HeI or metals present), secondary spectral features O (strong HeII; HeI or H present), temperature index 1 ($T \sim 50\,000$K)

the interaction between strongly magnetised planets and stars (or stellar winds). Star-planet interaction (SPI) via tidal or magnetic effects may also lead to observable features on the stellar surface and induces chromospheric stellar activity (Shkolnik et al., 2003) similar to the plasma torus in the Jupiter-Io system.

Figure 1.3 gives a schematic overview of the different planet detection methods and their sensitivities. The methods are grouped in the three main branches: dynamical effects, microlensing, and photometry. We see that the RV technique is so far the most successful method and several methods (pulsar timing, RV, microlensing, and transits) have the potential to detect Earth-mass planets.

1.2 The radial velocity method

The radial velocity (RV) method has become a standard technique in exoplanet search. Actually, it is an old technique that has been employed since already one hundred years to study binaries by originally recording their spectra on photographic plates. Benefiting from the invention of the CCD, the RV method has become sensitive enough since the 1990s to trace the effects of planets.

The RV method can be easily understood. Imagine, if a star has a companion, both bodies orbit around their common centre of mass. The star performs a reflex motion in three dimensional space and the trajectory $\vec{r}(t)$ is described by a Keplerian ellipse. The radial velocity is the projected component of the space velocity $\dot{\vec{r}}(t)$ onto the line of sight, i.e. the line between the observer and the star. By convention this line of sight determines the z-axis of our coordinate system and the radial velocity RV is simply given by $RV = \dot{z}$. The RV can be measured by the spectroscopic Doppler effect[5]

$$\frac{RV}{c} = \frac{\Delta\lambda}{\lambda} \tag{1.1}$$

where c is the speed of light and λ the rest wavelength. This means, when the source moves at a radial velocity RV, it causes a wavelength shift $\Delta\lambda$ to the spectrum. The object appears blue-shifted, when it approaches the observer (RV<0) and red-shifted, when it recedes from the observer (RV>0).

The equation for the RV as a function of time (RV curve) for Keplerian orbits will be given later (Sect. 2.5, Eq. (2.28)). For now Fig. 1.4 gives an overview of the variety of possible RV curves which are described by six orbital parameters, namely the period P, eccentricity e, RV semi-amplitude K, longitude of periastron ω, time of periastron passage T_0, and system radial velocity γ. Vice versa from the shape of the measured RV curve we can derive these parameters by fitting the model function. However, the RV is just the one dimensional component of a motion that takes place in three dimensional space. Thus there remain ambiguities regarding the orientation of the ellipse, and we cannot derive from the RVs alone two other orbit parameters, namely the longitude of the ascending node Ω and the inclination i of the orbit.

The unknown inclination i is the drawback of the the Doppler method which therefore can provide only minimum masses. This is expressed by the so called mass function

$$f(m) = \frac{(m\sin i)^3}{(M+m)^2} = \frac{P}{2\pi G}(K\sqrt{1-e^2})^3$$

where M is the mass of the star and G the gravitational constant. While we can calculate the right-hand side of the mass function with the orbit parameters derived from the RV curve, we cannot solve this cubic equation for the true companion mass m without knowing i. However, we obtain a minimum mass $m_{\min}$ for $i = 90°$. Considering the large mass difference between planets and stars ($m \ll M$, i.e. $M+m \approx M$), the minimum mass can be simply written as $m_{\min} = m\sin i$.

In the case of an orbit seen edge-on ($i = 90°$) as in transiting systems, the true mass equals the minimum mass ($m_{\min} = m$). Contrariwise, for a nearly face-on orbit the true mass can be much higher (by

[5]There is also a photometric Doppler effect (aka. Doppler boosting or Doppler beaming). When a source moves towards the observer, it appears brighter, because the source runs behind the radiated light and seems to emit the light at a higher rate. With the precision of the Kepler space telescope it was already possible to detect this effect in some binary systems having high orbital velocities (e.g. van Kerkwijk et al. 2010, Bloemen et al. 2010 and references therein, RV precision ∼km/s).

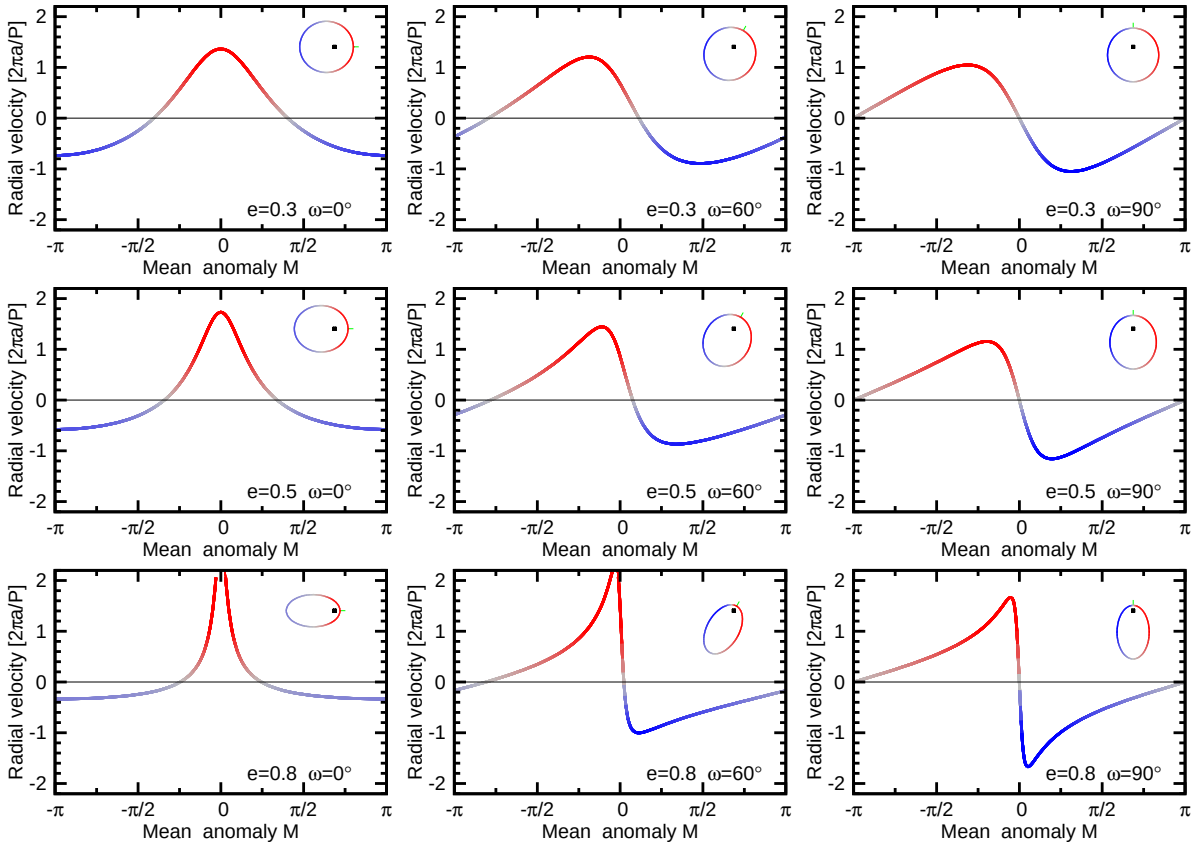

Figure 1.4: A sample of theoretical radial velocity curves. In the case of circular orbits ($e = 0$, not shown) the RV curve is sinusoidal. The more eccentric the orbit, the more asymmetric are the RV curves. Because the mean anomaly is defined as $M = 2\pi\frac{t-T_0}{P}$, $M = 0$ corresponds to the periastron passage (green tic). The embedded orbit in each panel indicates the shape, the orientation, and the focus of the ellipse (observer looks from the bottom axis; counterclockwise motion). Each orbit has the same semi-major axis a.

the factor of $\sim 1/\sin i$)[6]. Assuming geometrically random orientations, the probability for an inclination to be smaller than a threshold i_0 is (e.g. Kürster et al., 2008)

$$\text{Prob}(0 \leq i \leq i_0) = 1 - \cos i_0.$$

E.g. there is a 13% chance that the true mass exceeds twice the minimum mass (or $i < 30°$) and just a 3% chance for $m \geq 4 \cdot m_{\text{min}}$ (or $i < 14.5°$). Hence only in rare cases are the planetary minimum masses in the stellar regime (e.g. HD 33636 B, $m_{\text{min}} = 9.3 M_{\text{Jup}}$, $m = 0.14 M_{\odot}$, $i = 4°$, Bean et al., 2007).

1.2.1 Measuring precise radial velocities

To obtain precise RVs the challenge is to measure the wavelength shift $\Delta\lambda$ with a high precision. Spectrographs are usually employed for wavelength dependent flux measurements. They possess a grating or prism which disperses incident light and are characterised by the resolving power

$$R = \frac{\lambda}{\delta\lambda}$$

[6]Note that for low inclinations ($i \ll 90°$) the approximation $m \ll M$ might be not valid and one should solve the cubic form of mass function.

of the instrument. A simple estimate illustrates the required precision. If a spectrum is shifted by one resolution element, i.e. $\Delta\lambda = \delta\lambda$, this corresponds according to Eq. (1.1) to an RV shift of

$$\Delta RV = \frac{c}{R}.$$

E.g. in a high resolution spectrograph with $R = 100\,000$ the width of a resolution element corresponds to 3 km/s. Because one resolution element $\delta\lambda$ is usually sampled by 2–3 CCD pixels (pixel size $\sim 15\,\mu$m), the pixel width on the detector corresponds to 1–1.5 km/s. This means, if we aim at an RV precision of 1 m/s, we must be able to measure shifts of 1/1000 th of a pixel ($\sim$15 nm) and need *sub-pixel* accuracy in the data analysis!

Indeed this is possible, because the centroid positions of the stellar lines can be measured to a higher precision than their resolved line widths and many spectral lines are used to build a statistical RV average. Of course the RV precision also depends on the signal-to-noise ratio S/N of the spectrum. The situation is quite similar in astrometry where centroid positions are also measured more precisely than the width of the point spread function (PSF) depending on the S/N and the number of stars in the field. The RV precision, theoretically expected for photon noise, can be predicted with a simple equation which just depends on the spectrum and its intensity (Connes, 1985; Butler et al., 1996; Bouchy et al., 2001; see also Sect. 4.3.4).

Moreover, the stellar spectrum does never remain at the same position, even if a star does not change its intrinsic RV. Due to the barycentric velocity of the Earth of $\sim$29.8 km/s, two stellar spectra can be separated by up to 60 km/s over the course of half a year depending on the star's position on the sky. In our example above this shift corresponds to 20 resolution elements or roughly 40 CCD pixels. The maximum drift is 0.35 m/s/min, i.e. the barycentric effect can accumulate to a considerable amount during long exposures. There are routines which correct for the barycentric RV using the ephemerides of the Earth (Standish, 1990).

Over time the astronomers figured out many systematic error sources that limited the precision. It is important that the optical path is the same for the star light and the comparison source as demonstrated by Griffin & Griffin (1973). Wavelength shifts can arise, e.g., from mechanical instabilities or from pressure and temperature changes which influence the refractive index of the air and the structure of the optics and mechanics. Also inhomogeneities on the CCD can play a role (Butler et al., 1996).

The key to high RV precision is

- a very stable, high resolution spectrograph and/or
- a simultaneous wavelength calibration with a suitable spectrum and
- the same optical path for the stellar beam and the calibration source.

The HARPS spectrograph (La Silla, Chile) fulfils all requirements. It is embedded in a vacuum tank, i.e. in a temperature and pressure stabilised environment. It is so stable that one often waives a simultaneous calibration during a night[7].

The calibration process is important and two basic concepts have been developed for the simultaneous wavelength calibration which are briefly described below.

1.2.2 Self calibration with a gas absorption cell

Griffin & Griffin (1973) suggested to use the telluric lines of the Earth's atmosphere as a simultaneous reference spectrum to improve the RV precision. Before the star light enters the spectrograph, it passes the atmosphere containing natural gases, like water vapour, oxygen, or carbon dioxide, which imprint their absorption lines onto the stellar spectrum. The telluric lines are always recorded simultaneously;

[7]The second calibration fibre can then be used for a sky spectrum. It also avoids light cross-contamination from bright ThAr lines.

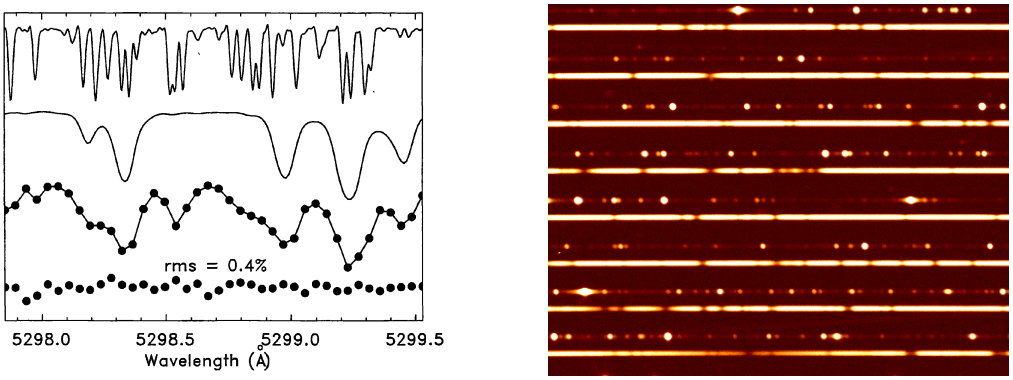

Figure 1.5: (Left) Principle of the iodine cell method (from Butler et al., 1996). Shown are the iodine spectrum with its sharp lines, the stellar template, the observed composite spectrum (dots) with the well-fitting model (solid line), and the enlarged residuals (from top to bottom). (Right) Section of a raw HARPS spectrum. The ThAr emission spectrum is recorded parallel to the stellar absorption spectrum in each Echelle order.

however they vary with the atmospheric conditions, especially with the wind speed which limits this technique to a typical precision of $\sim$20 m/s.

Campbell & Walker (1979) built a cell which was filled with hydrogen fluoride gas (HF). The sealed cell was placed in the stellar beam in front of the spectrograph and the HF absorption lines were superimposed onto the star light. In contrast to the telluric lines, the HF cell could be operated under controlled conditions ($T = 100°$C). HF is lethal and the cell had a length of 90 cm. The achieved precision was around 15 m/s (Campbell et al., 1988; Walker et al., 1995).

Later molecular iodine gas (I_2) was proposed and adapted as a calibration source (Beckers, 1976; Marcy & Butler, 1992). Iodine gas has a strong absorption coefficient (allowing for a short cell length of a few centimetres) and a high line density, and it is chemically stable and nonlethal. The principle of the method is shown in Fig. 1.5 (left). As outlined by Butler et al. (1996), the data modelling should invoke an overresolved iodine and stellar spectra which allow for a reconstruction of the instrumental line spread function (LSF). A highly resolved iodine spectrum can be obtained with a Fourier transform spectrometer (FTS), while the stellar template is constructed via deconvolution from a stellar spectrum taken without the cell.

The advantages of the absorption gas cell are the low costs and the long-term stability. The disadvantages are the complex data modelling, the short spectral coverage, and the lower efficiency due to the absorption ($\sim -50\%$). Moreover the science spectra are often useless for other scientific analysis, because the spectra are "contaminated" by the calibration lines. A precision of 3 m/s was widely demonstrated and also claims of 1 m/s precision were made (e.g. Vogt et al., 2010).

1.2.3 Simultaneous calibration with emission lamps

The first exoplanet 51 Peg b was detected with the ELODIE spectrograph of the Haute-Provence Observatory, France (Mayor & Queloz, 1995). The ELODIE spectrograph (Baranne et al., 1996) is a fibre fed Echelle spectrograph and uses a ThAr emission lamp for wavelength calibration. The same basic concept is also realised in the HARPS spectrograph (Mayor et al., 2003). Figure 1.5 (right) displays part of a raw HARPS frame. The ThAr spectrum is fed via a second fibre to the spectrograph and is recorded simultaneously and parallel to the science spectrum.

The ThAr lamp is often used, because it has many emission lines over a wide range (see Lovis & Pepe 2007 for a new ThAr line list). Not all lines are used for the calibration. The Ar lines are only stable to a few tens of m/s from lamp to lamp and exhibit significant ageing effects, because they are very sensitive to the pressure inside the lamp. Also lines with blends are excluded from the calibration.

Because also the Th lines suffer from ageing effects, special efforts must be made to correct for this (Mayor et al., 2009b). Since ThAr lamps have a finite lifetime, one strategy is to employ a rarely used master lamp to calibrate frequently used slave lamps.

The radial velocity is computed by a cross-correlation of the stellar spectrum with a numerical mask and corrected for the instrumental drift as measured with the second calibration fibre. The quoted RV precision of HARPS is 1 m/s or better (Lovis et al., 2006).

1.2.4 Other techniques

Besides the before mentioned calibration sources there are attempts to use interferometric facilities for the calibration. A precision of ~ 8 m/s was achieved with a Fabry-Perot etalon that can be placed into the light path in a way similar to using an iodine cell (Cochran et al., 1982; McMillan et al., 1990, 1994; Connes, 1985). Michelson interferometers were used for Doppler measurements of the Sun (Kozhevatov et al., 1995) and are currently under further development for exoplanet search (dispersed fixed-delay interferometry, Ge 2002). The latter discovered successfully an exoplanet (Ge et al., 2006).

The Fourier transform spectrometer (FTS) provides an accurate wavelength scale implying it is suitable for RV measurements. A FTS works similar to a Michelson interferometer where one arm length is tunable. In a first step, an interferogram is obtained by measuring the intensity as a function of the mirror path which can be moved over a large distance (~ 1 m). Second, the spectrum is computed via a numerical Fourier transform of the interferogram. The resolution depends on the scan length and the S/N on the scan duration. FTSs have an adjustable resolution and a simple, well-known instrumental profile. However, they are less efficient compared to conventional spectrographs. Combinations with dispersive elements are explored to improve the efficiency (Hajian et al., 2007). FTSs are also on board of the AKARI (FIS-FTS, Murakami et al. 2010) and HERSCHEL (SPIRE, Griffin et al. 2008) satellites.

Finally, it should be pointed out that radial velocities can also be measured without spectroscopy. With high-accuracy astrometry RVs can be derived from changing annual parallax, changing proper motion, or changing angular extent of a moving group of stars (Dravins et al., 1999)[8]. These are secular effects and current astrometry is not sufficient for precise RV measurements, but these methods provide estimates for absolute RVs independent of spectroscopic effects, such as line asymmetries, stellar convection, or gravitational redshift, which affect spectroscopically derived absolute RVs.

1.3 Outline of this work

This work concentrates on the analysis of real RV data to search for planets. In following chapters, we first develop further a period search tool which will play an important role in our data analysis. Then, we present two RV surveys. The precision of the RV data is well suitable for discovering planets, which is demonstrated by detection limits. The first survey includes a sample of 40 M dwarfs and aims at searching for terrestrial planets in the habitable zones of the stars. The second survey consists of 30 solar-like stars, and with the precision and timebase of the data sets we aim to detect Jupiter analogues.

The second and third chapter are already published in Astronomy and Astrophysics (Zechmeister & Kürster, 2009; Zechmeister et al., 2009). The forth chapter is close to submission.

[8]Likewise, we can derive astrometric quantities (product of distance and squared proper motion) from RV changes (see secular acceleration Sect. 3.3.1)

Chapter 2

The generalised Lomb-Scargle periodogram

A new formalism for the floating-mean and Keplerian periodograms

From Zechmeister & Kürster 2009, A&A, 496, 577

ABSTRACT: The Lomb-Scargle periodogram is a common tool in the frequency analysis of unequally spaced data equivalent to least-squares fitting of sine waves. We give an analytic solution for the generalisation to a full sine wave fit, including an offset and weights (χ^2 fitting). Compared to the Lomb-Scargle periodogram, the generalisation is superior as it provides more accurate frequencies, is less susceptible to aliasing, and gives a much better determination of the spectral intensity. Only a few modifications are required for the computation and the computational effort is similar. Our approach brings together several related methods that can be found in the literature, viz. the date-compensated discrete Fourier transform, the floating-mean periodogram, and the "spectral significance" estimator used in the SigSpec program, for which we point out some equivalences. Furthermore, we present an algorithm that implements this generalisation for the evaluation of the Keplerian periodogram that searches for the period of the best-fitting Keplerian orbit to radial velocity data. The systematic and non-random algorithm is capable of detecting eccentric orbits, which is demonstrated by two examples and can be a useful tool in searches for the orbital periods of exoplanets.

2.1 Introduction

The Lomb-Scargle periodogram (Scargle, 1982) is a widely used tool in period searches and frequency analysis of time series. It is equivalent to fitting sine waves of the form $y = a\cos\omega t + b\sin\omega t$. While standard fitting procedures require the solution of a set of linear equations for each sampled frequency, the Lomb-Scargle method provides an analytic solution and is therefore both convenient to use and efficient. The equation for the periodogram was given by Barning (1963), and also Lomb (1976) and Scargle (1982), who furthermore investigated its statistical behaviour, especially the statistical significance of the detection of a signal. For a time series (t_i, y_i) with zero mean ($\bar{y} = 0$), the Lomb-Scargle periodogram is defined as (normalisation from Lomb 1976):

$$\hat{p}(\omega) = \frac{1}{\hat{YY}}\left[\frac{\hat{YC}_{\hat{\tau}}^2}{\hat{CC}_{\hat{\tau}}} + \frac{\hat{YS}_{\hat{\tau}}^2}{\hat{SS}_{\hat{\tau}}}\right] \tag{2.1}$$

$$= \frac{1}{\sum_i y_i^2}\left\{\frac{[\sum_i y_i \cos\omega(t_i-\hat{\tau})]^2}{\sum_i \cos^2\omega(t_i-\hat{\tau})} + \frac{[\sum_i y_i \sin\omega(t_i-\hat{\tau})]^2}{\sum_i \sin^2\omega(t_i-\hat{\tau})}\right\} \tag{2.2}$$

where the hats are used in this paper to symbolise the classical expressions. The parameter $\hat{\tau}$ is calculated via

$$\tan 2\omega\hat{\tau} = \frac{\sum_i \sin 2\omega t_i}{\sum_i \cos 2\omega t_i}. \tag{2.3}$$

However, there are two shortcomings. First, the Lomb-Scargle periodogram does not take the measurement errors into account. This was solved by introducing weighted sums by Gilliland & Baliunas (1987) and Irwin et al. (1989) (equivalent to the generalisation to a χ^2 fit). Second, for the analysis the mean of the data was subtracted, which assumes that the mean of the data and the mean of the fitted sine function are the same. One can overcome this assumption with the introduction of an offset c, resulting in a further generalisation of this periodogram to the equivalent of weighted full sine wave fitting; i.e., $y = a\cos\omega t + b\sin\omega t + c$. Cumming et al. (1999), who called this generalisation "floating-mean periodogram", argue that this approach is superior: *"... the Lomb-Scargle periodogram fails to account for statistical fluctuations in the mean of a sampled sinusoid, making it non-robust when the number of observations is small, the sampling is uneven, or for periods comparable to or greater than the duration of the observations."* These authors provided a formal definition and also a sophisticated statistical treatment, but do not use an analytical solution for the computation of this periodogram.

Basically, analytical formulae for a full sine, least-squares spectrum have already been given by Ferraz-Mello (1981), calling this date-compensated discrete Fourier transform (DCDFT). We prefer to adopt a notation closely related to the Lomb-Scargle periodogram calling it the generalised Lomb-Scargle periodogram (GLS). Shrager (2001) tries for such an approach but did not generalise the parameter $\hat{\tau}$ in Eq. (2.3). Moreover, our generalised equations, which are derived in the following (Sect. 2.2), have a comparable symmetry to the classical ones and also allow us to point out equivalences to the "spectral significance" estimator used in the SigSpec program by Reegen (2007) (Sect. 2.4).

2.2 The generalised Lomb-Scargle periodogram (GLS)

The analytic solution for the generalised Lomb-Scargle periodogram can be obtained in a straightforward manner in the same way as outlined in Lomb (1976). Let y_i be the N measurements of a time series at time t_i and with errors σ_i. Fitting a full sine function (i.e. including an offset c):

$$y(t) = a\cos\omega t + b\sin\omega t + c$$

at given frequency ω (or period $P = \frac{2\pi}{\omega}$) means to minimise the squared difference between the data y_i and the model function $y(t)$:

$$\chi^2 = \sum_{i=1}^{N} \frac{[y_i - y(t_i)]^2}{\sigma_i^2} = W \sum w_i [y_i - y(t_i)]^2$$

where

$$w_i = \frac{1}{W}\frac{1}{\sigma_i^2} \qquad \left(W = \sum \frac{1}{\sigma_i^2} \qquad \sum w_i = 1\right)$$

are the normalised weights[1]. Minimisation leads to a system of (three) linear equations whose solution is derived in detail in Sect. 2.7.1. Furthermore, it is shown in Sect. 2.7.1 that the relative χ^2-reduction $p(\omega)$ as a function of frequency ω and normalised to unity by χ_0^2 (the χ^2 for the weighted mean) can be written as:

$$p(\omega) = \frac{\chi_0^2 - \chi^2(\omega)}{\chi_0^2} \tag{2.4}$$

$$p(\omega) = \frac{1}{YY \cdot D}\left[SS \cdot YC^2 + CC \cdot YS^2 - 2CS \cdot YC \cdot YS\right] \tag{2.5}$$

[1] For clarity the bounds of the summation are suppressed in the following notation. They are always the same ($i = 1, 2, ..., N$).

with:

$$D(\omega) = CC \cdot SS - CS^2 \tag{2.6}$$

and the following abbreviations for the sums:

$$Y = \sum w_i y_i \tag{2.7}$$
$$C = \sum w_i \cos \omega t_i \tag{2.8}$$
$$S = \sum w_i \sin \omega t_i \tag{2.9}$$

$$YY = \hat{YY} - Y \cdot Y \qquad \hat{YY} = \sum w_i y_i^2 \tag{2.10}$$
$$YC(\omega) = \hat{YC} - Y \cdot C \qquad \hat{YC} = \sum w_i y_i \cos \omega t_i \tag{2.11}$$
$$YS(\omega) = \hat{YS} - Y \cdot S \qquad \hat{YS} = \sum w_i y_i \sin \omega t_i \tag{2.12}$$
$$CC(\omega) = \hat{CC} - C \cdot C \qquad \hat{CC} = \sum w_i \cos^2 \omega t_i \tag{2.13}$$
$$SS(\omega) = \hat{SS} - S \cdot S \qquad \hat{SS} = \sum w_i \sin^2 \omega t_i \tag{2.14}$$
$$CS(\omega) = \hat{CS} - C \cdot S \qquad \hat{CS} = \sum w_i \cos \omega t_i \sin \omega t_i \tag{2.15}$$

Note that sums with hats correspond to the classical sums. $W \cdot YY \equiv \chi_0^2$ is simply the weighted sum of squared deviations from the weighted mean. The mixed sums can also be written as a weighted covariance $Cov_{x,y} = \sum w_i x_i y_i - X \cdot Y/W = E(x \cdot y) - WE(x)E(y)$ where E is the expectation value, e.g. $YS = Cov_{y,\sin \omega t}$.

With the weighted mean given by $\bar{y} = \sum w_i y_i = Y$ Eqs. (2.10)-(2.12) can also be written as:

$$YY = \sum w_i (y_i - \bar{y})^2 \tag{2.16}$$
$$YC(\omega) = \sum w_i (y_i - \bar{y}) \cos \omega t_i \tag{2.17}$$
$$YS(\omega) = \sum w_i (y_i - \bar{y}) \sin \omega t_i. \tag{2.18}$$

So the sums YC and YS use the weighted mean subtracted data and are calculated in the same way as for the Lomb-Scargle periodogram (but with weights).

The generalised Lomb-Scargle periodogram $p(\omega)$ in Eq. (2.4) is normalised to unity and therefore in the range of $0 \leq p \leq 1$, with $p = 0$ indicating no improvement of the fit and $p = 1$ a "perfect" fit (100% reduction of χ^2 or $\chi^2 = 0$).

As the full sine fit is time-translation invariant, there is also the possibility to introduce an arbitrary time reference point τ ($t_i \rightarrow t_i - \tau$; now, e.g. $CC = \sum w_i \cos^2 \omega(t_i - \tau) - (\sum w_i \cos \omega(t_i - \tau))^2$), which will not affect the χ^2 of the fit. If this parameter τ is chosen as

$$\begin{aligned} \tan 2\omega\tau &= \frac{2CS}{CC - SS} \\ &= \frac{\sum w_i \sin 2\omega t_i - 2 \sum w_i \cos \omega t_i \sum w_i \sin \omega t_i}{\sum w_i \cos 2\omega t_i - \left[\left(\sum w_i \cos \omega t_i \right)^2 - \left(\sum w_i \sin \omega t_i \right)^2 \right]} \end{aligned} \tag{2.19}$$

the interaction term in Eq. (2.5) disappears,

$$CS_\tau = \sum w_i \cos \omega(t_i - \tau) \sin \omega(t_i - \tau) - \sum w_i \cos \omega(t_i - \tau) \sum w_i \sin \omega(t_i - \tau) = 0$$

(proof in Appendix 2.7.2) and in this case we append the index τ to the time dependent sums. The parameter $\tau(\omega)$ is determined by the times t_i and the measurement errors σ_i for each frequency ω. So when using τ as defined in Eq. (2.19) the periodogram in Eq. (2.5) becomes

$$p(\omega) = \frac{1}{YY} \left[\frac{YC_\tau^2}{CC_\tau} + \frac{YS_\tau^2}{SS_\tau} \right]. \tag{2.20}$$

Note that Eq. (2.20) has the same form as the Lomb-Scargle periodogram in Eq. (2.1) with the difference that the errors can be weighted (weights w_i in all sums) and that there is an additional second term in CC_τ, SS_τ, CS_τ and $\tan 2\omega\tau$ (Eqs. (2.13)–(2.15) and Eq. (2.19), respectively) which accounts for the floating mean.

The computational effort is similar as for the Lomb-Scargle periodogram. The incorporation of the offset c requires only two additional sums for each frequency ω (namely $S = \sum w_i \sin \omega t_i$ and $C = \sum w_i \cos \omega t_i$ or S_τ and C_τ, respectively). The effort is even weaker when using Eq. (2.5) with keeping CS instead of using Eq. (2.20) with the parameter τ introduced via Eq. (2.19) which needs an extra preceding loop in the algorithm. If the errors are taken into account as weights, also the multiplication with w_i must be done.

For fast computation of the trigonometric sums the algorithm of Press & Rybicki (1989) can be applied, which has advantages in the case of large data sets and/or many frequency steps. Another possibility are trigonometric recurrences[2] as described in Press et al. (1992). Note also that the first sum in SS can be expressed by $\hat{SS} = 1 - \hat{CC}$.

2.3 Normalisation and False-Alarm probability (FAP)

There were several discussions in the literature on how to normalise the periodogram. For the detailed discussion we refer to the key papers by Scargle (1982), Horne & Baliunas (1986), Koen (1990) and Cumming et al. (1999). The normalisation becomes important for estimations of the false-alarm probability of a signal by means of an analytic expression. Lomb (1976) showed that if data are Gaussian noise, the terms $\hat{YC}^2/\hat{CC}$ and $\hat{YS}^2/\hat{SS}$ in Eq. (2.1) are χ^2-distributed and therefore the sum of both (which is $\propto p$) is χ^2-distributed with two degrees of freedom. This holds for the generalisation in Eq. (2.20) and also becomes clear from the definition of the periodogram in Eq. (2.4) $p(\omega) = \frac{\chi_0^2 - \chi^2(\omega)}{\chi_0^2}$ where for Gaussian noise the difference in the numerator $\chi_0^2 - \chi^2(\omega)$ is χ^2-distributed with $\nu = (N-1) - (N-3) = 2$ degrees of freedom.

The $p(\omega)$ can be compared with a known noise level p_n (expected from the *a priori* known noise variance or population variance) and the normalisation of $p(\omega)$ to p_n

$$P_n = \frac{p(\omega)}{p_n} \tag{2.21}$$

can be considered as a signal to noise ratio (Scargle, 1982). However, this noise level is often not known.

Alternatively, the noise level may be estimated for Gaussian noise from Eq. (2.4) to be $p_n = \frac{2}{N-1}$ which leads to:

$$P = \frac{N-1}{2} p(\omega) \tag{2.22}$$

and is the analogon to the normalisation in Horne & Baliunas (1986)[3]. So if the data are noise, $P = 1$ is the expected value. If the data contains a signal, $P \gg 1$ is expected at the signal frequency. However, this power is restricted to $0 \leq P \leq \frac{N-1}{2}$.

But if the data contains a signal or if errors are under- or overestimated or if intrinsic variability is present, then $p_n = \frac{2}{N-1}$ may not be a good uncorrelated estimator for the noise level. Cumming et al. (1999) suggested to estimate the noise level *a posteriori* with the residuals of the best fit and normalised the periodogram as

$$z(\omega) = \frac{N-3}{2} \frac{\chi_0^2 - \chi^2(\omega)}{\chi^2_{\rm best}} = \frac{N-3}{2} \frac{p(\omega)}{1 - p_{\rm best}} \tag{2.23}$$

[2] E.g. $\cos \omega_{k+1} t = \cos(\omega_k + \Delta\omega)t = \cos \omega_k t \cos \Delta\omega_k t - \sin \omega_k t \sin \Delta\omega t$ where $\Delta\omega$ is the frequency step.

[3] These authors called it the normalization with the sample variance σ_0^2. Note that $p(\omega)$ is already normalized with χ_0^2. For the unweighted case ($w_i = \frac{1}{N}$, $\sigma_0^2 = \frac{N}{N-1} YY$) one can write Eq. (2.22) with Eq. (2.20) as $P(\omega) = \frac{1}{2} \frac{N}{\sigma_0^2} \left[\frac{YC^2}{CC} + \frac{YS^2}{SS} \right]$.

Table 2.1: Probabilities that a periodogram power (P_n, p, P or z) can exceed a given value ($P_{n,0}$, p_0, P_0 or z_0) for different normalizations (from Cumming et al. 1999).

Reference level	Range	Probability
population variance	$P_n \in [0,\infty)$	$\mathrm{Prob}(P_n > P_{n,0}) = \exp(-P_{n,0})$
sample variance	$p \in [0,1]$	$\mathrm{Prob}(p > p_0) = (1-p_0)^{\frac{N-3}{2}}$
– " –	$P \in [0, \frac{N-1}{2}]$	$\mathrm{Prob}(P > P_0) = \left(1-\frac{2P}{N-1}\right)^{\frac{N-3}{2}}$
residual variance	$z \in [0,\infty)$	$\mathrm{Prob}(z > z_0) = \left(1+\frac{2z_0}{N-3}\right)^{-\frac{N-3}{2}}$

where the index "best" denotes the corresponding values of the best fit ($p_{\mathrm{best}} = p(\omega_{\mathrm{best}})$).

Statistical fluctuations or a present signal may lead to a larger periodogram power. To test for the significance of such a peak in the periodogram, the probability is assessed that this power can arise purely from noise. Cumming et al. (1999) clarified that the different normalisations result in different probability functions which are summarised in Table 2.1. Note that the last two probability values are the same for the best fit ($z_0 = z_{\mathrm{best}}$):

$$\begin{aligned}\mathrm{Prob}(z > z_{\mathrm{best}}) &= \left(1+\frac{2z_{\mathrm{best}}}{N-3}\right)^{-(N-3)/2} = \left(1+\frac{p_{\mathrm{best}}}{1-p_{\mathrm{best}}}\right)^{-(N-3)/2} \\ &= \left(\frac{1}{1-p_{\mathrm{best}}}\right)^{-(N-3)/2} = (1-p_{\mathrm{best}})^{(N-3)/2} \\ &= \mathrm{Prob}(p > p_{\mathrm{best}}) = \mathrm{Prob}(P > P_{\mathrm{best}}).\end{aligned}$$

Furthermore Baluev (2008) pointed out that the power definition

$$Z(\omega) = \frac{N-3}{2} \ln \frac{\chi_0^2}{\chi^2(\omega)}$$

as a nonlinear (logarithmic) scale for χ^2 has an exponential distribution (similiar to P_n)

$$\mathrm{Prob}(Z > Z_{\mathrm{best}}) = e^{-Z} = \left(\frac{\chi^2(\omega)}{\chi_0^2}\right)^{(N-3)/2} = \mathrm{Prob}(p > p_{\mathrm{best}}).$$

Since in period search with the periodogram we study a range of frequencies, we are also interested in the significance of one peak compared to the peaks at other frequencies rather than the significance of a single frequency. The false alarm probability (FAP) for the period search in a frequency range is given by

$$\mathrm{FAP} = 1 - [1 - \mathrm{Prob}(z > z_0)]^M \tag{2.24}$$

where M is the number of independent frequencies and may be estimated as the number of peaks in the periodogram. The width of one peak is $\delta f \approx \frac{1}{T}$ (≈frequency resolution). So in the frequency range $\Delta f = f_2 - f_1$ there are approximately $M = \frac{\Delta f}{\delta f}$ peaks and in the case $f_1 \ll f_2$ one can write $M \approx T f_2$ (Cumming, 2004). Finally, for low FAP values the following handy approximation for Eq. (2.24) is valid:

$$\mathrm{FAP} \approx M \cdot \mathrm{Prob}(z > z_0) \quad \text{for} \quad \mathrm{FAP} \ll 1. \tag{2.25}$$

Another possibility to access M and the FAP are Monte Carlo or bootstrap simulations in order to determine how often a certain power level (z_0) is exceeded just by chance. Such numerical calculation of the FAP are much more time-consuming than the actual computation of the GLS.

2.4 Equivalences between the GLS and SigSpec (Reegen, 2007)

Reegen (2007) developed a method, called SigSpec, to determine the significance of a peak at a given frequency (spectral significance) in a discrete Fourier transformation (DFT) which includes a zero mean correction. We will recapitulate some points from his paper in an adapted and shortened way in order to show several equivalences and to disentangle different notations used by us and used by Reegen (2007). For a detailed description we refer to the original paper. Briefly, approaching from Fourier theory Reegen (2007) defined the zero mean corrected Fourier coefficients[4]

$$a_{\mathrm{ZM}}(\omega) = \frac{1}{N}\sum y_i \cos\omega t_i - \frac{1}{N^2}\sum y_i \cdot \sum \cos\omega t_i$$
$$b_{\mathrm{ZM}}(\omega) = \frac{1}{N}\sum y_i \sin\omega t_i - \frac{1}{N^2}\sum y_i \cdot \sum \sin\omega t_i$$

which obviously correspond to YC and YS in Eqs. (2.11) and (2.12). Their variances are given by

$$\left\langle a_{\mathrm{ZM}}^2 \right\rangle = \frac{\left\langle y^2 \right\rangle}{N^2}\left[\sum \cos^2\omega t_i - \frac{1}{N}\left(\sum \cos\omega t_i\right)^2\right]$$

$$\left\langle b_{\mathrm{ZM}}^2 \right\rangle = \frac{\left\langle y^2 \right\rangle}{N^2}\left[\sum \sin^2\omega t_i - \frac{1}{N}\left(\sum \sin\omega t_i\right)^2\right]$$

The precise value of these variances depends on the temporal sampling. These variances can be expressed as $\left\langle a_{\mathrm{ZM}}^2 \right\rangle = \frac{\left\langle y^2 \right\rangle}{N} CC$ and $\left\langle b_{\mathrm{ZM}}^2 \right\rangle = \frac{\left\langle y^2 \right\rangle}{N} SS$.

Consider now two independent Gaussian variables whose cumulative distribution function (CDF) is given by:

$$\Phi(\alpha,\beta|\omega) = e^{-\frac{1}{2}\left(\frac{\alpha^2}{\langle\alpha^2\rangle}+\frac{\beta^2}{\langle\beta^2\rangle}\right)}.$$

A Gaussian distribution of the physical variable y_i in the time domain will lead to Gaussian variables a_{ZM} and b_{ZM} which in general are correlated. A rotation of Fourier Space by phase θ_0

$$\tan 2\theta_0 = \frac{N\sum \sin 2\omega t_i - 2\sum \cos\omega t_i \sum \sin\omega t_i}{N\sum \cos 2\omega t_i - (\sum \cos\omega t_i)^2 + (\sum \sin\omega t_i)^2}$$

transforms a_{ZM} and b_{ZM} into uncorrelated coefficients α and β with vanishing covariance. Indeed, $\omega\tau$ from Eq. (2.19) and θ_0 have the same value, but τ is applied in the time domain, while θ_0 is applied to the phase θ in the Fourier domain. It is only mentioned here that the resulting coefficients 2α and 2β correspond to YC_τ and YS_τ.

Finally, Reegen (2007) defines as the spectral significance $\mathrm{sig}(\alpha,\beta|\omega) := -\log\Phi(\alpha,\beta|\omega)$ and writes:

$$\mathrm{sig}(a_{\mathrm{ZM}}, b_{\mathrm{ZM}}|\omega) = \frac{N\log e}{\langle y^2\rangle}\left[\left(\frac{a_{\mathrm{ZM}}\cos\theta_0 + b_{\mathrm{ZM}}\sin\theta_0}{\alpha_0}\right)^2 + \left(\frac{a_{\mathrm{ZM}}\cos\theta_0 - b_{\mathrm{ZM}}\sin\theta_0}{\beta_0}\right)^2\right] \tag{2.26}$$

where

$$\alpha_0 := \sqrt{2N\frac{\langle\alpha^2\rangle}{\langle y^2\rangle}}$$
$$= \sqrt{\frac{2}{N^2}\left\{N\sum\cos^2(\omega t_i-\theta_0) - \left[\sum\cos(\omega t_i-\theta_0)\right]^2\right\}}$$

[4]Here only the unweighted case is discussed ($w_i = \frac{1}{N}$). Reegen (2007) also gives a generalization to weighting.

$$\beta_0 := \sqrt{2N\frac{\langle\beta^2\rangle}{\langle y^2\rangle}}$$
$$= \sqrt{\frac{2}{N^2}\left\{N\sum\sin^2(\omega t_i-\theta_0)-\left[\sum\sin(\omega t_i-\theta_0)\right]^2\right\}}$$

are called normalised semi-major and semi-minor axes. Note that $\alpha_0^2 \sim 2CC_\tau$ and $\beta_0^2 \sim 2SS_\tau$.

Reegen (2007) states that this gives as accurate frequencies as do least squares. However, from this derivation it is not clear that this is equivalent. But when comparing Eq. (2.26) to Eq. (2.20) with using $YC_\tau = YC\cos\omega\tau + YS\sin\omega\tau$ and $YS_\tau = YS\cos\omega\tau - YC\sin\omega\tau$:

$$p(\omega) = \frac{1}{YY}\left[\frac{(YC\cos\omega\tau+YS\sin\omega\tau)^2}{CC_\tau} + \frac{(YS\cos\omega\tau-YC\sin\omega\tau)^2}{SS_\tau}\right]$$

the equivalence of the GLS and the spectral significance estimator in SigSpec (and with it to least squares) is evident:

$$\mathrm{sig}(a_{\mathrm{ZM}}, b_{\mathrm{ZM}}|\omega) = \frac{YY\cdot N\log e}{2\langle y^2\rangle}\cdot p(\omega). \tag{2.27}$$

The two indicators differ only in a normalisation factor, which becomes $\frac{N-1}{2}\log e$, when $\langle y^2\rangle$ is estimated with the sample variance $\langle y_i^2\rangle = \frac{N}{N-1}YY$. Therefore, SigSpec gives accurate frequencies just like least squares. But note that the Fourier amplitude is given by the sum of the squared Fourier coefficient $A^2 = a_{ZM}^2 + b_{ZM}^2 = 4\alpha^2 + 4\beta^2 \sim YC^2 + YS^2 = YC_\tau^2 + YS_\tau^2$ while the least-squares fitting amplitude is $A^2 = a^2 + b^2 = \frac{YC_\tau^2}{CC_\tau^2} + \frac{YS_\tau^2}{SS_\tau^2}$ (see Sect. 2.7.1).

The comparison with SigSpec offers another point of view. It shows how the GLS is associated to Fourier theory and how it can be derived from the DFT (discrete Fourier transform) when demanding certain statistical properties such as simple statistical behaviour, time-translation invariance (Scargle, 1982) and varying zero mean. The shown equivalences allow *vice versa* to apply several of Reegen's (2007) conclusions to the GLS, e.g. that it is less susceptible to aliasing or that the time domain sampling is taken into account in the probability distribution.

2.5 Application of the GLS to the Keplerian periodogram (Keplerian fits to radial velocity data)

The search for the best-fitting sine function is a multidimensional χ^2-minimisation problem with four parameters: period P, amplitude A, phase φ, and offset c (or frequency $\omega = 2\pi/P$, a, b and c). At a given frequency ω the best-fitting parameters A, φ, and c can be computed immediately by an analytic solution revealing the global optimum for this three dimensional parameter subspace. But involving the frequency leads to a lot of local optima (minima in χ^2) as visualised by the numbers of maxima in the generalised Lomb-Scargle periodogram. With stepping through frequency ω one can pick up the global optimum in the four dimensional parameter space. That is how period search with the periodogram works. Because an analytic solution (implemented in the GLS) can be employed partially, there is no need for stepping through all parameters to explore the whole parameter space for the global optimum.

This concept can be transferred to the Keplerian periodogram which can be applied to search stellar radial velocity data for periodic signals caused by orbiting companions and measured from spectroscopic Doppler shifts. The radial velocity curve becomes more non-sinusoidal for a more eccentric orbit and its

shape depends on six orbital elements[5]:

γ	constant system radial velocity
K	radial velocity amplitude
ϖ	longitude of periastron
e	eccentricity
T_0	periastron passage
P	period.

In comparison to the full sine fit there are two more parameters to deal with which complicates the period search. An approach to simplify the Keplerian orbit search is to use the GLS to look for a periodic signal and use it for an initial guess. But choosing the best-fitting sine period does not necessarily lead to the best-fitting Keplerian orbit. So for finding the global optimum the whole parameter space must be explored.

The Keplerian periodogram (Cumming, 2004), just like the GLS, shows how good a trial period (frequency ω) can model the observed radial velocity data and can be defined as (χ^2-reduction):

$$p_{\mathrm{Kep}}(\omega) = \frac{\chi_0^2 - \chi_{\mathrm{Kep}}^2(\omega)}{\chi_0^2}.$$

Instead of the sine function, the function

$$RV(t) = \gamma + K[e\cos\varpi + \cos(\nu(t) + \varpi)] \tag{2.28}$$

which describes the radial reflex motion of a star due to the gravitational pull of a planet, serves as the model for the radial velocity curve. The time dependence is given by the true anomaly ν which furthermore depends on three orbital parameters ($\nu(t, P, e, T_0)$). The relation between ν and time t is:

$$\tan\frac{\nu}{2} = \sqrt{\frac{1+e}{1-e}}\tan\frac{E}{2}$$

$$E - e\sin E = M = 2\pi\frac{t - T_0}{P} \tag{2.29}$$

where E and M are called eccentric anomaly and mean anomaly, respectively[6]. Eq. (2.29), called Kepler's equation, is transcendent meaning that for a given time t the eccentric anomaly E cannot be calculated explicitly.

For the computation of a Keplerian periodogram χ^2 is to be minimised with respect to five parameters at a fixed trial frequency ω. Similar to the GLS there is no need for stepping through all parameters. With the substitutions $c = \gamma + Ke\cos\varpi$, $a = K\cos\varpi$ and $b = -K\sin\varpi$ Eq. (2.28) can be written as:

$$RV(t) = c + a\cos\nu(t) + b\sin\nu(t)$$

and with respect to the parameters a, b and c the analytic solution can be employed as described in Sect. 2.2 for known ν (instead of ωt) . So for fixed P, e and T_0 the true anomalies ν_i can be calculated and the GLS from Eq. (2.5) (now using ν_i instead of ωt_i) can be applied to compute the maximum χ^2-reduction ($p(\omega)$), here called $p_{e,T_0}(\omega)$. Stepping through e and T_0 yields the best Keplerian fit at frequency ω:

$$p_{\mathrm{Kep}}(\omega) = \max_{e,T_0} p_{e,T_0}(\omega)$$

[5] $K = \frac{2\pi}{P}\frac{a\sin i}{\sqrt{1-e^2}}$ with a the semi-major axis of the stellar orbit and i the inclination.

[6] The following expressions are also used frequently: $\sin\nu = \frac{\sqrt{1-e^2}\sin E}{1-e\cos E}$ and $\cos\nu = \frac{\cos E - e}{1-e\cos E}$.

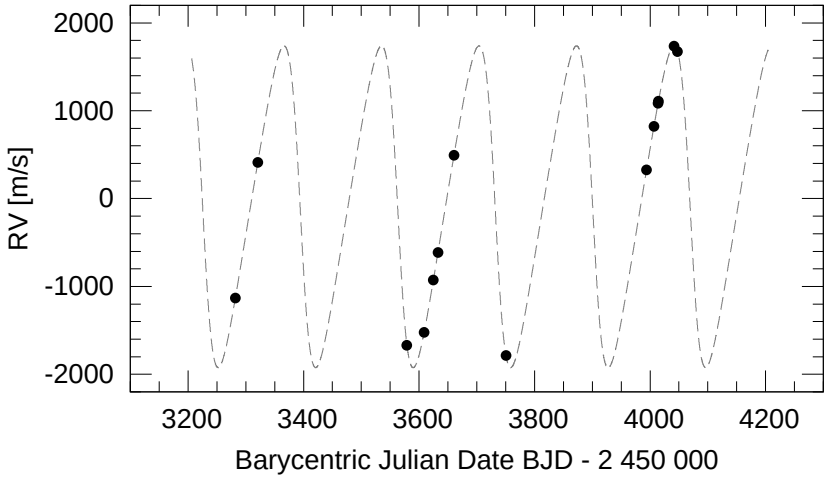

Figure 2.1: The radial velocity (RV) time series of the M dwarf GJ 1046. The dashed line is the best Keplerian orbit fit ($P = 168.8\,\mathrm{d}$, $e = 0.28$).

as visualised in the Keplerian periodogram. Finally, with stepping through the frequency, like for the GLS, one will find the best-fitting Keplerian orbit having the overall maximum power:

$$p_{\mathrm{Kep}}(\omega_{\mathrm{best}}) = \max_{\omega} p_{\mathrm{Kep}}(\omega).$$

There exist a series of tools (or are under development) using genetic algorithms or Bayesian techniques for fast searches for the best Keplerian fit (Ford & Gregory, 2007; Balan & Lahav, 2009). The algorithm, presented in this section, is not further optimised for speed. But it works well, is easy to implement and is robust since in principle it cannot miss a peak if the 3 dimensional grid for e, T_0 and ω is sufficiently dense. A reliable algorithm is needed for the computation of the Keplerian periodogram which by definition yields the best fit at fixed frequency and no local χ^2-minima. O'Toole et al. (2007, 2009b) developed an algorithm called 2DKLS (two dimensional Kepler Lomb-Scargle) that works on grid of period and eccentricity and seems to be similar to ours. But the possibility to use partly an analytic solution or the need for stepping T_0 is not mentioned by these authors.

The effort to compute the Keplerian periodogram with the described algorithm is much stronger in comparison to the GLS. There are three additional loops: two loops for stepping through e and T_0 and one for the iteration to solve Kepler's equation. Contrary to the GLS it is not possible to use recurrences or the fast computation of the trigonometric sums mentioned in Sect. 2.2.

However we would like to outline some possibilities for technical improvements for a faster search. The first concerns the grid size. We choose a regular grid for e, T_0 and ω. While this is adequate for the frequency ω, as we discuss later in this section, there might be a more appropriate e-T_0 grid, e.g. a less dense grid size for T_0 at lower eccentricities. A second possibility is to reduce the iterations for solving Kepler's equation by using the eccentric anomalies (or differentially corrected ones) as initial values for the next slightly different grid point. This can save several ten percent of computation time, in particular in dense grids and at high eccentricities. A third idea which might have a high potential for speed up is to combine our algorithm with other optimisation techniques (e.g. Levenberg-Marquardt instead of pure stepping) to optimise the remaining parameters in the function $p_{e,T_0}(\omega)$. A raw grid would provide the initial values and the optimisation technique would do the fine adjustment.

To give an example Fig. 2.1 shows RV data for the M dwarf GJ 1046 (Kürster et al., 2008) along with the best-fitting Keplerian orbit ($P = 168.8\,\mathrm{d}$, $e = 0.28$). Figure 2.2 shows the Lomb-Scargle, GLS, and Keplerian periodograms. Because a Keplerian orbit has more degrees of freedom it always has the highest χ^2 reduction ($0 \leq p_{\mathrm{LS}} \leq p_{\mathrm{GLS}} \leq p_{\mathrm{Kep},e<0.6} \leq p_{\mathrm{Kep}} \leq 1$).

As a comparison the Keplerian periodogram restricted to $e < 0.6$ is also shown in Fig. 2.2. At intervals where p_{Kep} exceeds $p_{e<0.6}$ the contribution is due to very eccentric orbits. Note that the Keplerian

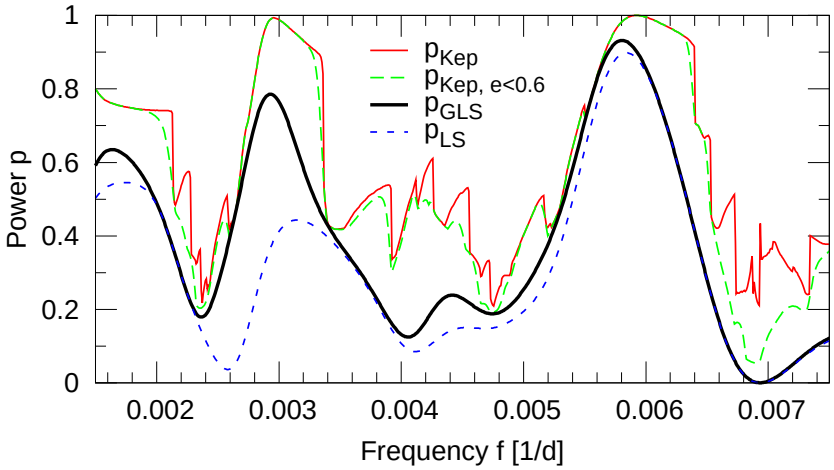

Figure 2.2: Comparison of the normalized Lomb-Scargle (LS), GLS and Keplerian periodograms for GJ 1046 ($f = \frac{1}{P} = \frac{\omega}{2\pi}$).

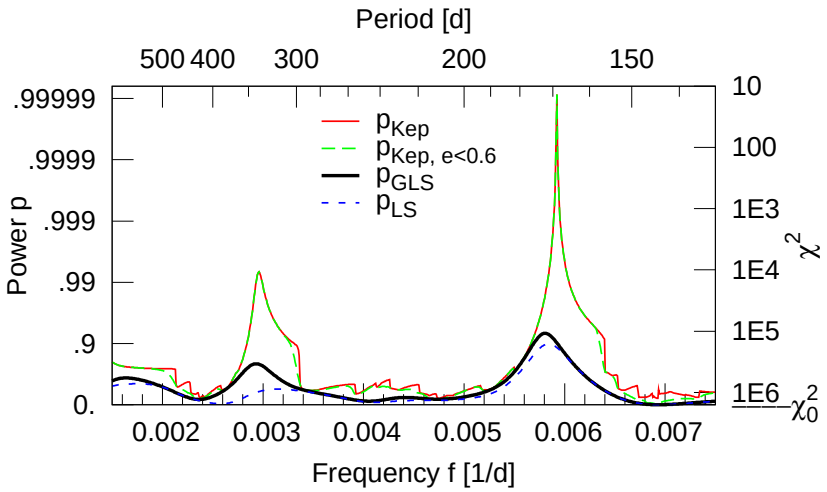

Figure 2.3: The same periodograms as in Fig. 2.2 with a quasi-logarithmic scale for p and a logarithmic scale for χ^2 (axis to the right).

periodogram obtains more structure when the search is extended to more eccentric orbits. Therefore the evaluation of the Keplerian periodogram needs a higher frequency resolution (this effect can also be observed in O'Toole et al. 2009b). This is a consequence of the fact that more eccentric orbits are spikier and thus more sensitive to phase and frequency.

Other than O'Toole et al. (2009b) we plot the periodograms against frequency[7] to illustrate that the typical peak width δf is frequency independent. Thus equidistant frequency steps ($\mathrm{d}f < \delta f$) yield a uniform sampling of each peak and are the most economic way to compute the periodogram rather than e.g. logarithmic period steps (leading to oversampling at long periods: $\mathrm{d}f = \mathrm{d}\frac{1}{P} = -\frac{1}{P^2}\mathrm{d}P = -\frac{1}{P}\mathrm{d}\ln P$) as used by O'Toole et al. (2009b). Still the periodograms can be plotted against a logarithmic period scale as e.g. sometimes preferred to present a period search for exoplanets.

Figure 2.4 visualises local optima in the p_{e,T_0} map at an arbitrary fixed frequency. There are two obvious local optima which means that searching from only one initial value for T_0 may be not sufficient as one could fail to lead the best local optimum in the e-T_0 plane. This justifies a stepping through e and T_0. The complexity in the e-T_0 plane, in particular at high eccentricities, finally translates into the

[7] for Fourier transforms this is common

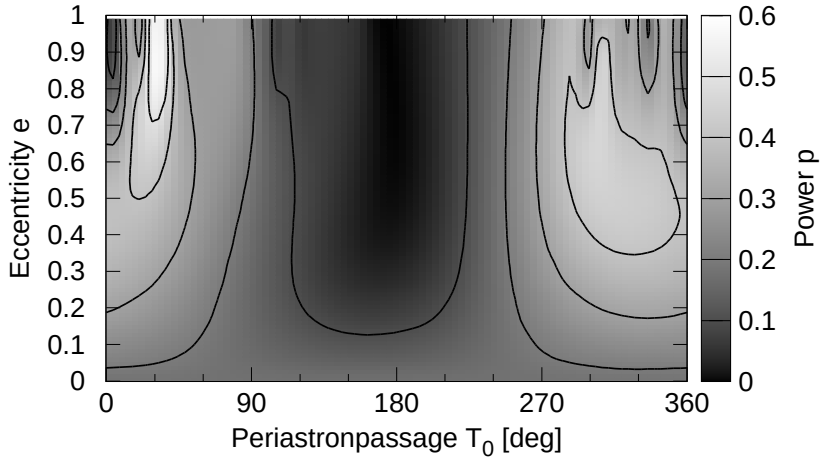

Figure 2.4: Power map (p_{e,T_0}) for e and T_0 at the arbitrary fixed frequency $f = 0.00422\,\mathrm{d}^{-1}$. The maximum value $p = 0.592$ is deposited in the Keplerian periodogram. Note that there are the two local optima.

Keplerian periodogram. When varying the frequency the landscape and maxima will evolve and the maxima can also switch.

In the given example LS and GLS would give a good initial guess for the best Keplerian period with only a slight frequency shift. But this is not always the case.

One may argue, that the second peak has an equal height suggesting the same significance. On a linear scale it seems so. But the significance is not a linear function of the power. Cumming et al. (2008) normalised the Keplerian periodogram as

$$z_{\mathrm{Kep}}(\omega) = \frac{N-5}{4}\frac{\chi_0^2 - \chi^2(\omega)}{\chi^2_{\mathrm{best}}} = \frac{N-5}{4}\frac{p_{\mathrm{Kep}}(\omega)}{1-p_{\mathrm{Kep}}(\omega_{\mathrm{best}})} \tag{2.30}$$

analogous to Eq. (2.23) and derived the probability distribution

$$\mathrm{Prob}(z > z_0) = \left(1 + \frac{N-3}{2}\frac{4z_0}{N-5}\right)\left(1 + \frac{4z_0}{N-5}\right)^{-\frac{N-3}{2}}.$$

With this we can calculate that the higher peak which is much closer to 1 has a 10^{-14} times lower probability to be due to noise, i.e. it has a 10^{14} times higher significance. In Fig. 2.3 the periodogram power is plotted on a logarithmic scale for χ^2 on the right-hand side. The much lower χ^2 is another convincing argument for the much higher significance.

Cumming (2004) suggested to estimate the FAP for the period search analogous to Eq. (2.25) and the number of independent frequencies again as $M \approx T\Delta f$. This estimation does not take into account the higher variability in the Keplerian periodogram, which depends on the examined eccentricity range, and therefore this FAP is likely to be underestimated.

Another, more extreme example is the planet around HD 20782 discovered by Jones et al. (2006). Figure 2.5 shows the RV data for the star taken from O'Toole et al. (2009b). Due to the high eccentricity this is a case where LS and GLS fail to find the right period. However, our algorithm for the Keplerian periodogram find the same solution as the 2DKLS ($P = 591.9\,\mathrm{d}$, $e = 0.97$). The Keplerian periodogram in Fig. 2.6 indicates this period. This time it is normalised according to Eq. (2.30) and seems to suffer from an overall high noise level (caused by many other eccentric solutions that will fit the one 'outlier'). However, that the period is significant can again be shown just as in the previous example.

For comparison we also show the periodogram with the normalisation by the best fit *at each* fre-

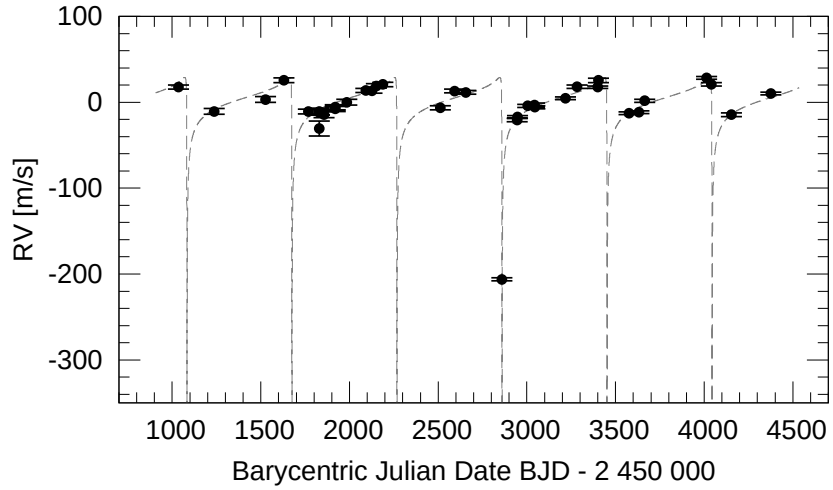

Figure 2.5: The radial velocity (RV) time series of HD 20782. The dashed line is the best Keplerian orbit fit.

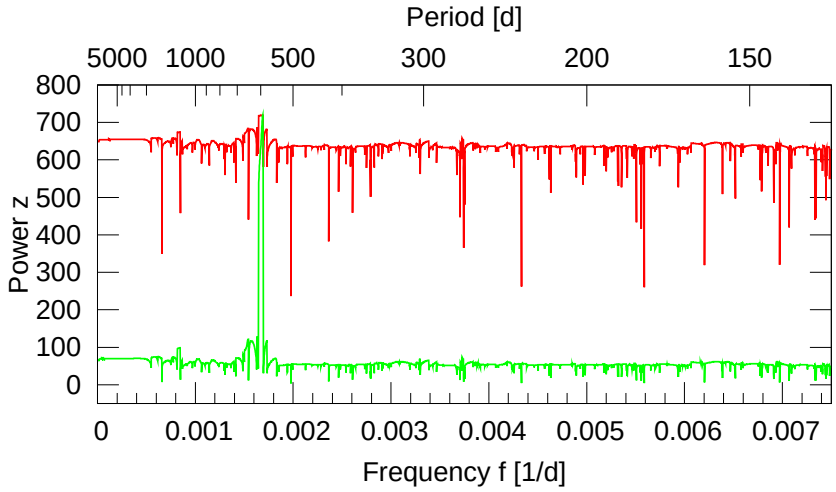

Figure 2.6: Keplerian periodogram for HD 20782. Both are the same Keplerian periodogram, but the upper one is normalized with the best fit (Eq. (2.30)) while the lower one is normalized with the best fit *at each* frequency (Eq. (2.31)). Both have by definition the same maximum value.

quency (Cumming, 2004)

$$z_{\mathrm{Kep}}(\omega) = \frac{N-5}{4}\frac{\chi_0^2 - \chi^2(\omega)}{\chi^2(\omega)} \tag{2.31}$$

which is used in the 2DKLS and reveals the power maximum as impressively as in O'Toole et al. (2009b, Fig. 1b). As Cumming et al. (1999) mentioned the choice of the normalisation is a matter of taste; the distribution of maximum power is the same. Finally, keep in mind when comparing Fig. 2.6 with the 2DKLS in O'Toole et al. (2009b, Fig. 1b) which shows a slice at $e = 0.97$, that the Keplerian periodogram in Fig. 2.6 includes all eccentricities ($0 \leq e \leq 0.99$). Also the algorithms are different because we also step for T_0 and simultaneously fit the longitude of periastron ϖ.

2.6 Conclusions

Generalised Lomb-Scargle periodogram (GLS), floating-mean periodogram (Cumming et al., 1999), date-compensated discrete Fourier transform (DCDFT, Ferraz-Mello 1981), and "spectral significance"

(SigSpec, Reegen 2007) at last all mean the same thing: least-squares spectrum for fitting a sinusoid plus a constant. Cumming et al. (1999) and Reegen (2007) have already shown the advantages of accounting for a varying zero point and therefore we recommend the usage of the generalised Lomb-Scargle periodogram (GLS) for the period analysis of time series. The implementation is easy as there are only a few modifications in the sums of the Lomb-Scargle periodogram.

The GLS can be calculated as conveniently as the Lomb-Scargle periodogram and in a straight forward manner with an analytical solution while programs applying standard routines for fitting sinusoids involve solving a set of linear equations by inverting a 3 x 3 matrix repeated at each frequency. The GLS can be tailored by concentrating the sums in one loop over the data. As already mentioned by Lomb (1976) Eq. (2.5) (including Eqs. (2.13)–(2.18)) should be applied for the numerical work. A fast calculation of the GLS is especially desirable for large samples, large data sets and/or many frequency steps. It also may be helpful to speed up prewhitening procedures (e.g. Reegen, 2007) in case of multifrequency analysis or numerical calculations of the significance of a signal with bootstrap methods or Monte Carlo simulations.

The term generalised Lomb-Scargle periodogram has already been used by Bretthorst (2001) for the generalisation to sinusoidal functions of the kind: $y(t) = aZ(t)\cos\omega t + bZ(t)\sin\omega t$ with an arbitrary amplitude modulation $Z(t)$ whose time dependence and all parameters are fully specified (e.g. $Z(t)$ can be an exponential decay). Without repeating the whole procedure given in Sect. 2.7.1, 2.7.2, and 2.2 it is just mentioned here that the generalisation to $y(t) = aZ(t)\cos\omega t + bZ(t)\sin\omega t + c$ will result in the same equations with the difference that $Z(t_i)$ has to be attached to each sine and cosine term in each sum (e.g. $\hat{CC} = \sum w_i Z(t_i)\cos\omega t_i \cdot Z(t_i)\cos\omega t_i$).

We presented an algorithm for the application of GLS to the Keplerian periodogram which is the least-squares spectrum for Keplerian orbits. It is an hybrid algorithm that partially applies an analytic solution for linearised parameters and partially steps through non-linear parameters. This has to be distinguished from methods that use the best sine fit as an initial guess. With two examples we have demonstrated that our algorithm for the computation of the Keplerian periodogram is capable to detect (very) eccentric planets in a systematic and nonrandom way.

Apart from this, the least-squares spectrum analysis (the idea goes back to Vaníček, 1971) with more complicated model functions than full sine functions is beyond the scope of this paper (e.g. including linear trends, Walker et al., 1995 or multiple sine functions). For the calculation of such periodograms the employment of the analytical solutions is not essential, but can be faster.

2.7 Accompanying auxiliary calculations

2.7.1 Derivation of the generalised Lomb-Scargle periodogram (GLS)

The derivation of the generalised Lomb-Scargle periodogram is briefly shown. With the sinusoid plus constant model

$$y(t) = a\cos\omega t + b\sin\omega t + c$$

the squared difference between the data y_i and the model function $y(t)$

$$\chi^2 = W\sum w_i[y_i - y(t_i)]^2$$

is to be minimised. For the minimum χ^2 the partial derivatives vanish and therefore:

$$0 = \partial_a\chi^2 = 2W\sum w_i[y_i - y(t_i)]\cos\omega t_i \tag{2.32}$$

$$0 = \partial_b\chi^2 = 2W\sum w_i[y_i - y(t_i)]\sin\omega t_i \tag{2.33}$$

$$0 = \partial_c\chi^2 = 2W\sum w_i[y_i - y(t_i)] \tag{2.34}$$

These conditions for the minimum give three linear equations:

$$\begin{bmatrix} \hat{YC} \\ \hat{YS} \\ Y \end{bmatrix} = \begin{bmatrix} \hat{CC} & \hat{CS} & C \\ \hat{CS} & \hat{SS} & S \\ C & S & 1 \end{bmatrix} \begin{bmatrix} a \\ b \\ c \end{bmatrix}$$

where the abbreviations in Eqs. (2.7)–(2.15) were applied. Eliminating c in the first two equations with the last equation ($c = Y - aC - bS$) yields:

$$\begin{bmatrix} \hat{YC} - Y \cdot C \\ \hat{YS} - Y \cdot S \end{bmatrix} = \begin{bmatrix} \hat{CC} - C \cdot C & \hat{CS} - C \cdot S \\ \hat{CS} - C \cdot S & \hat{SS} - S \cdot S \end{bmatrix} \begin{bmatrix} a \\ b \end{bmatrix}$$

Using again the notations of Eqs. (2.11)–(2.15) this can be written as:

$$\begin{bmatrix} YC \\ YS \end{bmatrix} = \begin{bmatrix} CC & CS \\ CS & SS \end{bmatrix} \begin{bmatrix} a \\ b \end{bmatrix}.$$

So the solution for the parameters a and b is

$$a = \frac{YC \cdot SS - YS \cdot CS}{D} \qquad \text{and} \qquad b = \frac{YS \cdot CC - YC \cdot CS}{D}. \tag{2.35}$$

The amplitude of the best-fitting sine function at frequency ω is given by $\sqrt{a^2 + b^2}$. With these solutions the minimum χ^2 can be written only in terms of the sums Eqs. (2.10)–(2.15) when eliminating the parameters a, b, and c as shown below. With the conditions for the minimum (Eqs. (2.32)–(2.34)) it can be seen that:

$$\begin{aligned} \sum w_i[y_i - y(t_i)]y(t_i) = \quad & a\sum w_i[y_i - y(t_i)]\cos\omega t_i \\ & + b\sum w_i[y_i - y(t_i)]\sin\omega t_i \\ & + c\sum w_i[y_i - y(t_i)] \\ & = 0. \end{aligned}$$

Therefore, the minimum χ^2 can be written as:

$$\begin{aligned} \chi^2(\omega)/W &= \sum w_i[y_i - y(t_i)]y_i - \underbrace{\sum w_i[y_i - y(t_i)]y(t_i)}_{=0} \\ &= \hat{YY} - a\hat{YC} - b\hat{YS} - cY \\ &= \hat{YY} - Y \cdot Y - a(\hat{YC} - Y \cdot C) - b(\hat{YS} - Y \cdot S) \\ &= YY - aYC - bYS \end{aligned}$$

where in the last step again the definitions of Eqs. (2.10)–(2.12) were applied. Finally a and b can be substituted by Eq. (2.35):

$$\chi^2(\omega)/W = YY - \frac{SS \cdot YC^2}{D} - \frac{CC \cdot YS^2}{D} + 2\frac{CS \cdot YC \cdot YS}{D}.$$

When now using the χ^2-reduction normalised to unity

$$p(\omega) = \frac{\chi_0^2 - \chi^2(\omega)}{\chi_0^2}$$

and the fact that $\chi_0^2 = W \cdot YY$, Eq. (2.5) will result.

2.7.2 Verification of Eq. (2.19)

Eq. (2.19) can be verified with the help of trigonometric addition theorems. For this purpose CS must be formulated. Furthermore, the index τ and the notation $\varphi = \omega\tau$ will be used:

$$\begin{aligned} 2CS_\tau = & \sum w_i \sin 2(\omega t_i - \varphi) \\ & - 2\sum w_i \cos(\omega t_i - \varphi)\sum w_i \sin(\omega t_i - \varphi) \\ = & \cos 2\varphi \sum w_i \sin 2\omega t_i - \sin 2\varphi \sum w_i \cos 2\omega t_i \\ & - 2(C\cos\varphi + S\sin\varphi)(S\cos\varphi - C\sin\varphi) \end{aligned}$$

Expanding the last term yields

$$\begin{aligned} 2CS_\tau =& 2\hat{CS}\cos 2\varphi - (\hat{CC} - \hat{SS})\sin 2\varphi \\ & - 2\left[C\cdot S(\cos^2\varphi - \sin^2\varphi) - (C^2 - S^2)\sin\varphi\cos\varphi\right] \end{aligned}$$

and after factoring $\cos 2\varphi$ and $\sin 2\varphi$:

$$\begin{aligned} 2CS_\tau =& 2(\hat{CS} - C\cdot S)\cos 2\varphi - \left(\hat{CC} - \hat{SS} - (C^2 - S^2)\right)\sin 2\varphi \\ =& 2CS\cos 2\varphi - (CC - SS)\sin 2\varphi. \end{aligned}$$

So for $CS_\tau = 0$, $\varphi = \omega\tau$ has to be chosen as:

$$\tan 2\omega\tau = \frac{2CS}{CC - SS}.$$

By the way, replacing the generalised sums CC, SS and CS by the classical ones leads to the original definition for $\hat{\tau}$ in Eq. (2.3):

$$\tan 2\omega\hat{\tau} = \frac{2\hat{CS}}{\hat{CC} - \hat{SS}} = \frac{\sum \sin 2\omega t_i}{\sum \cos 2\omega t_i}.$$

2.8 Comments on the GLS periodogram

2.8.1 Error estimation for the GLS parameters

The GLS periodogram is an algorithm to search for periods. However, it is also important to provide the uncertainties of the resulting parameters. There is a bunch of numerical methods, such as Bayesian or bootstrap methods, to derive parameter errors. However, they require extensive computation time and the development or implementation of special software. Hence, it is always desirable to have a simple analytical error estimation at hand. Montgomery & Odonoghue (1999) and Breger et al. (1999) outlined how this can be done analytically for a simple sine function assuming Gaussian noise. Their method is based on error propagation. Kallinger et al. (2008) obtained similar results with a heuristic error estimation for the SigSpec program (Sect. 2.4). Their relations give "upper error limits" (not 1σ errors) and are expressed in terms of power.

This section provides an error estimate for fitting a sine function including offset and weights. It can be done in a straightforward way using error propagation and the above notation for the GLS periodogram. The results can be expressed with the weighted rms and are hence a generalisation of the results by Montgomery & Odonoghue (1999) and Breger et al. (1999).

Errors in the coefficients a and b

The error for parameter a (the index τ is suppressed) for a given frequency ω can be estimated by simple error propagation

$$(\Delta a)^2 = \sum \left(\frac{\partial a}{\partial y_i} \right)^2 \sigma_i^2. \tag{2.36}$$

The gradient in brackets describes the response of parameter a when the data y_i changes. a is given by $a = \frac{YC}{CC}$ (again the index τ is suppressed). Hence, to derive $\partial_{y_i} a$, we need $\partial_{y_i} YC$

$$\begin{aligned} YC &= \hat{YC} - Y \cdot C = \sum w_i y_i \cos \omega t_i - \sum w_i y_i \cdot \sum w_i \cos \omega t_i \\ \partial_{y_i} YC &= w_i (\cos \omega t_i - C). \end{aligned}$$

The relation between the measurement errors σ_i and the normalised weights w_i is $w_i = \frac{1}{W} \frac{1}{\sigma_i^2}$ where $\sum w_i = 1$ and $W = \sum \frac{1}{\sigma_i^2} =: \frac{N}{\sigma^2}$. Substituting these expressions in Eq. (2.36) and simplifying gives

$$\begin{aligned} (\Delta a)^2 &= \frac{1}{CC^2 W} \sum \left(\frac{\partial YC}{\partial y_i} \right)^2 \frac{1}{w_i} = \frac{1}{CC^2 W} \sum w_i \left[\cos \omega t_i - C \right]^2 \\ &= \frac{1}{CC^2 W} \left[\hat{CC} - 2C \cdot C + C^2 \right] = \frac{\sigma^2}{CC^2 N} \left[\hat{CC} - C \cdot C \right] \\ &= \frac{\sigma^2}{CC \cdot N}. \end{aligned}$$

Similarly, we obtain for parameter b

$$(\Delta b)^2 = \frac{\sigma^2}{SS \cdot N}.$$

When assuming a homogeneous phase coverage, the approximation $CC \approx SS \approx \frac{1}{2}$ can be made[8] and the equations simplify further to

$$(\Delta a)^2 = (\Delta b)^2 = \frac{2\sigma^2}{N} \quad \text{or} \quad \Delta a = \Delta b = \sqrt{\frac{2}{N}} \sigma.$$

[8] Remember that $\int_0^{2\pi} \cos^2 x \, \mathrm{d}x = \int_0^{2\pi} \sin^2 x \, \mathrm{d}x = \frac{1}{2}$.

Error in amplitude A

The amplitude error ΔA for a given frequency ω can be estimated by

$$(\Delta A)^2 = \sum \left(\frac{\partial A}{\partial y_i} \right)^2 \sigma_i^2.$$

With the relation $A^2 = a^2 + b^2$, we find the derivative for the amplitude

$$\partial_{y_i} A = \partial_{y_i} \sqrt{a^2 + b^2} = \frac{1}{A} \left[a \partial_{y_i} a + b \partial_{y_i} b \right].$$

Inserting this, leads to

$$\begin{aligned}(\Delta A)^2 &= \frac{1}{A^2} \sum \left[a \partial_{y_i} a + b \partial_{y_i} b \right]^2 \sigma_i^2 \\ &= \frac{1}{A^2} \left[a^2 \Delta a^2 + b^2 \Delta b^2 + 2ab \sum (\partial_{y_i} a \cdot \partial_{y_i} b) \sigma_i^2 \right].\end{aligned}$$

The last sum vanishes, because

$$\begin{aligned}\sum (\partial_{y_i} YC \cdot \partial_{y_i} YS) \sigma_i^2 &= \sum w_i^2 (\cos \omega t_i \sin \omega t_i - S \cos \omega t_i - C \sin \omega t_i + C \cdot S) \frac{1}{W w_i} \\ &= \frac{1}{W} (\hat{CS} - S \cdot C - C \cdot S + C \cdot S) \\ &= \frac{1}{W} (\hat{CS} - S \cdot C) = \frac{1}{W} CS = 0.\end{aligned}$$

Remember that in our notation $CS = 0$ and τ is suppressed. So the error in the amplitude is

$$(\Delta A)^2 = \frac{\sigma^2}{A^2 N} \left[\frac{a^2}{CC} + \frac{b^2}{SS} \right].$$

Again estimating in the denominator $CC \approx SS \approx \frac{1}{2}$, the bracket term is the twice squared amplitude $2A^2$ and we obtain the simple estimate for the error in the amplitude

$$(\Delta A)^2 = \frac{2\sigma^2}{N} \quad \text{or} \quad \Delta A = \sqrt{\frac{2}{N}} \sigma.$$

Error in phase ϕ

The phase ϕ is given by $\tan \phi = \frac{b}{a}$ and the error propagation for ϕ is

$$(\Delta \phi)^2 = \sum \left(\frac{\partial \phi}{\partial y_i} \right)^2 \sigma_i^2.$$

The derivative $\partial_{y_i} \phi$ can be obtained via implicit differentiation

$$\begin{aligned}\partial_{y_i} \tan \phi = (1 + \tan^2 \phi) \partial_{y_i} \phi = \partial_{y_i} \frac{b}{a} &= \frac{a \partial_{y_i} b - b \partial_{y_i} a}{a^2} \\ \partial_{y_i} \phi = \frac{a \partial_{y_i} b - b \partial_{y_i} a}{(1 + b^2/a^2) a^2} &= \frac{a \partial_{y_i} b - b \partial_{y_i} a}{A^2}.\end{aligned}$$

Inserting and simplifying then yields

$$\begin{aligned}(\Delta \phi)^2 &= \frac{1}{A^4} \sum \left[a \partial_{y_i} b - b \partial_{y_i} a \right]^2 \sigma_i^2 \\ &= \frac{1}{A^4} \left[a^2 \Delta b^2 + b^2 \Delta a^2 \sigma_i^2 - 2ab \sum (\partial_{y_i} a \cdot \partial_{y_i} b) \sigma_i^2 \right] \\ &= \frac{\sigma^2}{A^4 N} \left[\frac{a^2}{SS} + \frac{b^2}{CC} \right]\end{aligned}$$

where it has already been shown that the last sum vanishes. Again with the approximation $CC \approx SS \approx \frac{1}{2}$, the error in phase is

$$(\Delta\phi)^2 = \frac{2\sigma^2}{A^2 N} \quad \text{or} \quad \Delta\phi = \sqrt{\frac{2}{N}}\frac{\sigma}{A}.$$

Error in the offset parameter c

The offset c is given by $c = Y - aC - bS$. The error propagation

$$\Delta c^2 = \sum \left(\frac{\partial c}{\partial y_i}\right)^2 \sigma_i^2$$

then leads to

$$\begin{aligned}
\Delta c^2 &= \sum \left[\partial_{y_i} Y - C\partial_{y_i} a - S\partial_{y_i} b\right]^2 \sigma_i^2 \\
&= \sum \left[(\partial_{y_i} Y)^2 + C^2(\partial_{y_i} a)^2 + S^2(\partial_{y_i} b)^2 - 2C\partial_{y_i} Y\partial_{y_i} a - 2S\partial_{y_i} Y\partial_{y_i} b + 2C\cdot S\partial_{y_i} a\partial_{y_i} b\right] \sigma_i^2 \\
&= \sum w_i^2\sigma_i^2 + C^2(\Delta a)^2 + S^2(\Delta b)^2 - 2C\frac{1}{W\cdot CC}(C-C) - 2S\frac{1}{W\cdot SS}(S-S) \\
&= \frac{\sigma^2}{N}\left[1 + \frac{C^2}{CC} + \frac{S^2}{SS}\right]
\end{aligned}$$

Now we can approximate $C \approx S \approx 0$, which is valid for uniform phase coverage[9]. This results in

$$\Delta c^2 = \frac{\sigma^2}{N} \quad \text{or} \quad \Delta c = \sqrt{\frac{1}{N}}\sigma.$$

Summary and discussion for error estimation

In the previous section we have found that the errors for amplitude, phase, and offset can be estimated by

$$\begin{aligned}
\Delta A &= \sqrt{\frac{2}{N}}\sigma \\
\Delta\phi &= \sqrt{\frac{2}{N}}\frac{\sigma}{A} \\
\Delta c &= \sqrt{\frac{1}{N}}\sigma.
\end{aligned}$$

This is basically the same result as in Montgomery & Odonoghue (1999). The errors depend on the number of measurements N and the measurement noise σ. The quantity σ was derived here employing the mean weights. As a matter of fact, when measurement errors σ_i are correctly estimated, then σ can be interpreted as the true noise level. In the case of a reasonable fit ($\chi^2_{\rm red} \approx 1$) the weighted scatter should be similar to the weighted mean error, i.e. rms $\approx \sigma$, because $\chi^2_{\rm red} = \frac{\rm rms^2}{\sigma^2}$ (Sect. 4.4.1). Practically however, the weights can be arbitrary, under- or overestimated and the remaining scatter should provide a better noise estimate. Hence more generally, in these equations the noise level σ should be replaced with weighted root mean square (wrms) of the residuals.

Note that these simple equations involve approximations which assume a uniform phase coverage or duty cycle. These approximations are, e.g., not valid when the period is longer than the time baseline. Then the equations without approximations should be used to avoid an underestimation of the parameter errors.

[9] $\int_0^{2\pi}\cos x\,\mathrm{d}x = \int_0^{2\pi}\sin x\,\mathrm{d}x = 0$

The estimation of the frequency error is more complicated, because the frequency is a non-linear parameter. Montgomery & Odonoghue (1999) derived

$$\Delta f = \sqrt{\frac{6}{N}} \frac{1}{\pi T} \frac{\sigma}{A} \tag{2.37}$$

which we simply adopt here being aware of the risk of error underestimation for insufficient phase coverage. The frequency error Δf is inversely proportional to the time baseline T, the square root of number of measurements N, and the square root of the signal-to-noise ratio S/N ($= A^2/\sigma^2$). Note that $\frac{1}{T}$ is the typical width of peaks in a periodogram (frequency resolution), but the frequency error can be much smaller.

Gilliland & Fisher (1985) proposed for the frequency error $\Delta f_{\mathrm{Gil}} = \frac{1}{T}\sqrt{\frac{3^2}{4^2 N}\frac{\sigma^2}{A^2} + \frac{0.0256}{(fT)^2}}$. Here the last additive term is supposed to account for the number of covered cycles fT. It is based on the finding by Kovacs (1981) that even noiseless data with one sinusoidal component (finite data set) shows a frequency shift. However, this effect results, because Kovacs (1981) did not account for an offset c. When this term is neglected, only $\Delta f_{\mathrm{Gil}} \approx \frac{3}{4\sqrt{N}} \frac{1}{T} \frac{\sigma}{A}$ remains (Baliunas et al., 1985; Kovacs, 1981) which just differs by a factor of $\frac{\Delta f}{\Delta f_{\mathrm{Gil}}} = \frac{\pi}{4}\sqrt{\frac{3}{2}} \approx 0.96$ from Eq. (2.37).

Kallinger et al. (2008) defined a heuristical frequency error $\Delta f_{\mathrm{Kal}} = \frac{1}{T\sqrt{\mathrm{sig}}}$ for the SigSpec program (see Sect. 2.4 and Reegen 2007). Using the estimate $CC \approx SS \approx \frac{1}{2}$, the least-square fitting amplitude A can be expressed in terms of power p, $A^2 = \frac{YC^2}{CC^2} + \frac{YS^2}{SS^2} \approx 2\left[\frac{YC^2}{CC} + \frac{YS^2}{SS}\right] = 2YY \cdot p$, and the SigSpec indicator (Eq. (2.27)) becomes $\mathrm{sig} \approx \frac{N \log \mathrm{e}}{4} \cdot \frac{A^2}{\langle y^2 \rangle}$. Identifying $\langle y^2 \rangle$ with σ^2, we find $\Delta f_{\mathrm{Kal}} \approx \frac{2}{\sqrt{N \log e}} \frac{1}{T} \frac{\sigma}{A}$ which differs by a factor of $\frac{2\pi}{\sqrt{6 \log e}} \approx 3.89$ from Eq. (2.37). Our simple derivation shows that Δf_{Kal} gives roughly a 4σ-error for the frequency which can also be seen in Fig. 1 of Kallinger et al. (2008). These authors found these results with extensive simulations and denoted their error estimates as upper limits. In the regime of high power, i.e. large S/N, Δf_{Kal} is also overestimated, because the scatter of the time series which includes the signal amplitude is a bad noise estimate ($\sigma \ll$ rms) as mentioned by Kallinger et al. (2008).

2.8.2 A polar grid

In Sect. 2.5 we simply suggested a Cartesian grid to step for the parameters f, e, and T_0 to cover the whole parameter space for the Keplerian periodogram. However, we already argued that a higher grid density might be more appropriate for higher eccentricities. The Cartesian grid has the disadvantage that for low or zero eccentricities too many T_0 are tested. In this section, a polar grid for e and T_0 (or cylindrical grid for f, e, and T_0, respectively) is proposed that overcomes the afore mentioned shortcomings.

The idea originates from the parameter transformation of e and ω to the Lagrangian parameters $h = e\cos\omega$ and $k = e\sin\omega$. This transformation is usually done to circumvent a coordinate singularity that occurs when the eccentricity is close to zero ($e \approx 0$), i.e. for circular orbits. The same circular orbit can be described by various, infinite combinations of ω and T_0 (which can be a problem for backward calculations), while it is unambiguously defined with $h = 0$ and $k = 0$.

The Lagrangian parameter transformation, however, is not so useful for our algorithm to compute the Keplerian periodogram, because ω is solved analytically, while e and T_0 ($x_0 = 2\pi T_0/f$) are solved by stepping. The parametrisation $\hat{h} = e\cos x_0$ and $\hat{k} = e\sin x_0$, on the other hand, has the desired properties. A circular orbit is then also described by the unique grid point ($\hat{h} = 0$, $\hat{k} = 0$). This parametrisation can be easily implemented and now a Cartesian $\hat{h}$-$\hat{k}$ grid would be the simplest choice. Remapping this squarely $\hat{h}$-$\hat{k}$ grid to a e-x_0 grid ($\mathrm{d}\hat{h} = \mathrm{d}\hat{k} = \mathrm{d}e$), such that the same number of grid points is maintained in each grid element, $\mathrm{d}A_{\hat{h}\hat{k}} = \mathrm{d}\hat{h}\,\mathrm{d}\hat{k} = (\mathrm{d}e)^2 \stackrel{!}{=} \mathrm{d}A_{ex_0} = e\,\mathrm{d}e\,\mathrm{d}x_0$, requires $\mathrm{d}x_0 = \frac{1}{e}\mathrm{d}e$ and means that with higher eccentricities e the size for the x_0-steps should decrease or the number of T_0 grid points should linearly increase, respectively.

Figure 2.7 visualises the power map of Fig. 2.4, but this time in polar coordinates which seems to be a better choice. By using this polar grid, the computational effort is redistributed more evenly from

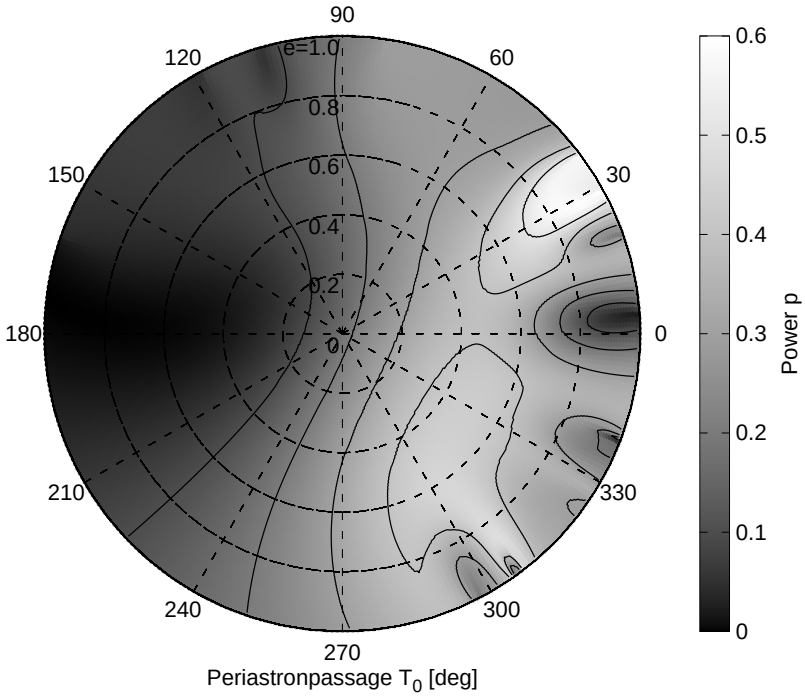

Figure 2.7: The same power map as in Fig. 2.4, but on a polar grid for e and T_0. Note the many narrow features at high eccentricities.

low to high eccentricities. This saves a factor of 2 in computation time. Note, that choosing a two times smaller step size for e (and hence also for x_0) in the polar grid, increases the effort quadratically to a factor of 4.

2.8.3 The F-distribution

In several sections (e.g. Sect. 2.3, 3.3.2, or 4.4) we make use of the F-distribution to derive the probability of a fit improvement. Here we would like to give the equation for the F-distribution and apply it to an example.

As outlined by Cumming et al. (1999), we can employ the quantity

$$z = \frac{\Delta\chi^2/\Delta\nu}{\chi_2^2(\omega_0)/\nu_2}$$

to derive the significance of a fit improvement (cf. Eq. (2.23) and (2.30)). The reduced χ^2 in the denominator is an estimate of the noise (fit residuals χ_2^2 with ν_2 degrees of freedom), while the χ^2 difference in the numerator is an estimate of the pure signal ($\Delta\chi^2 = \chi_1^2 - \chi_2^2(\omega)$ and $\Delta\nu = \nu_1 - \nu_2$). Because both denominator and numerator are χ^2-distributed, their ratio z has the properties of a F-value which follows a F-distribution given by

$$F(z;m,n) = \frac{1}{B(1,\frac{m}{2},\frac{n}{2})} B\left(\frac{mz}{mz+n},\frac{m}{2},\frac{n}{2}\right)$$

where $m = \Delta\nu$ and $n = \nu$. The incomplete beta function $B(x,a,b)$ therein is calculated via

$$B(x,a,b) = \int_0^x t^{a-1}(1-t)^{b-1}\mathrm{d}t.$$

In the case of $m = \Delta\nu = 2$ ($a = 1$), such as the sine fit with an offset ($\nu_2 = N-3$, $\nu_1 = N-1$), the

integration is simple and can be done analytically

$$B(x,1,b) = \int_0^x (1-t)^{b-1}\mathrm{d}t = -\frac{1}{b}(1-t)^b|_0^x = \frac{1}{b}\left(1-(1-x)^b\right)$$
$$B(1,1,b) = \frac{1}{b}.$$

Thus we obtain

$$F(z;2,N-3) = 1-\left(1-\frac{2z}{2z+N-3}\right)^{\frac{N-3}{2}} = 1-\left(1+\frac{2}{N-3}z\right)^{-\frac{N-3}{2}}$$

which is the same result as given Table 2.1 (taken from Cumming et al. 1999) when accounting for $\mathrm{Prob}(z > z_0) = 1 - F(z_0;2,N-3)$.

Chapter 3

The M dwarf planet search programme at the ESO VLT + UVES[1,2]

A search for terrestrial planets in the habitable zone of M dwarfs

From Zechmeister, Kürster, & Endl 2009, A&A, 505, 859

ABSTRACT: We present radial velocity (RV) measurements of our sample of 40 M dwarfs from our planet search programme with VLT+UVES begun in 2000. Although with our RV precision down to 2–2.5 m/s and timebase line of up to 7 years, we are capable of finding planets of a few Earth masses in the close-in habitable zones of M dwarfs, there is no detection of a planetary companion. To demonstrate this we present mass detection limits allowing us to exclude Jupiter-mass planets up to 1 AU for most of our sample stars. We identified 6 M dwarfs that host a brown dwarf or low-mass stellar companion. With the exception of these, all other sample stars show low RV variability with an rms < 20 m/s. Some high proper motion stars exhibit a linear RV trend consistent with their secular acceleration. Furthermore, we examine our data sets for a possible correlation between RVs and stellar activity as seen in variations of the Hα line strength. For Barnard's star we found a significant anticorrelation, but most of the sample stars do not show such a correlation.

3.1 Introduction

High-precision differential radial velocity (RV) measurements of stellar reflex motions induced by an orbiting companion have so far been the most successful method to discover extrasolar planets and to characterise their orbital properties. Originally, RV planet search programmes have largely concentrated on main sequence stars of spectral types late-F through K. That only a comparatively small number of M dwarfs were included comes from their faintness, which requires large telescopes to perform high-precision RV measurements of a few m/s. For an understanding of the formation and abundance of extrasolar planets it is important to determine the presence and orbital characteristics of planets around stars of as many different types as possible, and especially around this most abundant type of star.

Even if M dwarfs are faint and require large telescopes, however, they have two advantageous characteristics when searching for terrestrial exoplanets in the habitable zones (HZ) with radial velocity (RV) methods. Compared to solar-like stars, (i) they have a lower mass ($M = 0.1 - 0.6 M_\odot$), and (ii) the habitable zone is close-in around this cooler and less luminous type of star ($L = 0.0008 - 0.06 L_\odot$, Guinan &

[1]Based on observations collected at the European Southern Observatory, Paranal Chile, ESO programmes 65.L-0428, 66.C-0446, 267.C-5700, 68.C-0415, 69.C-0722, 70.C-0044, 71.C-0498, 072.C-0495, 173.C-0606, 078.C-0829.

[2]Radial velocity data are available in electronic form at the CDS via anonymous ftp to cdsarc.u-strasbg.fr (130.79.128.5) or via http://cdsweb.u-strasbg.fr/cgi-bin/qcat?J/A+A/505/859

Table 3.1: M dwarfs with known planets and their masses discovered with the RV method.

Star	b	c	d	e	References
GJ 876	$2.53 M_{\rm Jup}$	$0.79 M_{\rm Jup}$	$7.53 M_{\oplus}$		[1][2][3][4]
GJ 581	$15.6 M_{\oplus}$	$5.1 M_{\oplus}$	$8.2 M_{\oplus}$	$1.9 M_{\oplus}$	[5][6][7]
GJ 436	$21 M_{\oplus}$				[8]
GJ 317	$0.71 M_{\rm Jup}$				[9]
GJ 674	$11.1 M_{\oplus}$				[10]
GJ 849	$0.82 M_{\rm Jup}$				[11]
GJ 176	$8.4 M_{\oplus}$				[12][13]
GJ 832	$0.64 M_{\rm Jup}$				[14]

Note: The masses are minimum masses with the exception for GJ 436 and GJ 876. [1] Delfosse et al. 1998, [2,3] Marcy et al. 1998, 2001, [4] Rivera et al. 2005, [5] Bonfils et al. 2005, [6] Udry et al. 2007, [7] Mayor et al. 2009a, [8] Butler et al. 2004, [9] Johnson et al. 2007, [10] Bonfils et al. 2007, [11] Butler et al. 2006, [12] Forveille et al. 2009, [13] Butler et al. 2009, [14] Bailey et al. 2009.

Engle 2009). By habitable zone we understand the region that allows liquid water on the planet surface as described in Kasting et al. (1993).

For M dwarfs, the HZ is typically 0.03 – 0.4 AU. The RV amplitude induced due to a planet by the Doppler effect is

$$K = \sqrt{\frac{G}{1-e^2}} \frac{m \sin i}{\sqrt{(M+m)a}} = 28.4 \mathrm{m/s} \cdot \frac{m \sin i}{M_{\rm Jup}} \left(\frac{M_{\odot}}{M} \frac{\mathrm{AU}}{a} \right)^{1/2}. \tag{3.1}$$

It increases for closer distances a (shorter periods) and lower stellar mass M. Thus the RV amplitude induced by a planet in the HZ of an M dwarf is higher than that of a solar-like star. M dwarfs are also ideal targets for astrometric follow-up due to their lower mass, as well as for transit observations. In combination with the RV method, astrometry allows the resolution of the $\sin i$-ambiguity and true masses to be obtained.

At present there are only a few M dwarfs known to have planets, as summarized in Table 3.1. The M4V star GJ 876 has two Jovian planets orbiting in a 2:1 resonance (Marcy et al. 2001; see also Benedict et al. 2002 for an astrometric determination of the mass of the outer planet), and a third planet in this system has been found by Rivera et al. (2005). The M3V star GJ 581 is another multiple system with three Neptune-type planets. The latest detection of a fourth planet in this system by Mayor et al. (2009a) is a new highlight in planet search with RVs. With only $1.9 M_{\oplus}$, GJ 581 e is the lowest-mass planet found so far with the RV method. The same work also resulted in a revised period for the outer planet GJ 581 d, placing it inside the habitable zone. The planet around the M2.5V star GJ 436 first discovered with the RV method (Butler et al., 2004) also turned out to be a transiting one (Gillon et al., 2007). So far it is the only known transiting planet around an M dwarf. Most recently, Bailey et al. (2009) has discovered the first long-period planet around an M dwarf (GJ 832). A planet with a mass of $24.5 M_{\oplus}$ ($P = 10.24$ d) around GJ 176 announced by Endl et al. (2008) is rejected by Forveille et al. (2009) and Butler et al. (2009). Instead, both groups find evidence of another planet with a shorter period (8.78 d) and a minimum mass of $8.4 M_{\oplus}$ (Forveille et al., 2009) and $12 M_{\oplus}$ Butler et al. (2009).

Several radial velocity (RV) surveys of M dwarfs have resulted in few or no detections, indicating a lower frequency of planets compared to solar-like stars; e.g., Endl et al. (2006) monitored 90 M dwarfs (including the first data for 21 stars from our sample) without a planet detection. The sample studied by Cumming et al. (2008) surveying 110 M dwarfs contained only two planet hosting M dwarfs (GJ 876 and GJ 436). HARPS guaranteed time project #3 had 50 nights on 120 M dwarfs within 11 pc, and so far it has revealed only three planet-hosting M dwarfs (GJ 876, GJ 581, and GJ 674).

M dwarfs are an ideal testing ground for competing models of the formation of gas giants. While the classical core-accretion model has severe problems with forming Jupiter-mass planets in the less massive protoplanetary disks even around M dwarfs (e.g. Laughlin et al. 2004), the competing gravitational

instability model can also efficiently form Jovian-type companions around M dwarfs (Boss, 2006). Ida & Lin (2005) even predict a higher frequency of icy giant planets with masses comparable to Neptune in short periodic orbits for M dwarfs than for G type stars.

Recent results of microlensing surveys (e. g. OGLE-2005-BLG-390b, $5.5 M_{\oplus}$, Beaulieu et al. 2006; OGLE-2005-BLG-169b, Gould et al. 2006; presumed M dwarfs) may also indicate that low-mass planetary companions might be abundant around M dwarfs.

3.2 Targets and Observations

Our sample consists of 40 M dwarfs and one M giant[3], which are listed in Table 3.2. All M dwarfs are brighter than $V \lesssim 12.2$ mag and nearby within a distance of 37 pc (33 M dwarfs even within 20 pc). Their spectral types range from M0 to M5. The stellar masses M were derived from the mass-luminosity relation by Delfosse et al. (2000) using the absolute brightness in K band. As an indicator of activity we selected the X-ray luminosity as detected in the ROSAT all-sky survey (from Hünsch et al., 1999). Detected as X-ray sources are Barnard's star ($L_x = 0.1$), GJ 1 (0.6), GJ 190 (0.9), GJ 229 (1.3), and the most active Proxima Cen (1.7). The rest of the sample was not detected by ROSAT, implying that these stars are inactive.

The observations started in 2000, initially with 20 targets. Typically, three consecutive spectra per night were taken for each star with exposure times of 90 – 900 s depending on the object brightness. In April 2004 (JD=2453100) the sample was complemented by 21 additional stars, while the monitoring of HG 7-15 was ended. Since then the number of spectra per night was reduced to one, with the exception of Barnard's star, GJ 160.2, GJ 821, and Proxima Cen.

Our data of the first 20 stars (+ GJ 510) taken before mid-2005 were already included in the study by Endl et al. (2006). Here we present the full data set for all 41 stars as observed until March 2007. A detailed study of the full Proxima Cen data set can be found in Endl & Kürster (2008). A study of the pre-2002.75 data set of Barnard's star is given by Kürster et al. (2003).

The observations were carried out with the UVES spectrograph at the VLT-UT2, directly fed via image slicer #3 that redistributes the light from a $1'' \times 1''$ aperture along a $0.3''$ wide slit. This resulted in a resolving power of $R = 100\,000 - 120\,000$. The red arm of UVES was employed and a wavelength coverage 495–704 nm over 37 orders was selected. An iodine cell was used for precise wavelength calibration and modelling of the instrumental profile. Only the range of 500–600 nm was used to determine the RVs. This range is rich in iodine lines.

The data reduction included bias subtraction, flat-fielding, Echelle straylight subtraction, wavelength calibration, and barycentric correction (see also Endl & Kürster, 2008). The data modelling with the "AUSTRAL" code to obtain the RV is described in Endl et al. (2000). We achieve an RV precision of 2 m/s for bright stars. In practice, photon noise limits the RV precision for faint M dwarfs and correspondingly the errors are larger for those stars that were observed with lower S/N. Radial velocities and also their errors (see Kürster et al. 2003 for discussion) were combined into nightly averages. They are shown in Figs. 3.1 and 3.2 (the RV data are available as online material).

3.3 Data analysis

3.3.1 Secular acceleration

Even if a star moves undisturbed with a constant space velocity v, it can show a change in its radial velocity (RV). This secular or perspective acceleration was first measured by Kürster et al. (2003) for Barnard's star. In polar coordinates the radial and tangential velocity component, respectively, are (Fig. 3.3)

$$v_{\rm r} = -v\cos\varphi \quad \text{and} \quad v_{\rm t} = v\sin\varphi.$$

[3] GJ 4106 is listed in the Catalogue of Nearby Stars with a parallax of 84 ± 17 mas (11.9 pc). However, with the Hipparcos parallax GJ 4106 should be an M giant.

Table 3.2: Targets with their spectral type, visual magnitude V, distance d (van Leeuwen, 2007), and stellar mass M derived from the K-band mass-luminosity relation by Delfosse et al. (2000).

Star	Spec Type	V [mag]	d [pc]	M [$M_\odot$]
Barnard (GJ 699)	M4Ve	9.54	1.82	0.16
GJ 1	M1.5	8.57	4.34	0.45
GJ 27.1	M0.5	11.42	23.99	0.53
GJ 118	M2.5	10.70	11.65	0.36
GJ 160.2	M0V	9.69	23.12	0.69
GJ 173	M1.5	10.35	11.10	0.48
GJ 180	M2	12.50	12.12	0.43
GJ 190	M3.5	10.31	9.27	0.44
GJ 218	M1.5	10.72	15.03	0.50
GJ 229	M1/M2V	8.14	5.75	0.58
GJ 263	M3.5	11.29	16.02	0.55
GJ 357	M2.5V	10.85	9.02	0.37
GJ 377	M3	11.44	16.29	0.52
GJ 422	M3.5	11.66	12.67	0.35
GJ 433	M1.5	9.79	8.88	0.48
GJ 477	M1	11.08	18.99	0.54
GJ 510	M1	11.05	16.74	0.49
GJ 620	M0	10.25	16.44	0.61
GJ 637	M0.5	11.36	15.88	0.41
GJ 682	M3.5	10.96	5.08	0.27
GJ 739	M2	11.14	14.09	0.45
GJ 817	M1	11.48	19.17	0.43
GJ 821	M1	10.87	12.17	0.44
GJ 842	M0.5	9.74	11.99	0.58
GJ 855	M0.5	10.74	19.15	0.60
GJ 891	M2V	12.20	16.08	0.35
GJ 911	M0V	10.88	24.26	0.63
GJ 1009	M1.5	11.16	17.98	0.56
GJ 1046	M2.5+v	11.62	14.07	0.40
GJ 1100	M0	11.48	28.93	0.57
GJ 3020	M2.5	11.54	22.78	0.62
GJ 3082	M0	11.10	16.56	0.47
GJ 3098	M1.5Vk:	11.21	17.86	0.50
GJ 3671	M0	11.20	17.74	0.50
GJ 3759	M1V	10.95	16.97	0.49
GJ 3916	M2.5V	11.25	15.10	0.49
GJ 3973	M1.5Vk:	10.94	18.23	0.54
GJ 4106	M2	10.82	110.50	0.55
GJ 4293	M0.5	10.90	25.06	0.57
HG 7-15	M1V	10.85	37.31	0.78
Prox Cen (GJ 551)	M5.5Ve	11.05	1.30	0.12

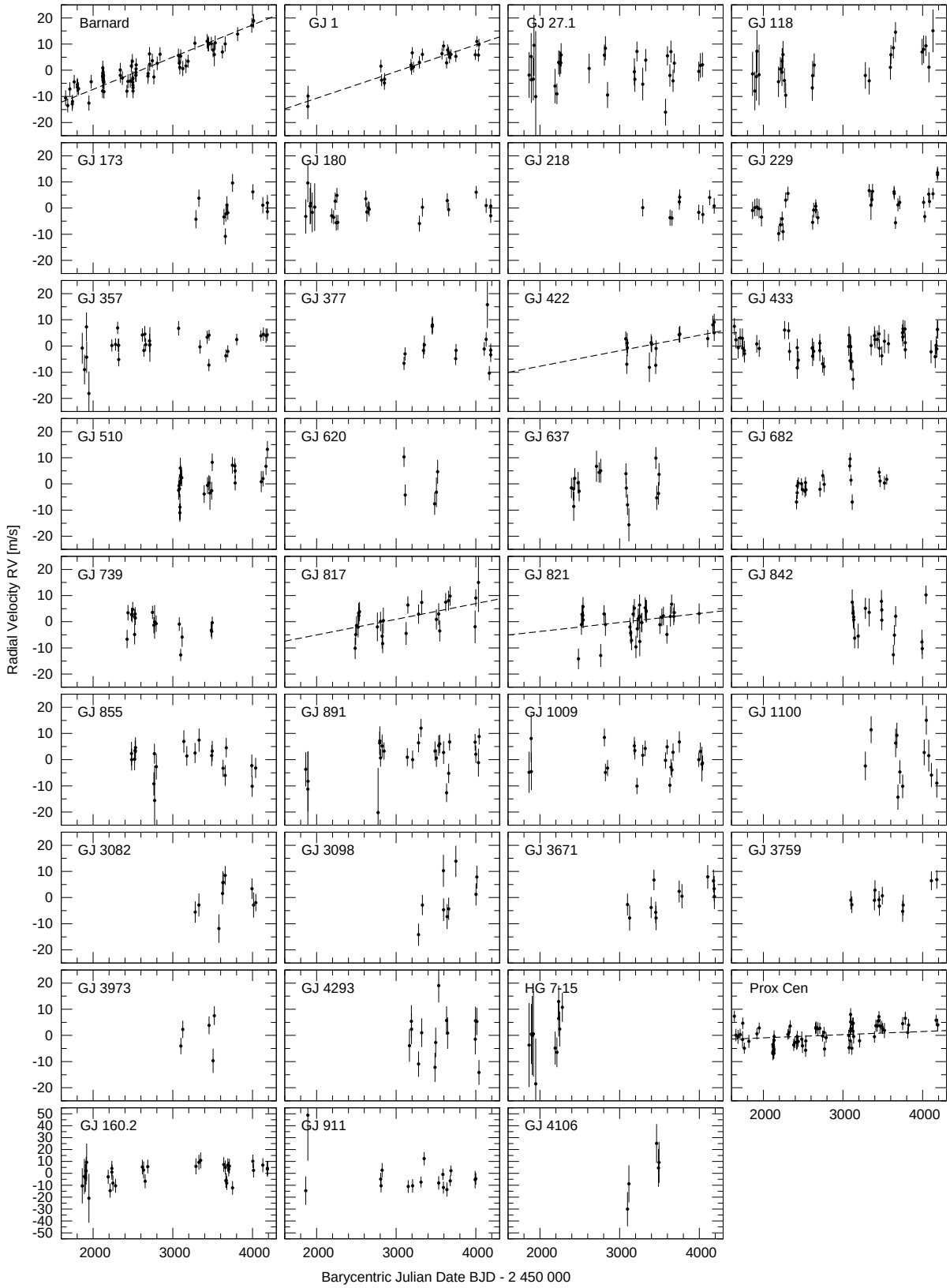

Figure 3.1: Radial velocities for 35 M dwarfs. Dashed lines represent no fit; they show the predicted secular acceleration effect caused by the proper motion (only for Proxima Cen and stars with $\dot{v}_{\rm r} > 1\,$m/s/yr).

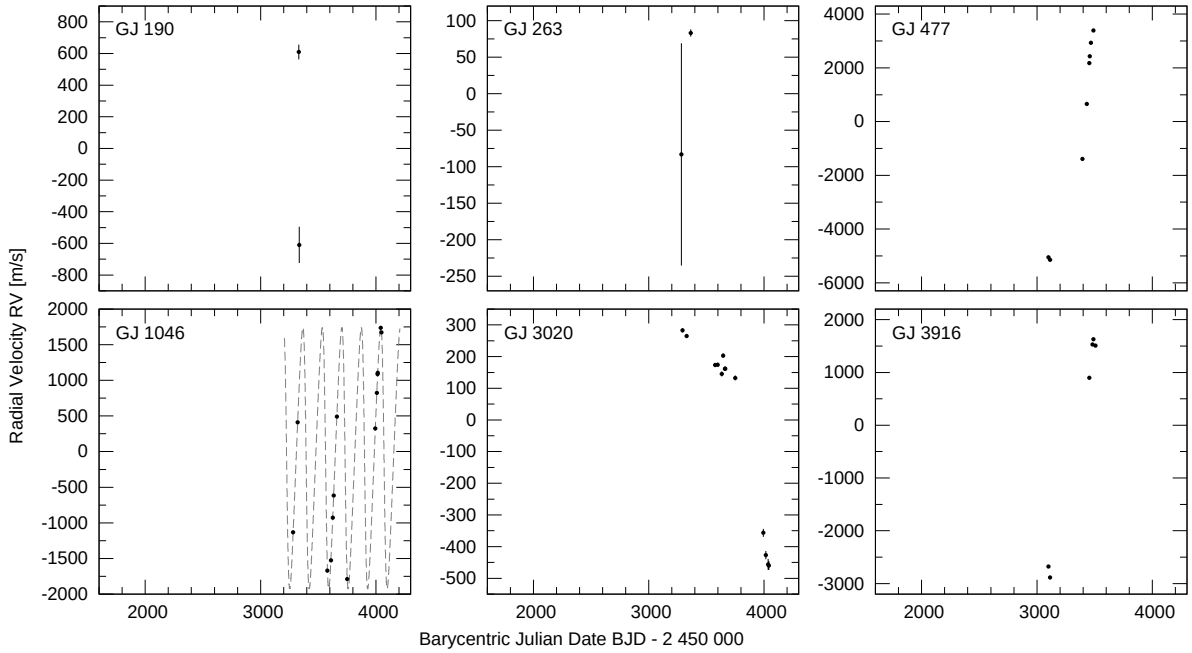

Figure 3.2: Radial velocities for 6 more M dwarfs. The orbital solution for GJ 1046 is taken from Kürster et al. (2008).

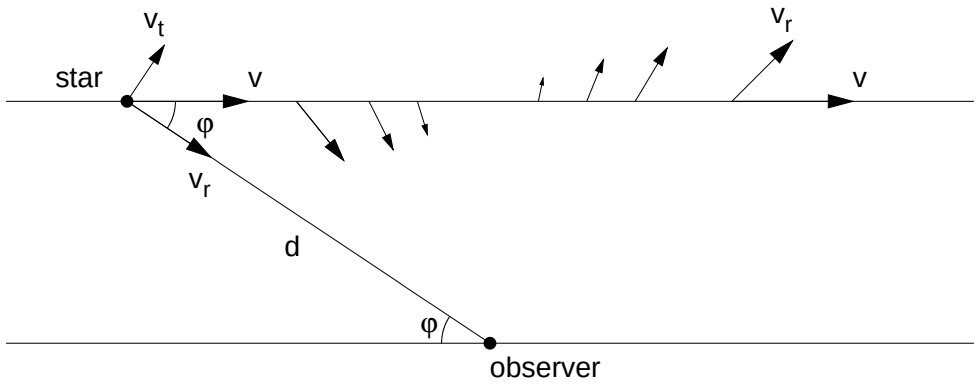

Figure 3.3: Change in the radial velocity v_r due to constant motion v (secular acceleration $\dot{v}_r$).

The differentiation of v_r with respect to time t yields the secular acceleration ($v = \text{const.}$)

$$\dot{v}_\mathrm{r} = \frac{\mathrm{d}v_\mathrm{r}(t)}{\mathrm{d}t} = v \sin\varphi \cdot \dot{\varphi} = v_\mathrm{t}\dot{\varphi}.$$

The tangential velocity $v_\mathrm{t} = d \cdot \mu$ depends on the distance d of the star and its proper motion μ, which can also be identified with the time derivative of the angular position $\dot{\varphi} = \mu$. Therefore the instantaneous secular acceleration is given by

$$\frac{\mathrm{d}v_\mathrm{r}(t)}{\mathrm{d}t} = \frac{v_\mathrm{t}^2}{d} = \mu^2 d = 22.98 \frac{\mathrm{m/s}}{\mathrm{yr}} \frac{(\mu_\alpha^2 + \mu_\delta^2) \cdot \mathrm{yr}^2/\mathrm{arcsec}^2}{\pi/\mathrm{mas}}. \tag{3.2}$$

where μ_α and μ_δ are the proper motion in right ascension and declination, respectively. It only depends on the proper motion μ and parallax π, which are easily accessible from the Hipparcos catalogue. Note that the knowledge of v_r and v is *not* explicitly required for the prediction of the instantaneous secular acceleration.

One has to take this effect into account, especially for high proper motion stars, to avoid the misleading conclusion that this RV change is a disturbance by a companion. A feature of the secular acceleration is that this effect is only geometrical, not physical, and always positive ($\dot{v}_r \geq 0$). With the high astrometric precision of Hipparcos, this effect can be predicted with high accuracy for nearby stars.

Table 3.3 lists the prediction for secular acceleration for all of our sample stars as derived from Eq. (3.2). Some stars (e.g. Barnard's star, GJ 1, and Proxima Cen) have such high proper motion that the secular acceleration can be measured (4.5, 3.7, and 0.4 m/s/yr, respectively). This effect is depicted with a dashed line for Proxima Cen and for all stars with $\dot{v}_r > 1\,\mathrm{m/s/yr}$ in Fig. 3.1. The secular acceleration was subtracted before subsequent analysis of the RV data.

We note that, even though Barnard's star has the highest (angular) proper motion μ and the dependence is quadratic on μ, it is *not* the star with the highest secular acceleration. When inspecting high proper motion stars from the Hipparcos catalogue (van Leeuwen, 2007) we found four stars that have a higher secular acceleration because of their smaller parallax (see lower part of Table 3.3), namely: GJ 451 (Groombridge 1830, G8Vp + M5.5V), GJ 9511 (K2V + K2Vfe), GJ 191 (Kapteyn's star, M1V), and GJ 9371 (sdK4).

3.3.2 Tests for variability and trends

Following the recipe outlined by Endl et al. (2002), we performed several statistical tests to identify variability and RV trends in our data. First, we asked the question for each star of whether the observed variability or rms σ is significantly higher than the mean measurement error $\overline{\sigma_{RV}}$ using the F-Test (and $F = \frac{\sigma^2}{\overline{\sigma_{RV}}^2}$ as F-value)[4].

The calculated probabilities $P(F)$ from the F-Test are listed in Table 3.4 for each star. A low value of $P(F)$ (e.g. < 0.01, i.e. 99% confidence, in bold face in Table 3.4) indicates that the observed scatter can probably not be explained with the measurement errors and that there is an excess variability or a trend. This is the case for the stars with a high rms (GJ 477, GJ 1046, GJ 3020, and GJ 3916), which seem to have a companion, probably in the brown dwarf or low-mass star regime (see also Fig. 3.2). GJ 190 and GJ 263 also have a high sample variance. They may have a stellar companion bright enough to contaminate the spectrum. We deduce this from the large measurement error that would occur for a double-lined spectroscopic binary (SB2) because our data modelling is only designed for a single-lined spectroscopic binary (SB1). Also, because there are only two measurements for GJ 190 and GJ 263, they do not stand out in the F-statistics. Indeed GJ 263 has already been identified as a spectroscopic binary, and an adaptive optics image was presented by Beuzit et al. (2004). Among the stars with an rms smaller than 20 m/s, only GJ 229, GJ 357, and Proxima Cen have an rms that is significantly greater than the measurement error.

A similar test for RV variability is to determine the goodness of fit for a constant model, i.e. calculating the χ^2 above the weighted RV mean[5] and deriving the probability from the χ^2-distribution. These probability values $P(\chi^2_{\mathrm{const}})$ are mostly lower than $P(F)$, and therefore there would be more variable stars according to our $P < 0.01$ criterion (Table 3.4).

As long-period planets can cause a trend in the RV, we also tested for this by weighted fitting of a linear slope. A high probability of the resulting χ^2_{slope} indicates that this is an acceptable fit (on the contrary, a low probability indicates remaining variability). But it is also informative to compare χ^2_{slope} with the χ^2_{const} of the weighted mean via the F-value (Cumming et al., 1999)

$$F_{\mathrm{slope}} = (N-2)\frac{\chi^2_{\mathrm{constant}} - \chi^2_{\mathrm{slope}}}{\chi^2_{\mathrm{slope}}}.$$

[4] We use the one-tailed F-test because we are not interested in cases of error overestimation.

[5] When each measurement has the same error σ_{RV}, one gets

$$\chi^2_{\mathrm{red}} = \frac{\chi^2_{\mathrm{const}}}{N-1} = \frac{1}{(N-1)\sigma^2_{RV}} \sum (RV_i - \overline{RV})^2 = \frac{\sigma^2}{\sigma^2_{RV}} = F.$$

Table 3.3: Proper motion μ, parallax π (from Hipparcos, van Leeuwen 2007) and secular acceleration (SA) $\dot{v}_r(t)$ for the M dwarfs sample, with the highest SA stars in the lower part of the table for comparison (not in our sample).

Star	μ_α [mas/yr]	μ_δ [mas/yr]	π [mas]	$\dot{v}_r(t)$ [m/s/yr]
Barnard	-798.58±1.72	10328.12±1.22	548.31±1.51	4.497±0.012
GJ 1	5634.68±0.86	-2337.71±0.71	230.42±0.90	3.711±0.015
GJ 27.1	485.57±2.81	-223.13±2.11	41.69±2.80	0.157±0.011
GJ 118	978.61±2.27	633.21±2.64	85.87±1.99	0.364±0.008
GJ 160.2	51.90±1.24	-780.04±1.57	43.25±1.61	0.325±0.012
GJ 173	-225.75±1.94	-192.57±1.88	90.10±1.74	0.022±0.000
GJ 180	408.07±2.49	-642.82±2.06	82.52±2.40	0.161±0.005
GJ 190	502.99±1.32	-1399.76±1.52	107.85±2.10	0.471±0.009
GJ 218	768.13±1.39	-123.17±1.54	66.54±1.43	0.209±0.005
GJ 229	-137.09±0.50	-713.66±0.81	173.81±0.99	0.070±0.000
GJ 263	-123.73±3.68	-814.92±2.87	62.41±3.16	0.250±0.013
GJ 357	136.67±1.53	-989.13±1.41	110.82±1.92	0.207±0.004
GJ 377	-1096.84±2.11	647.29±2.63	61.39±2.55	0.607±0.025
GJ 422	-2466.98±2.87	1180.09±2.17	78.91±2.60	2.178±0.072
GJ 433	-72.51±1.49	-851.92±0.88	112.58±1.44	0.149±0.002
GJ 477	-101.39±2.28	-697.57±1.75	52.67±3.05	0.217±0.013
GJ 510	-452.04±2.55	-104.79±1.55	59.72±2.43	0.083±0.003
GJ 620	-348.40±2.35	-675.73±1.87	60.83±2.06	0.218±0.007
GJ 637	-480.59±1.17	-529.12±1.86	62.97±1.99	0.186±0.006
GJ 682	-708.98±2.55	-937.40±1.88	196.90±2.15	0.161±0.002
GJ 739	153.46±2.91	-495.17±1.98	70.95±2.56	0.087±0.003
GJ 817	-918.58±3.68	-2038.13±2.50	52.16±2.92	2.202±0.123
GJ 821	713.47±2.82	-1994.64±0.95	82.18±2.17	1.255±0.033
GJ 842	888.07±1.31	-125.56±1.16	83.43±1.77	0.222±0.005
GJ 855	587.72±2.17	-376.75±1.32	52.22±2.17	0.214±0.009
GJ 891	717.43±3.40	22.12±2.69	62.17±3.27	0.190±0.010
GJ 911	-42.36±3.32	128.87±2.44	41.22±2.64	0.010±0.001
GJ 1009	62.95±2.45	-196.98±2.46	55.62±2.32	0.018±0.001
GJ 1046	1395.67±1.72	547.16±2.52	71.06±3.23	0.727±0.033
GJ 1100	118.29±2.67	-498.47±1.30	34.57±2.79	0.174±0.014
GJ 3020	-44.73±4.05	-237.17±3.70	43.89±4.39	0.030±0.003
GJ 3082	104.14±2.04	311.53±1.81	60.38±1.81	0.041±0.001
GJ 3098	-589.19±1.86	-887.83±1.24	55.98±1.91	0.466±0.016
GJ 3671	-603.54±1.64	-296.43±1.36	56.38±2.04	0.184±0.007
GJ 3759	-391.22±1.50	-411.01±1.71	58.94±2.40	0.126±0.005
GJ 3916	-332.19±2.90	-352.83±2.62	66.21±3.18	0.082±0.004
GJ 3973	-9.48±2.45	-221.00±1.72	54.86±2.18	0.020±0.001
GJ 4106	31.55±4.63	-104.82±3.59	9.05±3.70	0.030±0.012
GJ 4293	198.08±2.42	-113.57±2.08	39.90±3.04	0.030±0.002
HG 7-15	176.02±2.85	5.73±1.79	26.80±2.05	0.027±0.002
Prox Cen	-3775.75±1.63	765.54±2.01	771.64±2.60	0.442±0.002
GJ 451 A	4003.98±0.37	-5813.62±0.23	109.99±0.41	10.411±0.039
GJ 9511 B	-999.75±1.29	-3542.60±1.13	35.14±1.48	8.861±0.373
GJ 9511 A	-997.47±1.20	-3543.55±1.03	34.65±1.28	8.988±0.332
GJ 191	6505.08±0.98	-5730.84±0.96	255.66±0.91	6.756±0.024
GJ 9371	264.99±2.23	-3157.36±2.30	42.79±2.70	5.391±0.340

Table 3.4: Tests for variability and trends.

Star	N	T [d]	σ [m/s]	$\overline{\sigma_{RV}}$ [m/s]	$P(F)$	$\chi^2_{\rm const}$	$P(\chi^2_{\rm const})$	Comment
Barnard	75	2358	3.3	2.7	0.065	114	**0.0022**	
GJ 1	24	2151	2.5	2.4	0.9	27.3	0.24	
GJ 27.1	30	2177	6.1	6.1	0.95	41.2	0.066	
GJ 118	26	2266	6.5	5.8	0.56	40.5	0.026	
GJ 160.2	33	2325	8.1	7.7	0.79	41.1	0.13	
GJ 173	12	897	5.3	3.1	0.094	30.6	**0.0013**	
GJ 180	24	2325	3.8	4.1	0.71	29.4	0.17	
GJ 190	2	4	861.8	80.7	0.12	97.4	$< \mathbf{10^{-7}}$	SB2
GJ 218	9	896	3.1	3.1	0.98	8.49	0.39	
GJ 229	32	2325	5.5	2.8	**0.00036**	139	$< \mathbf{10^{-7}}$	
GJ 263	2	82	117.6	78.6	0.75	1.19	0.27	SB2
GJ 357	30	2321	5.3	3.2	**0.0096**	59.9	**0.00064**	
GJ 377	14	1089	6.7	3.2	0.014	40	**0.00014**	
GJ 422	15	1112	4.0	3.4	0.55	16.8	0.27	
GJ 433	54	2554	4.4	3.6	0.16	80	**0.0097**	
GJ 477	8	389	3486.0	4.3	$\mathbf{1.6 \cdot 10^{-19}}$	$5.58{\cdot}10^6$	$< \mathbf{10^{-7}}$	SB1
GJ 510	23	1115	5.6	3.5	0.039	54	**0.00016**	
GJ 620	5	422	7.3	4.4	0.36	13.1	0.011	
GJ 637	17	1099	6.4	4.4	0.16	27	0.041	
GJ 682	20	1134	4.0	2.3	0.024	53.8	$\mathbf{3.6 \cdot 10^{-5}}$	
GJ 739	19	1070	4.4	3.1	0.13	48.8	**0.00012**	
GJ 817	25	1551	4.9	4.3	0.54	32.2	0.12	
GJ 821	35	1516	5.0	3.8	0.12	53.7	0.017	
GJ 842	17	926	6.7	4.2	0.065	44.6	**0.00016**	
GJ 855	22	1561	5.8	4.5	0.24	28.7	0.12	
GJ 891	25	2178	7.5	5.1	0.068	48.4	**0.0023**	
GJ 911	17	2136	14.9	7.7	0.012	25.2	0.067	
GJ 1009	22	2177	5.3	4.0	0.23	47.8	**0.00074**	
GJ 1046	14	766	1248.3	3.6	$\mathbf{1.9 \cdot 10^{-30}}$	$1.59{\cdot}10^6$	$< \mathbf{10^{-7}}$	SB1 (BD)
GJ 1100	12	897	9.3	5.1	0.061	37	**0.00011**	
GJ 3020	13	749	298.8	9.0	$\mathbf{5 \cdot 10^{-16}}$	$7.62{\cdot}10^3$	$< \mathbf{10^{-7}}$	SB1
GJ 3082	10	761	6.2	4.2	0.27	17.5	0.041	
GJ 3098	9	733	9.1	4.7	0.079	26.7	**0.00081**	
GJ 3671	12	1090	5.6	4.4	0.46	17.4	0.095	
GJ 3759	11	1080	3.9	3.6	0.81	11.5	0.32	
GJ 3916	6	406	2170.7	9.2	$\mathbf{1.5 \cdot 10^{-11}}$	$4.07{\cdot}10^5$	$< \mathbf{10^{-7}}$	SB1
GJ 3973	5	420	6.8	3.6	0.25	12	0.017	
GJ 4106	5	396	20.7	15.9	0.62	7.4	0.12	giant
GJ 4293	14	875	8.7	5.6	0.13	32.3	**0.0021**	
HG 7-15	11	417	8.7	10.3	0.59	11	0.36	
Prox Cen	76	2555	3.6	2.3	**0.00028**	183	$< \mathbf{10^{-7}}$	

Listed are the number of measurements N, time baseline T, RV scatter σ (rms), mean RV measurement error $\overline{\sigma_{RV}}$, and results of statistical tests. Low values of the F-test probability $P(F)$, as well as $P(\chi^2_{\rm const})$, e.g. <0.01, mean that a constant model is improbable, hence indicate variability (values in bold fonts). In contrast, a high $P(\chi^2_{\rm slope})$ indicates that a trend is an acceptable model while a small $P(F_{\rm slope})$ indicates a significant fit improvement.

Table 3.5: Contination of Table 3.4.

Star	Slope [m/s/yr]	$\chi^2_{\rm slope}$	$P(\chi^2_{\rm slope})$	$P(F_{\rm slope})$	Comment
Barnard	-0.688	99.4	**0.022**	**0.0038**	
GJ 1	-0.454	25.9	**0.26**	0.56	
GJ 27.1	0.122	41.1	**0.052**	0.32	
GJ 118	1.99	23.8	**0.47**	**0.00083**	
GJ 160.2	1.36	35.5	**0.26**	0.067	
GJ 173	1.61	28.7	0.0014	0.86	
GJ 180	0.418	27.5	**0.19**	0.46	
GJ 190	$-1.12\cdot10^5$	0	$< 10^{-7}$	$< \mathbf{10^{-7}}$	SB2
GJ 218	1.03	7.96	**0.34**	0.96	
GJ 229	1.43	95.6	$< 10^{-7}$	**0.0017**	
GJ 263	743	0	$< 10^{-7}$	$< \mathbf{10^{-7}}$	SB2
GJ 357	0.393	57.5	0.00084	0.58	
GJ 377	-0.284	39.8	$7.7\cdot10^{-5}$	0.36	
GJ 422	0.599	16.2	**0.24**	0.99	
GJ 433	0.284	78.4	**0.011**	0.61	
GJ 477	$6.99\cdot10^3$	$4.52\cdot10^5$	$< 10^{-7}$	**0.00034**	SB1
GJ 510	2.64	37.9	**0.013**	0.014	
GJ 620	-5.1	11	**0.012**	0.98	
GJ 637	0.305	26.9	**0.03**	0.38	
GJ 682	1.62	40.8	0.0016	0.056	
GJ 739	-2.09	37.4	0.003	0.072	
GJ 817	0.184	32.1	**0.098**	0.42	
GJ 821	-0.268	53.5	**0.013**	0.56	
GJ 842	-1.2	43.5	0.00013	0.91	
GJ 855	-1.14	24.9	**0.21**	0.19	
GJ 891	0.556	47.6	0.0019	0.93	
GJ 911	0.389	25.1	**0.049**	0.38	
GJ 1009	0.0316	47.8	0.00046	0.055	
GJ 1046	$1.09\cdot10^3$	$8.8\cdot10^5$	$< 10^{-7}$	0.018	SB1 (BD)
GJ 1100	-1.67	36.3	$7.4\cdot10^{-5}$	0.66	
GJ 3020	-287	$2.29\cdot10^3$	$< 10^{-7}$	**0.00074**	SB1
GJ 3082	1.19	17.1	**0.029**	0.66	
GJ 3098	7.05	16	**0.025**	0.13	
GJ 3671	3.26	10.2	**0.43**	0.046	
GJ 3759	2.48	6.84	**0.65**	0.071	
GJ 3916	$4.1\cdot10^3$	$2.12\cdot10^3$	$< 10^{-7}$	$\mathbf{2\cdot10^{-5}}$	SB1
GJ 3973	3.3	10.8	**0.013**	0.78	
GJ 4106	32.2	1.99	**0.58**	0.13	giant
GJ 4293	-0.114	32.3	0.0012	0.064	
HG 7-15	10.5	9.03	**0.43**	0.39	
Prox Cen	0.703	159	$< 10^{-7}$	**0.0026**	

A high $F_{\rm slope}$-value indicates a fit improvement whereas a low probability $P(F_{\rm slope})$ shows this improvement to be significant and that it is probable not due to noise.

In Table 3.4 the stars with a significant trend are marked in bold face. Besides the companion hosting M dwarfs GJ 477, GJ 3020, and GJ 3916, these are the stars Barnard's star, GJ 118, GJ 229, and Proxima Cen. The significant trend of 1.4 m/s/yr for GJ 229 may be caused by the wide T7p brown dwarf companion GJ 229 B, as one can show with a rough estimate. Assuming a circular orbit and the projected separation of 45 AU ($\alpha = 7.7''$ Nakajima et al. 1995, $\pi = 0.173''$) as the orbital radius to GJ 229, the orbital period is of the order of $P = 400$ yr. Then a $30\,M_{\rm Jup}$ companion can cause a velocity amplitude of $K = 170$ m/s (Eq. (3.1)) and the maximum RV change is $\dot{RV} = K\frac{2\pi}{P} = 2.7\,{\rm m/s/yr}$, about twice as large as the observed trend. However, the low $P(\chi^2_{\rm slope})$ indicates there is still some variability after trend subtraction.

3.3.3 Periodogram analysis

To test for periodicities in the RV data, we computed the generalized Lomb-Scargle periodogram (GLS, Zechmeister & Kürster 2009), which is the equivalent of fitting sine waves including an offset. The adopted period search interval ranges from 2 d to the time baseline T of each data set. Note that 2 d will mostly exceed the average Nyquist frequency. However, searching at frequencies higher than the Nyquist frequency is possible for irregular sampling (Pelt, 2009). False-alarm probabilities (FAP) were determined by bootstrap randomization (e.g. Kürster et al., 1997). In this method random data sets are generated from an original data set by shuffling the RVs while retaining the observing times. For each random data set, the GLS periodogram was computed and searched for its maximum. The FAP is then given by that fraction of random data sets having a periodogram power higher than the original one. For each star we generated 1000 random data sets which resolves FAP $> 10^{-3}$ and is sufficient to decide whether the FAP is below our threshold of 0.01.

Table 3.6 shows that GJ 4106 and GJ 1046 have a FAP marginally lower than 0.01. The probable brown dwarf companion to GJ 1046 with a minimum mass of $26.9\,M_{\rm Jup}$ in an eccentric orbit ($e = 0.28$) with a 168.8 d period has been already published by Kürster et al. (2008) based on this UVES data set. For the 365 d period in Proxima Cen we refer to Endl & Kürster (2008), who recently analysed the RV data and identified this period as a 1-year alias.

Based on data from the first 2 1/2 yr, Kürster et al. (2003) determined two RV periods of 32 d and 45 d for Barnard's star with a FAP of 0.56% and 1.05%, respectively. Now, in the enlarged data set with a 6 1/2 yr time baseline, the second period (45 d; with an amplitude of 2.9 m/s) has the highest periodogram peak, and its FAP is now less than 0.1%, i.e. more significant (see Fig. 3.4, second panel for the periodogram and Fig. 3.5 for the RVs phased to this period). However, stellar activity is the probable cause of this variability and will be discussed in Sect. 3.3.5.

3.3.4 Upper detection limits

A Jupiter-mass planet in a circular orbit with a radius of 1 AU around a $0.4\,M_{\odot}$-M dwarf would cause an RV amplitude of 45 m/s (even higher for closer orbits; Eq. (3.1)) and would be easily detectable with our precision of typically a few m/s. However, most of our sample stars show low RV-variations and no indication of a planet. To determine which planets in circular orbits can be excluded, we calculated detection limits in the following way.

We considered the data as noise and simulated planetary signals by adding sine waves to the data with a range of trial frequencies and for 12 different equidistant phases. The time sampling remained unaffected. For the simulated data the generalised Lomb-Scargle periodogram power was calculated at the trial sine wave frequency where the peak of the signal is expected. If this power was below a power threshold (which corresponds to an FAP of 0.01, see note below), we increased the amplitude of the sine wave. The simulated planet is considered as detected, if the power is in all 12 phases (equal to or) higher than the threshold. The corresponding amplitude is considered as the 99% detection limit. In Appendix 3.6.2 we provide an analytic solution to calculate this amplitude for a given power threshold

Table 3.6: Test for periodicities in the RV (GJ 190 and GJ 263 excluded): the best period P with its χ^2 and bootstrapped FAP.

Star	P [d]	$\chi^2_{\rm sin}$	FAP
Barnard	44.9	72.5	$< \mathbf{10^{-4}}$
GJ 1	2.73	12.5	0.733
GJ 27.1	2.01	18	0.189
GJ 118	3.97	15.6	0.329
GJ 160.2	4.15	20.7	0.577
GJ 173	2.28	3.67	0.026
GJ 180	5.93	8.63	0.127
GJ 218	2.02	0.473	0.557
GJ 229	10.9	63.7	0.102
GJ 357	3.41	28.4	0.157
GJ 377	15.1	7.47	0.029
GJ 422	8.82	4.69	0.498
GJ 433	6.5	55.6	0.451
GJ 477	243	$1.58 \cdot 10^5$	0.541
GJ 510	2.92	29.1	0.867
GJ 620	2.51	0.00667	0.637
GJ 637	8.54	8.54	0.245
GJ 682	89.3	20.1	0.178
GJ 739	2.34	16.3	0.334
GJ 817	2.36	15.1	0.743
GJ 821	12.6	32.9	0.393
GJ 842	92.6	10.8	0.219
GJ 855	16	12.6	0.668
GJ 891	30.5	22.1	0.36
GJ 911	2.35	9.85	0.909
GJ 1009	3.73	17.1	0.502
GJ 1046	174	$1.23 \cdot 10^5$	**0.008**
GJ 1100	3.79	5.27	0.477
GJ 3020	5.14	$3.03 \cdot 10^3$	0.895
GJ 3082	3.72	1.7	0.261
GJ 3098	2.7	2.23	0.5
GJ 3671	68.1	1.69	0.218
GJ 3759	2.46	1.8	0.769
GJ 3916	8.6	82.5	0.077
GJ 3973	2.25	0.00154	0.105
GJ 4106	2.41	0.000139	**0.009**
GJ 4293	19.1	11	0.994
HG 7-15	4.55	0.919	0.179
Prox Cen	365	101	$< \mathbf{10^{-4}}$

and phase. This procedure was performed for a number of trial frequencies resulting in amplitude limits which finally were translated into mass upper limits (Fig. 3.6) using Eq. (3.1) and the stellar masses from Table 3.2.

It should be noted that the periodogram power p is a measure/quantity for the FAP. By applying bootstrap randomisation to the original data we get a FAP vs. power relation $p(FAP)$. No assumptions are necessary about the number of independent frequencies. The power value for FAP=0.01 was also taken

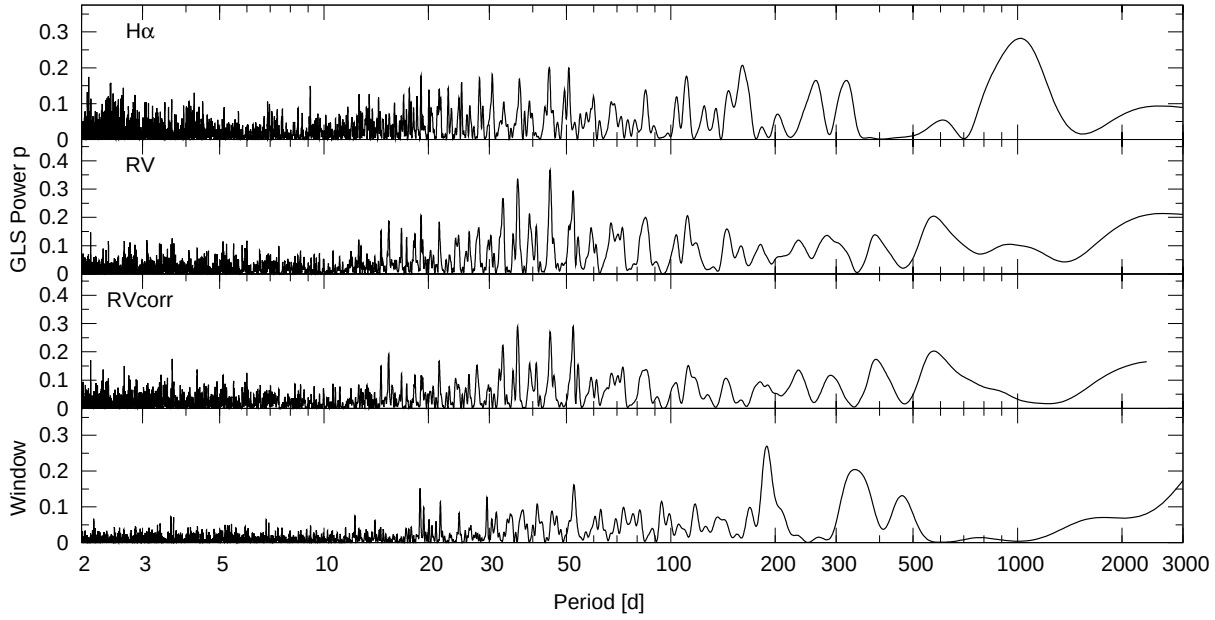

Figure 3.4: GLS periodograms for the Hα-index (top panel; see Sect. 3.3.5), the RV data (second panel), the RV data corrected for a Hα correlation (third panel), and window function (bottom) of Barnard's star.

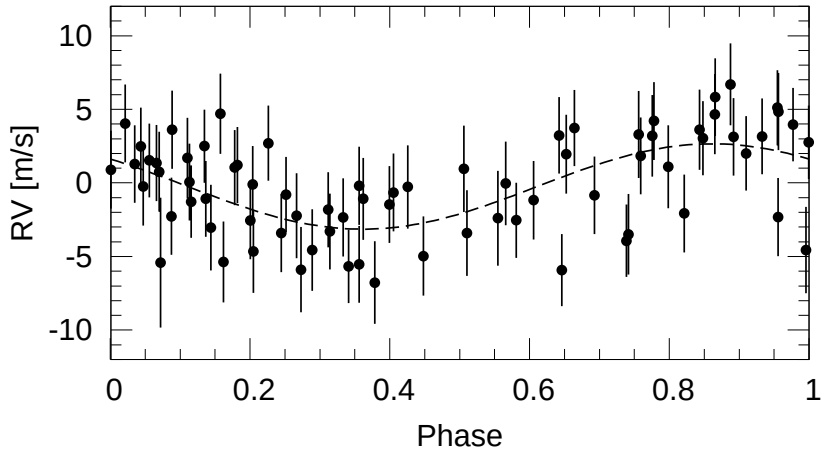

Figure 3.5: Radial velocity time series for Barnard's star phased to the 44.9 d period and the best-fitting sinusoid.

as the threshold for the simulated data. This modification to the method by Endl et al. (2002) bypasses bootstrapping the simulated data again and is therefore more efficient and allows a dense sampling of the frequency.

Here we assume that the $p(FAP)$ relation does not change much when adding a sine wave, because the time sampling and number of measurements does not change. The only thing that can happen is that the rms (or χ^2 above the mean) of the simulated data changes (increases) by a certain factor. But as the normalized power is invariant when the measurements are scaled the resulting effect is small. A comparison of the detections limits given in Fig. 3.6 with those from Endl & Kürster (2008) for Proxima Cen shows quite similar results. Figure 3.6 also shows the steep increase that generally appears for periods longer than the time base (see also Cumming 2004; Nelson & Angel 1998).

Instead of again searching the whole frequency range, only the power at the original sine frequency was calculated, since one can expect to find the simulated signal there. This saves computational effort

and is more conservative, because we exclude spurious detections that exceed the power threshold with a lower amplitude at alias or noise frequencies.

Figure 3.6 shows the results of our detection limit calculation. It can be seen that for Barnard's star or Proxima Cen, i.e. stars with low masses and many measurements, the detection limit reaches down to a few Earth masses for close-in circular orbits and even within their habitable zones (HZ). Both stars have a priori frequencies with a FAP<0.01. These frequencies were excluded from the detection limit calculation (Barnard's star: 36.1-36.4 d and 44.6 – 45.1 d; Proxima Cen: 295.0–313.11 d and 347.1-392.5 d). The HZ is depicted for each star derived from Fig. 15 of Kasting et al. (1993), whereas we used the stellar masses from Table 3.2. For an M dwarf with a mass of $0.3 M_{\odot}$, the HZ is beyond 0.1 AU. For several stars we can exclude planets with a few ten Earth masses in their HZ and Jupiter-mass planets ($1 M_{\rm Jup} = 318 M_{\rm Earth}$) up to a few AU.

3.3.5 Correlation between RV and Hα index?

Stellar activity can affect the measured RV. The Hα line is an indicator of stellar activity (the only available one in the UVES spectra). In Proxima Cen as an active flare star, the Hα line is in emission in contrast to low-activity Barnard's star. However, the Hα line is variable in both cases. Therefore investigating the correlation between RV and variations in the Hα line may be useful for correcting RV for stellar activity.

Kürster et al. (2003) report a correlation of this type for Barnard's star. We checked this again with the now available longer data set for Barnard's star, as well as for the other stars. As a measure of the variability of the Hα line we adopt the definition of the Hα-index by Kürster et al. (2003):

$$I = \frac{\overline{F_0}}{0.5(\overline{F_1} + \overline{F_2})} \tag{3.3}$$

where $\overline{F_0}$ is the mean flux in the range of [-15.5km/s,+15.5km/s] around the Hα line ($\lambda = 656.28$ nm) and $\overline{F_1}$ and $\overline{F_2}$ are the mean flux two reference bandpasses ([-700km/s,-300km/s] and [600 km/s, 1000 km/s], respectively) used for normalization. This index is a kind of filling-in of the Hα line (i.e for emission $I \gtrsim 1$) and is related to equivalent width (see Appendix 3.6.1). Following Kürster et al. (2003), we also computed a CaI index [+441.5 km/s, 472.5 km/s] for comparison. The CaI line ($\lambda = 6572.795$ Å) is expected to be stable.

Figure 3.7 shows the variation in the Hα index for Barnard's star with time. In Fig. 3.8 the RV is plotted against the Hα index. The flare event has already been described in Kürster et al. (2003), does not seem to have any effect on the RV, and is excluded from the correlation analysis. No further flare was detected in the longer data set. We calculated a correlation coefficient of $r = -0.42$ for the whole data set. Because the new data (JD>2452600) have a less pronounced anti-correlation with a correlation coefficient of $r = -0.25$, the correlation decreases compared to the old data set where $r = -0.50$ (Kürster et al., 2003), but the anti-correlation is still present and becomes more significant due to the longer baseline.

We performed a period search (Fig. 3.4, top panel) for the Hα index of Barnard's star (again flare event is excluded). With the new data, a 1000 d period dominates the GLS periodogram (upper panel). There is also some power at 44.5 d that was found to be the dominant period in the RV data (second panel). Therefore it is probable that the 45-day RV period is caused by stellar activity rather than by a planet (third panel). When we subtract the correlation from the RV data, the rms reduces slightly from 3.35 m/s to 3.09 m/s. The FAP of this period for the corrected RV data is only 5.5% compared to $< 0.01\%$ of the uncorrected RV data (Table 3.6). A similar analysis for the other stars[6] only yields a significant correlation for GJ 433, GJ 821, and GJ 855 (Figs. 3.9–3.11). All stars show no significant RV-CaI index correlation.

Finally, we investigated the question of whether more active stars show more RV excess scatter. Figure 3.12 compares the RV scatter (rms from Table 3.4) and the relative Hα line index scatter for all M dwarfs from our sample and demonstrates that no correlation can be seen.

[6]The 6 six stars with companions were excluded.

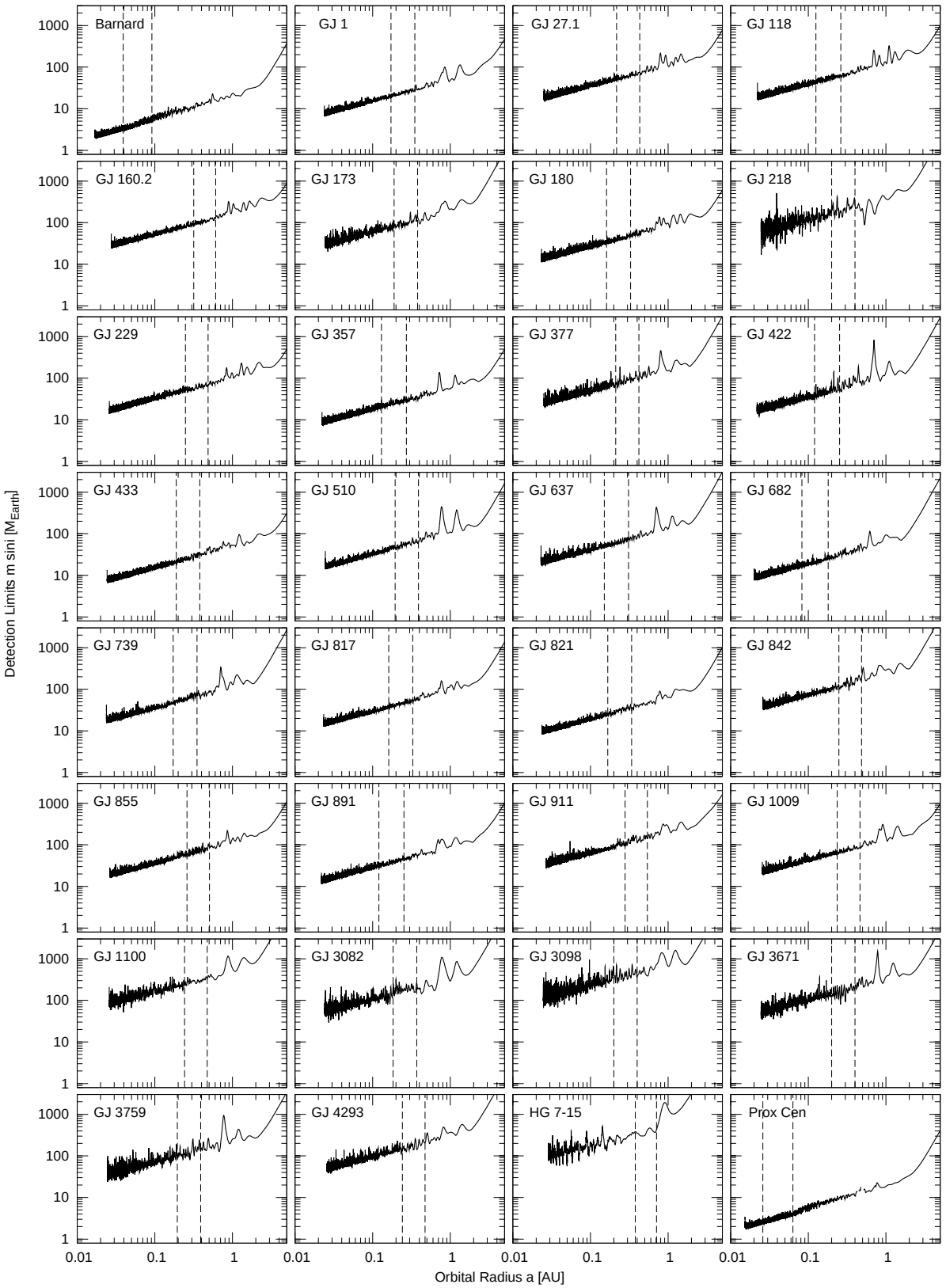

Figure 3.6: Detection limits for stars with at least 8 RV measurements. Planets in circular orbits above the limit would be detected with a probability >99%. The dashed lines show the habitable zone (HZ) (Kasting et al., 1993).

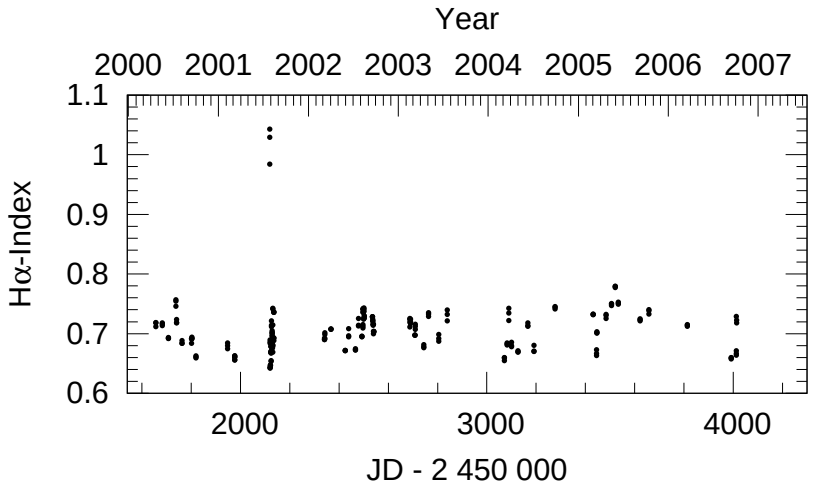

Figure 3.7: Time series of the Hα-index for Barnard's star.

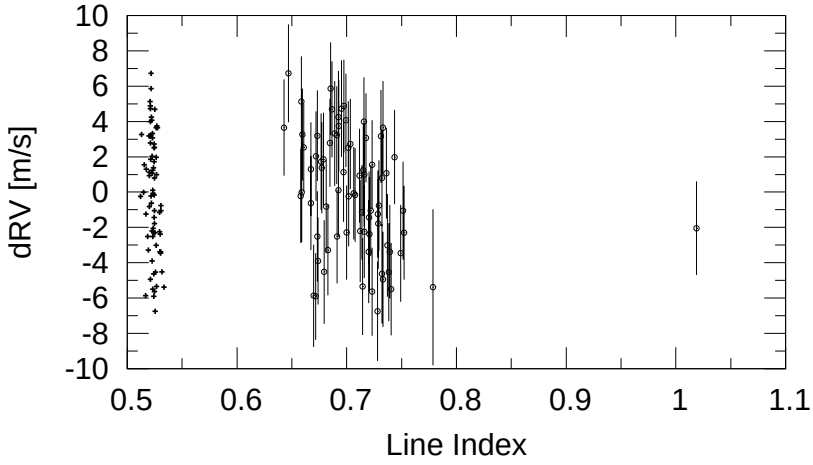

Figure 3.8: Correlation of the Hα-index with the RV for Barnard's star (dots with error bars, $r_{\mathrm{H}\alpha} = 0.42$). For comparison the CaI-index (crosses).

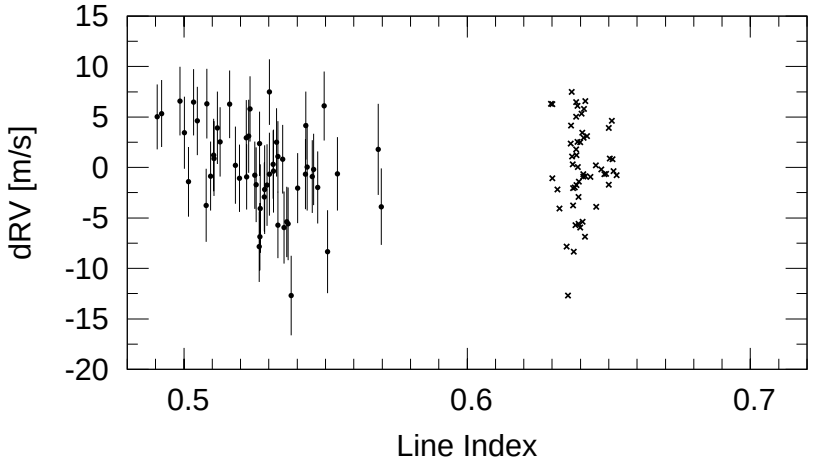

Figure 3.9: Correlation of the Hα- and CaI-index with the RV for GJ 433 ($r_{\mathrm{H}\alpha} = -0.40$).

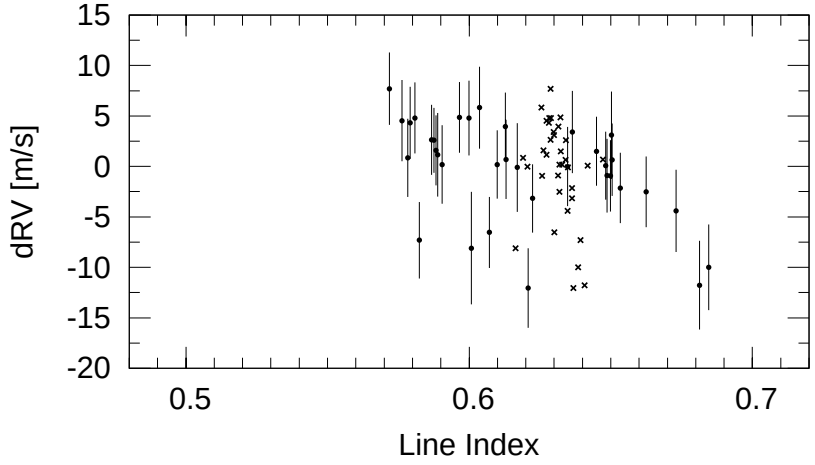

Figure 3.10: Correlation of the Hα- and CaI-index with the RV for GJ 821 ($r_{\mathrm{H}\alpha} = -0.49$).

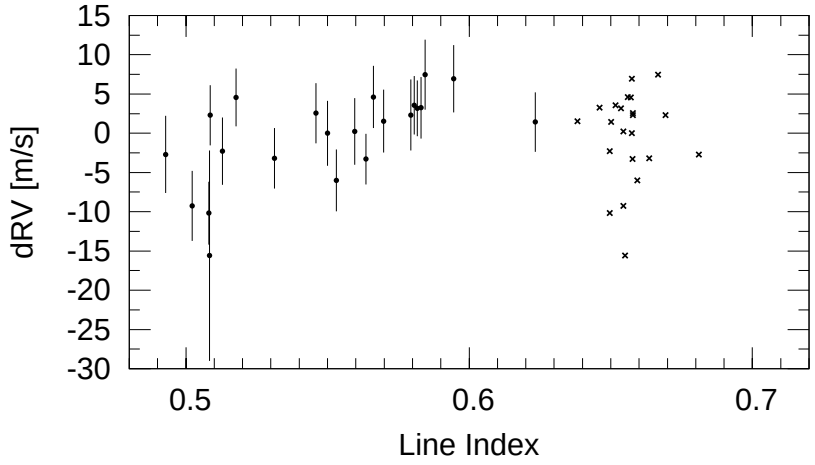

Figure 3.11: Correlation of the Hα- and CaI-index with the RV for GJ 855 ($r_{\mathrm{H}\alpha} = 0.62$).

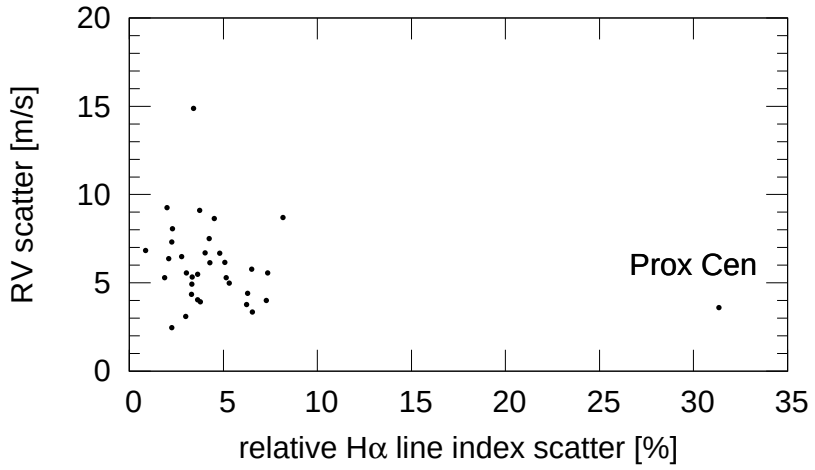

Figure 3.12: Comparison of the RV scatter (rms) and Hα variability for all M dwarfs with an rms $<$ 20 m/s. No correlation can be seen. The very active star Proxima Cen shows only very low RV excess.

3.4 Discussion

We browsed the available literature and catalogues for known binarity of our M dwarfs, which may have an impact on planet formation. Well known are the substellar companions to GJ 229 (Nakajima et al., 1995) and GJ 263 (Beuzit et al., 2004). Proxima Cen constitutes a widely separated common proper motion pair with α Cen A+B.

For GJ 477 and GJ 3916, binarity is indicated in the Hipparcos catalogue. GJ 477 has the double/multiple systems flag "X" (stochastic solution, probable astrometric binaries with a short period). GJ 3916 is listed with the flag "G" (acceleration or higher order terms). The large amplitudes seen in the RVs for both stars confirm this.

Other stars with an entry are: GJ 620 ("G"), GJ 4106 ("G"), and GJ 433 ("O", i.e. orbital solution). For these stars we found only low RV variation. This is at least controversial for GJ 433 (HIP 56528). The announced period is 500 d (see also Bernstein, 1997) and the amplitude is expected to be several hundred m/s.[7] At 1 AU our detections limit reaches down to $0.2 M_{\rm Jup}$ (Fig. 3.6).

To our knowledge the rest of our sample so far has no discovered companions. Companions are explicitly excluded with near-infrared speckle interferometry by Leinert et al. (1997) for GJ 1 and GJ 682 ($\Delta K = -4.5$ mag at 1-10 AU), as well as GJ 891 with infrared coronagraphic imaging by McCarthy & Zuckerman (2004) (>$30 M_{\rm Jup}$ at 140-1200AU).

Kürster et al. (2003) discussed how several stellar activity phenomena, such as spots, plages, or convective RV shifts, might affect the RV measurements. A linear RV-Hα anti-correlation that is present in Barnard's star could be a result of a convective redshift caused by plages that suppress blueshifted convective flows. We find such an anticorrelation for GJ 433 and GJ 821, while GJ 855 exhibits a positive correlation (Figs. 3.9–3.11). Bonfils et al. (2007) presented with GJ 674 (M2.5V) an example where the RV and Hα variations seem to be phase-shifted. The correlation thus differs from a linear one and looks like a loop. One would expect such behaviour for a plage rotating with the surface.

Flare events, such as the one observed in Barnard's star, do not seem to take part in the correlation. This agrees with the fact that no significant and strong correlation is observed in the flaring M dwarf Proxima Cen (see also Endl & Kürster, 2008).

3.5 Conclusion

Within the sensitivity provided by our RV precision of a few m/s we have not detected any planets around our sample stars. Most of the M dwarfs exhibit only low RV variations and some of them have a measurable secular acceleration due to their high proper motion.

We have discussed two effects on the RV that are not caused by planetary companions. First, the secular acceleration, is a perspective effect and causes always a positive RV trend. This effect can be corrected easily. Vise versa, this can be seen as an independent measurement of the astrometric quantity $\frac{\mu^2}{\pi}$, i.e. a confirmation for the ratio of squared proper motion and parallax (the absolute RV is not required). The second effect are RV variations caused by stellar activity. This is likely the case for the 45 d period we found in the RV data of Barnard's star. The RVs correlate with the Hα index. Such a correlation was found here only for a few M dwarfs and therefore no conclusions can be drawn in general.

As a by-product of our survey we have identified 6 M dwarfs with low-mass companions, four of them (GJ 477, GJ 1046 and GJ 3020, and GJ 3916) are brown dwarf or low-mass stellar candidates and two are spectroscopic binaries (SB2: GJ 263 and GJ 190). Follow-up RV observations will yield the orbital parameters and the lower limits for the companion masses $m \sin i$.

Our detection limits demonstrate that we can exclude giant planets with $1 M_{\rm Jup}$ up to 1 AU for half of our M dwarfs and that we are in principle capable of discovering planets with a few Earth masses in the

[7] The parameters for the circular orbit ($e = 0$, $\omega = 0$) are $P = 500 \pm 32$ d, $T_0 = 2448402 \pm 28$ d, $a_0 = 4.27 \pm 2.04$ mas, $i = 54 \pm 2$, and $\Omega = 346 \pm 22$ deg. With the parallax $\pi = 112.58 \pm 1.44$ the semi major axis of the photocentre is $a_0 = 0.0379$ AU. Assuming $a_0 \approx a_1$ the amplitude would be $K_1 = \sin i \frac{2\pi a_0}{P} = 668$ m/s for the circular orbit. With $m_1 = 0.48 M_\odot$ the secondary mass is $m_2 = 19.8 M_{\rm Jup}$ calculated from the mass function $f(m) = \frac{(m \sin i)^3}{(m+M)^2} = \frac{P}{2\pi G}(K\sqrt{1-e^2})^3$, i.e. $m \sin i = K \cdot \sqrt[3]{(m+M)^2 \frac{P}{2\pi G}}$.

habitable zones of M dwarfs with VLT+UVES. For this purpose an adequate number of measurements is needed to find low amplitudes of the order of the achieved high RV precision. The low frequency of Jupiter-mass planets around M dwarfs requires a large sample. The given detection limits are based on the search for single planets in circular orbits. These limits would be higher for eccentric orbits or multi-planet systems.

Even if planet detections are more spectacular, it is also important to report non-detections, which are required to estimate the planet frequency. Our non-detections of planets support the increasing observational evidence of a lower frequency of Jupiter-mass planets around M dwarfs. Endl et al. (2006) estimated a frequency of $\approx 1\%$ or less up to 1 AU orbital radius for Jupiter-mass planets around M dwarfs compared to 2.5% for solar like stars. This comparison cannot be done yet for low-mass planets because they are much harder to detect (and even more so for G stars), which introduces observational biases. However low-mass planets seem to be quite frequent around M dwarfs (Bonfils et al., 2007).

Expansion of current M dwarf planet searches will allow more precise determination of the true frequency of giant planetary companions to this type of stars and lower the detection limits. Photometric surveys for transits like the recently started project MEarth (Irwin et al., 2009) monitoring 2000 nearby M dwarfs and microlensing projects will also contribute. The discoveries of planetary systems around GJ 876 (Delfosse et al., 1998; Marcy et al., 1998, 2001; Rivera et al., 2005) and GJ 581 (Udry et al., 2007) show that planets do exist around M dwarfs. This promises further discoveries of low-mass planets in the future with high-precision RV surveys.

3.6 Accompanying auxiliary calculations

3.6.1 Relation between index and equivalent width

The equivalent width is defined as

$$EW = \sum_i \delta\lambda_i \frac{F_{C_i} - F_i}{F_{C_i}}$$

where $\delta\lambda_i$ is the width of the i-th pixel in wavelength, and F_i and F_{C_i} are the flux and continuum flux in the i-th pixel, respectively. The equivalent width EW is measured in terms of wavelengths. In a normalized spectrum the continuum flux is constant $F_{C_i} = F_C$ resulting in

$$EW = \Delta\lambda \left[1 - \frac{1}{\Delta\lambda} \sum \delta\lambda_i \frac{F_i}{F_C}\right]$$

where $\Delta\lambda = \sum \delta\lambda_i$ is the considered wavelength range.

The index I as defined (for Hα) in Eq. (3.3) is, on the other hand, a dimensionless measure. It is normalized by the mean flux $\overline{F} = \frac{1}{\Delta\lambda}\sum_i \delta\lambda_i F_i$ taken from reference ranges instead of the continuum, which is sometimes difficult to estimate, in particular for M dwarfs with their ubiquitous absorption lines.

In the case that the reference regions are estimated as continuum, i.e. $\overline{F_1} = \overline{F_2} = F_C$, the index becomes $I = \frac{1}{F_C}\frac{1}{\Delta\lambda}\sum_i \delta\lambda_i F_i$ and is related to EW as

$$I = 1 - \frac{EW}{\Delta\lambda}.$$

Note that an absorption line is indicated by $EW > 0$ ($0 < I < 1$) and an emission line by $EW < 0$ ($I > 1$).

3.6.2 Response of the GLS periodogram when adding a sine wave

The definition of the generalized Lomb-Scargle periodogram (GLS) is (we use the notation introduced in Zechmeister & Kürster 2009)

$$p_y(\omega) = \frac{1}{YY} \cdot \frac{SS \cdot YC^2 + CC \cdot YS^2 - 2CS \cdot YC \cdot YS}{CC \cdot SS - CS^2}$$

whereas abbreviations are weighted covariances for data y_i, sine, and cosine terms (e.g. $YC = \sum w_i y_i \cos \omega t_i - \sum w_i y_i \cdot \sum w_i \cos \omega t_i = \sum w_i (y_i - \bar{y}) \cos \omega t_i$; w_i are normalised weights).

When introducing a parameter τ defined by $\tan 2\tau = \frac{2CS}{CC-SS}$ and replacing t_i by $\tau_i = t_i - \tau$ (resulting in $CS_\tau = 0$) the GLS can be written as (see Zechmeister & Kürster (2009) for details)

$$p_y(\omega) = \frac{1}{YY}\left[\frac{YC_\tau^2}{CC_\tau} + \frac{YS_\tau^2}{SS_\tau}\right]$$

in a form very similar to classical Lomb-Scargle periodogram. While the first formulation can save some computational effort, the use of the second is more elegant for our purpose.

By adding a sine wave with frequency ω_0 to the data y_i, we generate new data $x_i = y_i + a\cos\omega_0 t_i + b\sin\omega_0 t_i$ or $x_i = y_i + a_\tau \cos\omega_0 \tau_i + b_\tau \sin\omega_0 \tau_i$. This results in a new periodogram $p_x(\omega)$ for the new data set x

$$p_x(\omega) = \frac{1}{XX}\left[\frac{XC_\tau^2}{CC_\tau} + \frac{XS_\tau^2}{SS_\tau}\right].$$

Because the times are not changed, this neither affects the parameter τ or the sums that only depend on the time sampling (CC_τ and SS_τ or CC, SS, CS, and D, respectively). When adding the sine wave the mean changes

$$\begin{aligned}\bar{x} &= \sum w_i x_i = \sum w_i y_i + a\sum w_i \cos\omega_0 t_i + b\sum w_i \sin\omega_0 t_i \\ &= \bar{y} + aC_0 + bS_0.\end{aligned}$$

The sums YC and YS change as follows

$$\begin{aligned}XC &= \sum w_i (x_i - \bar{x}) \cos\omega t_i = YC + aCC_0 + bCS_0 \\ XS &= \sum w_i (x_i - \bar{x}) \sin\omega t_i = YS + aC_0 S + bSS_0 \\ XX &= \sum w_i (x_i - \bar{x})^2 \\ &= \sum w_i (y_i - \bar{y} + a(\cos\omega_0 t_i - C_0) + b(\sin\omega_0 t_i - S_0))^2 \\ &= YY + a^2 C_0 C_0 + b^2 S_0 S_0 + 2aYC_0 + 2bY_0 S_0 + 2abC_0 S_0. \end{aligned} \tag{3.4}$$

As described in Sect. 3.3.4, it is more conservative to scan the power only at $\omega = \omega_0$ instead of the whole frequency range. This bypasses the calculation of sums comprising two different frequencies and is an enormous simplification. The sums of simulated data can be expressed by the sums for the original data. Therefore is not necessary to repeat the summation for the simulated data. When using the notation with τ this becomes $XC_\tau = YC_\tau + a_\tau CC_\tau$ and $XS_\tau = YS_\tau + a_\tau SS_\tau$ because $CS_\tau = 0$.

The power response at the frequency where the sine wave was added is

$$\begin{aligned}p_x(\omega) &= \frac{1}{XX}\left[\frac{YC_\tau^2}{CC_\tau} + a^2 CC_\tau + 2aYC_\tau + \frac{YS_\tau^2}{SS_\tau} + b^2 SS_\tau + 2bYS_\tau\right] \\ &= \frac{1}{XX}\left[p_y YY + XX - YY\right] = 1 - \frac{(1-p_y)YY}{XX}.\end{aligned}$$

Now we are interested in the amplitude A or variance XX that is required for a given phase φ to produce a desired power threshold $p_x(\omega)$, which corresponds to an FAP. The required variance is $XX = YY\frac{1-p_y}{1-p_x}$.

We obtain the required amplitude by solving the quadratic equation resulting from Eq. (3.4) ($a = A\cos\varphi$, $b = A\sin\varphi$)

$$\begin{aligned}0 &= a^2 CC + b^2 SS + 2aYC + 2bYS + 2abCS - (XX - YY) \\ &= A^2(CC\cos^2\varphi + SS\sin^2\varphi + 2CS\cos\varphi\sin\varphi) \\ &\quad + 2A(YC\cos\varphi + YS\sin\varphi) - (XX - YY) \\ &= \alpha A^2 + 2\beta A - \gamma\end{aligned}$$

with the substitutions $\alpha = CC\cos^2\varphi + SS\sin^2\varphi + 2CS\cos\varphi\sin\varphi$, $\beta = YC\cos\varphi + YS\sin\varphi$, and $\gamma = XX - YY = YY\frac{p_x - p_y}{p_x}$. This leads us to the amplitude

$$A(\omega,\varphi) = -\frac{\beta}{\alpha} \underset{(-)}{+} \sqrt{\left(\frac{\beta}{\alpha}\right)^2 + 4\frac{\gamma}{\alpha}},$$

which we consider as the amplitude detection limit for a fixed phase and for a given power threshold p_x and which can be expressed by GLS sums for the original data. Probing a set of phases φ, we finally choose $\max_\varphi A(\omega,\varphi)$.

The second of the two solution is rejected, because we demand positive amplitudes ($A > 0$, $\varphi \in [0, 360^\circ)$). The terms α and γ are always positive: $\gamma = YY\frac{p_x - p_y}{p_x} > 0$ (as long as $p_x - p_y > 0$) and $\alpha = CC\cos^2\varphi + SS\sin^2\varphi + 2CS\cos\varphi\sin\varphi = CC_\tau\cos^2\varphi + SS_\tau\sin^2\varphi > 0$.

3.7 Additional note regarding the planet discovery for GJ 433

On an ESO workshop (Towards Other Earths, Porto, Portugal) in October 2009, i.e. after our publication (Zechmeister et al., 2009), there was a planet announcement for the M dwarf GJ 433 based on HARPS RV measurements. Today, even one year later, there is no refereed publication of this announcement. The only information publicly available[8] for the putative planet is a period of $\sim$7 d and a minimum mass of $0.019\,M_{\rm Jup}$ ($6\,M_\oplus$) which corresponds to an RV semi-amplitude of ~ 3 m/s.

Here we would like to re-analayse our UVES data and discuss that supposed planet detection. Our best-fitting sinusoid has a period of 6.5 d that is listed in Table 3.6 having an amplitude of 3.3 m/s (corresponding to $6\,M_\oplus$). These values are quite similar to the announced ones. However, this period is not statistically significant in our data set and we cannot claim a planet. Figure 3.13 shows the periodogram including a zoom-in to the region of interest. Figure 3.14 shows the RV data phased to this period. The fit reduces the the scatter from 4.3 m/s to 3.6 m/s.

[8] `http://exoplanet.eu/planet.php?p1=GJ+433&p2=b`

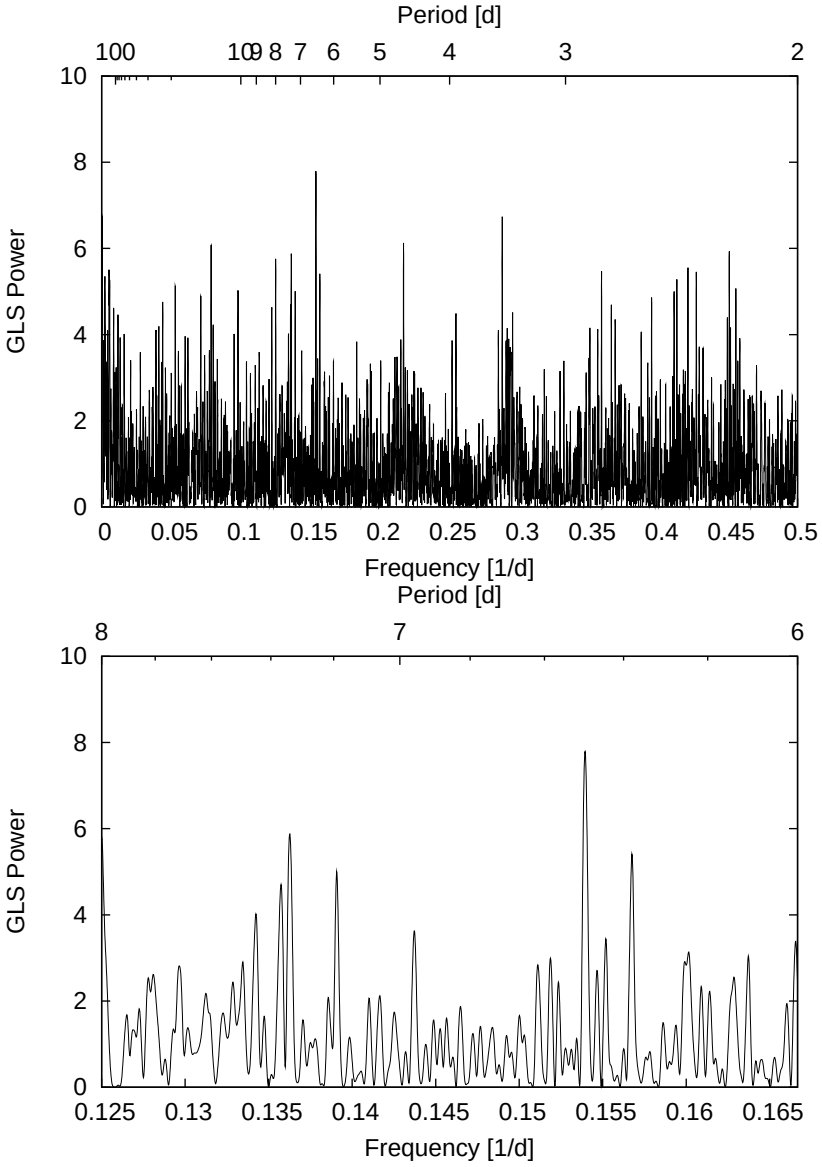

Figure 3.13: Periodogram for GJ 433 for periods down to 2 d (top) and zoom in to the range 6–8 d (bottom).

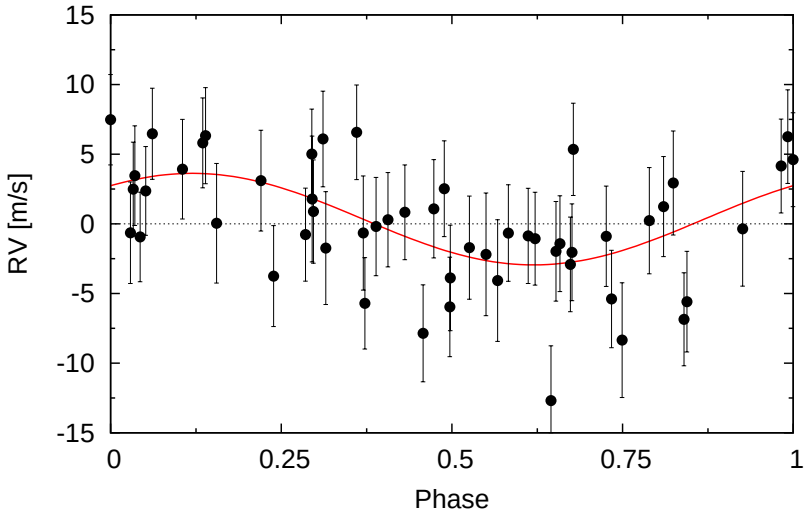

Figure 3.14: RVs for GJ 433 phase folded to the best-fitting, but non-significant period of 6.5 d.

We stress that periods other than that at 6.5 d have even less power. We also point out that our RVs correlate with variations in the Hα-line strength (see Sect. 3.3.5). We conclude that the HARPS data set must have much better RVs precision, since otherwise we would be able to disprove the planet detection. We have to combine both UVES and HARPS data to clarify this.

Chapter 4

The planet search programme at the ESO CES and HARPS[1,2]

The search for Jupiter analogues around solar-like stars

Based on Zechmeister, Kürster, Endl, Lo Curto, Hartman, & Henning, close to submission to A&A

ABSTRACT: In 1992 we began a precision radial velocity survey for planets around solar-like stars with the Coudé Echelle Spectrograph and the Long Camera (CES LC) at La Silla (Chile) resulting in the discovery of the planet ι Hor b. We have continued the survey with the upgraded CES Very Long Camera (VLC) and the HARPS spectrographs. In this paper we present further radial velocities for 31 stars of the original sample with higher precision. The observations cover a time span of up to 15 years and permit a search for Jupiter analogues. The survey was carried out with three different instruments/instrument configurations using the iodine cell and the ThAr methods for wavelength calibration. We combine the data sets, perform a joint analysis for variability, trends, periodicities, and Keplerian orbits, and compute detection limits. We achieve a long-term RV precision of 15 m/s (CES+LC), 9 m/s (CES+VLC), and 3 m/s (HARPS), respectively. This enables us to confirm the planetary signals seen for ι Hor, HR 506, and HR 3259, while the planet ε Eri b cannot be confirmed. We find a steady RV trend for ε Ind A explicable by a planetary companion and calling for direct imaging campaigns. Contrariwise, we find previously reported trends to be smaller for β Hyi and not present for α Men. Long-terms in several of our stars are compatible with known stellar companions. We provide a spectroscopic orbital solution for the binary HR 2400 and refined solutions for the planets around HR 506 and ι Hor. The occurence of two Jupiter-mass planets in our sample is in line with the estimate of 10% for the frequency of giant planets with periods smaller than 10 yr around solar-like stars.

4.1 Introduction

The search for extra-solar planets has so far revealed more than 500 planets, most of them discovered by the radial velocity (RV) technique. Interestingly, many hot Jupiters have been found, a consequence related to the fact that the RV method as well as the transit method is very sensitive to short period

[1]Based on observations collected at the European Southern Observatory, La Silla Chile, ESO programmes 50.7-0095, 51.7-0054, 52.7-0002, 53.7-0064, 54.E-0424, 55.E-0361, 56.E-0490, 57.E-0142, 58.E-0134, 59.E-0597, 60.E-0386, 61.E-0589, 62.L-0490, 64.L-0568, 66.C-0482, 67.C-0296, 69.C-0723, 70.C-0047, 71.C-0599, 072.C-0513, 073.C-0784, 074.C-0012, 076.C-0878, 077.C-0530, 078.C-0833, 079.C-0681.

[2]Radial velocity data are available in electronic form at the CDS via anonymous ftp to cdsarc.u-strasbg.fr (130.79.128.5) or via http://cdsweb.u-strasbg.fr/cgi-bin/qcat?J/A+A/

planets. Out of 500 planets discovered so far, 61% have a period shorter than 1 year. Before the discovery of the first extrasolar planet around a solar-like star, the hot Jupiter 51 Peg b (Mayor & Queloz, 1995), it was widely expected that planetary systems are in general similar to the solar-system and this was also predicted by most theoretical models (Marcy et al., 2008). Therefore surveys were designed to search for planets with masses of $1\,M_{\rm Jup}$ and at distances of 5 AU from solar-like stars (e.g. Walker et al., 1995). The regime of Jupiter analogues is still sparsely explored, because observations with long time-baselines and precise RV measurements are required; e.g. Jupiter orbits the Sun in 12 years and induces an RV semi-amplitude of 12 m/s.

The survey described in this paper was begun in 1992 (Endl et al., 2002) with the Coudé Echelle Spectrograph (CES) Long Camera (LC). It was continued in 1999 with the CES Very Long Camera (VLC) and later on in 2003 with the HARPS spectrograph. The survey covers a time span of up to 15 years with RV precisions ranging from 15 m/s down to 3 m/s. A comparable survey was analysed by Wittenmyer et al. (2006) and carried out in the northern hemisphere with the 2.7m telescope at the McDonald Observatory. It started in 1988 with 24 solar-like stars[3] and 7 subgiants and was combined with CFHT data (Walker et al., 1995), giving it an even longer temporal coverage up to 25 years, albeit with a somewhat lower precision (10–20m/s).

There are many other exoplanet search projects at Lick, AAT (O'Toole et al., 2009a), Keck (Cumming et al., 2008), Elodie/Sophie (Naef et al., 2005), Coralie (Ségransan et al., 2010), and HARPS (Naef et al., 2010). These high precision RV projects have discovered a large fraction of the currently known planets and are continuously extending their time baselines. Examples for discovered Jupiter analogues are GJ 777Ab (Naef et al., 2003), a $1.33\,M_{\rm Jup}$ planet at 4.8 AU around a G6IV star, or HD 154345b (Wright et al., 2008), a $0.95\,M_{\rm Jup}$ planet at 4.5 AU around a G8V dwarf.

4.2 The sample

The original sample of 37 solar-like stars was introduced in detail in Endl et al. (2002). Of these, the monitoring of six stars was stopped: HR 448, HR 753, HR 7373, Barnard's star, Proxima Centauri, and GJ 433. The latter three are M dwarfs. For these recent and more precise results with VLT+UVES are published in Zechmeister et al. (2009). We are left with 31 stars listed in Table 4.1 along with some of their properties (spectral type, visual magnitude, distance, and stellar mass).

All stars have a brightness of $V < 6$ mag and spectral types ranging from late F to K. There are two subgiant stars (β Hyi, and δ Eri) and two giant stars (HR 3677 and HR 8883) in the sample[4]. In the following we provide some short notes on selected individuals objects.

β Hyi and τ Cet: These stars were the subjects of asteroseismology campaigns (Bedding et al., 2007; Teixeira et al., 2009) which provided stellar parameters and also an insight for the magnitude of the nightly, oscillation-induced RV jitter ($\sim$2 m/s, cf. Table 4.10).

HR 506 (HD 10647): A planet candidate was presented by Mayor et al.[5] based on CORALIE measurements presented at the XIX th IAP Colloquium (Paris, 2003). Jones et al. (2004) found also weak evidence for a similar signal with the AAT, but did not exclude stellar activity as the cause. Butler et al. (2006) listed AAT RV data and derived orbital parameters.

ι Hor: For this active star Kürster et al. (2000) discovered a planet. The signal was also seen by Naef et al. (2001) using the CORALIE spectrograph and by Butler et al. (2001) with the AAT. Vauclair et al. (2008) investigated the oscillations of this star with HARPS.

[3] There are three targets (δ Eri, α For, and τ Cet) common to both samples.

[4] HR 3677 and HR 8883 were indicated in the Bright Star Catalogue as dwarf stars (Hoffleit & Jaschek, 1991). Therefore they entered our sample, however they are giants as indicated by their distances.

[5] We found no refereed publication. Information is available on `http://obswww.unige.ch/~udry/planet/hd10647.html`.

Table 4.1: Targets with their spectral type (Hoffleit & Jaschek, 1991), visual magnitude V (Perryman et al., 1997), distance d (van Leeuwen, 2007), and stellar mass M.

Star	alias	Spec Type	V [mag]	d [pc]	M [$M_\odot$]	
HR 77	ζ Tuc	F9V	4.23	8.59	1.06	[PM]
HR 98	β Hyi	G2IV	2.82	7.46	1.1	[D]
HR 209	HR 209	G1V	5.80	15.16	1.10	[G]
HR 370	ν Phe	F8V	4.97	15.11	1.20	[G]
HR 506	HR 506	F9V	5.52	17.43	1.17	[G]
HR 509	τ Cet	G8V	3.49	3.65	0.78	[T]
HR 695	κ For	G0V	5.19	21.96	1.12	[G]
HR 810	ι Hor	G0V	5.40	17.17	1.25	[V]
HR 963	α For	F8V	3.80	14.24	1.20	[G]
HR 1006	ζ^1 Ret	G2.5V	5.53	12.01	1.05	[G]
HR 1010	ζ^2 Ret	G1V	5.24	12.03	1.10	[G]
HR 1084	ε Eri	K2V	3.72	3.22	0.85	[DS]
HR 1136	δ Eri	K0IV	3.52	9.04	1.23	[PM]
HR 2261	α Men	G6V	5.08	10.20	0.95	[G]
HR 2400	HR 2400	F8V	5.58	36.91	1.20	[G]
HR 2667	HR 2667	G3V	5.56	16.52	1.04	[G]
HR 3259	HR 3259	G7.5V	5.95	12.49	0.90	[G]
HR 3677	HR 3677	G0III	5.85	196.85	2.1	[G]
HR 4523	HR 4523	G3V	4.89	9.22	1.04	[G]
HR 4979	HR 4979	G3V	4.85	20.67	1.04	[G]
HR 5459	α Cen A	G2V	-0.01	1.25	1.10	[P]
HR 5460	α Cen B	K1V	1.35	1.32	0.93	[P]
HR 5568	GJ 570 A	K4V	5.72	5.84	0.71	[G]
HR 6416	HR 6416	G8V	5.47	8.80	0.89	[G]
HR 6998	HR 6998	G4V	5.85	13.08	1.00	[G]
HR 7703	HR 7703	K3V	5.32	6.02	0.74	[G]
HR 7875	ϕ^2 Pav	F8V	5.11	24.66	1.1	[PM]
HR 8323	HR 8323	G0V	5.57	15.99	1.12	[G]
HR 8387	ε Ind A	K4.5V	4.69	3.62	0.70	[G]
HR 8501	HR 8501	G3V	5.36	13.79	1.04	[G]
HR 8883	HR 8883	G4III	5.65	101.32	2.1	[G]

References for mass estimates: [D] Dravins et al. (1998), [DS] Drake & Smith (1993), [G] Gray (1988), [PM] Porto de Mello, priv. comm., [P] Pourbaix et al. (2002), [T] Teixeira et al. (2009), [V] Vauclair et al. (2008).

ε Eri: Hatzes et al. (2000) announced a planet around this active star. Benedict et al. (2006) refined the orbital solution and combined the RVs with astrometric measurements indicating an orbital inclination of $i = 30°$.

α Men: Eggenberger et al. (2007) reported a companion for α Men which is likely an M3.5 – M6.5 dwarf that was seen at a separation of 3.05" with the VLT+NACO. They also mentioned a radial velocity drift seen with the CORALIE spectrograph.

HR 3259: This star is known to host a planetary system with three Neptune-mass planets (Lovis et al., 2006).

Table 4.2: The three used instruments/configurations with their wavelength reference, chosen spectral coverage and resolving power, and telescope diameter.

Spectrograph	Ref.	λ [Å]	R	Tel.
CES + LC	I_2	5367 – 5412	100 000	1.4 m
CES + VLC	I_2	5376 – 5412	220 000	3.6 m
HARPS	ThAr	3800 – 6900	115 000	3.6 m

4.3 Instruments and data reduction

We used three high resolution spectrographs that are briefly described below with more detail provided for the less known VLC+CES. Table 4.2 gives an overview of some basic properties of the three instruments.

4.3.1 CES + Long Camera

In 1992 the survey started (1992-11-03 to 1998-04-04) with the Coudé Echelle Spectrograph (CES) and its Long Camera (LC) fed by the 1.4 m Coudé Auxiliary Telescope (CAT) at La Silla (Chile). The CES+LC had a chosen wavelength coverage of 45 Å and a resolution of 100 000 (Table 4.2). A 2 k CCD gathered part of one spectral echelle order. An iodine gas absorption cell provided the wavelength calibration. More details about the instrument, data analysis, as well as the obtained results can be found in Endl et al. (2002). Table 4.3 lists the radial velocity results. The median rms is 15.2 m/s when excluding the targets with comments in Table 4.3 and reflects the typical precision.

4.3.2 CES + Very Long Camera

The Very Long Camera (VLC) of the Coudé Echelle Spectrograph (CES) was operated since April 1998 together with the ESO 3.6 m telescope in La Silla (Chile). For our sample we collected VLC spectra from 1999-11-21 to 2006-05-24. The VLC was an upgrade of the CES that doubled the resolving power to $R = 220\,000 - 235\,000$ as well as the CCD length so that 80% of the spectral coverage was retained. This upgrade together with improved internal stability, and also the larger telescope aperture promised an improvement of the RV precision.

The VLC was fed by a fibre link from the Cassegrain focus of the 3.6 m telescope. A modified Bowen-Walraven image slicer provided an efficient light throughput at the high resolving power. It redistributed the light from the fibre with a $2''$ aperture via 14 slices to an effective slit width of $0.16''$ and resulted in a complex illumination profile in the spatial direction, i.e. perpendicular to the dispersion axis (Fig. 4.1). The right half of a 4 k $\times$ 2 k EEV CCD recorded part of one spectral order with the wavelength range of 5376 – 5412 Å. In 2006-06-15 CCD#59 was replaced by CCD#61.

The CES+VLC employed the same iodine cell as the CES+LC for wavelength calibration. This cell was controlled at a temperature of 50°C. The RV modelling (Sect. 4.3.4) requires a high resolution and high signal-to-noise iodine spectrum to reconstruct confidently the instrumental line profile (IP) of the spectrograph. In November 2008 we obtained for our iodine cell a spectrum with $R = 1\,000\,000$ and S/N$\sim$1000 performed with a Fourier Transform Spectrometer (FTS) at Lund Observatory. While the former iodine cell scan had only $R = 400\,000$, the new scan ensures a iodine spectrum with a resolution almost 5 times higher than the resolution of the VLC spectrograph.

The following properties of the CES+VLC spectra must be considered in the data analysis: The VLC spectra are contaminated by a grating ghost located in the middle of the CCD (Fig. 4.1) and suffered also from stray light produced by the image slicer. Ripples are visible in the continuum of high S/N ($\sim$1000) spectra such as flat fields, caused by interference in the fibre. Also visible in flats are less efficient rows on the chip every 512 pixels, due to a smaller pixel size resulting from the manufacturing process, which affect the wavelength solution. Moreover, a lower bias level is observed to the left of the spectra, probably

Table 4.3: Radial velocity results for all targets. For each instrument configuration the rms is calculated independently. RV data are not binned. Comments are on multiplicity (see also Table 4.6 for more information).

Star	CES + LC				CES + VLC				HARPS				Comment
	N	T [d]	rms [m/s]	$\overline{\Delta RV}$ [m/s]	N	T [d]	rms [m/s]	$\overline{\Delta RV}$ [m/s]	N	T [d]	rms [m/s]	$\overline{\Delta RV}$ [m/s]	
ζ Tuc	51	1888	19.8	14.5	48	2104	9.2	7.9	136	1415	3.4	0.5	
β Hyi	157	1887	22.9	18.6	46	1920	7.7	12.5	2432	1837	2.7	0.3	
HR 209	35	1572	17.2	17.6	36	1941	11.1	9.8	48	1401	8.9	0.4	
ν Phe	58	1926	15.6	14.6	35	1910	10.1	8.2	63	1415	3.0	0.5	
HR 506	23	1573	28.0	20.2	42	1910	18.7	17.7	57	1401	13.2	0.6	planet
τ Cet	116	1888	11.4	13.3	61	1920	8.1	8.8	4479	2041	4.0	0.3	
κ For	40	1890	722.9	12.8	45	2094	1134.0	10.2	74	1401	660.1	0.4	SB1
ι Hor	95	1976	51.3	16.9	122	2186	37.1	12.6	1838	1401	12.7	0.6	planet
α For	65	1889	42.2	31.6	39	1856	16.7	14.7	191	1401	8.4	0.5	trend
ζ^1 Ret	14	184	17.0	14.2	42	1857	15.3	10.3	63	1401	8.0	0.4	
ζ^2 Ret	58	1976	18.9	14.6	43	1857	10.1	9.3	51	1401	3.4	0.4	
ε Eri	66	1889	12.2	9.0	69	2186	10.0	8.1	508	1390	5.7	0.2	planet(?)
δ Eri	48	1888	12.5	11.7	42	1856	7.5	7.0	142	1443	2.5	0.2	
α Men	46	1852	9.8	10.7	77	2368	8.4	9.8	253	1297	3.7	0.2	
HR 2400	53	1924	275.1	23.0	54	2039	523.8	14.4	66	1296	235.1	0.5	SB1
HR 2667	66	1934	15.1	18.5	64	2329	7.5	11.4	72	1296	1.6	0.3	
HR 3259	35	1851	16.5	11.3	61	2367	9.2	7.7	64	1287	3.8	0.3	three planets
HR 3677	34	1924	492.4	15.1	38	2044	1253.9	8.2	69	1287	906.5	0.4	SB1
HR 4523	27	1925	14.9	12.2	57	2276	6.7	8.9	309	1608	9.8	0.2	
HR 4979	52	1933	11.7	10.8	58	2329	9.2	10.2	90	1510	3.3	0.2	
α Cen A	205	1852	166.5	10.7	1076	2276	97.7	10.2	4440	1273	39.8	0.2	SB1
α Cen B	291	1852	203.5	9.3	54	1770	247.6	7.7	887	1616	178.7	0.1	SB1
GJ 570 A	40	384	6.9	11.4	87	2284	10.2	6.5	53	1853	3.0	0.2	
HR 6416	57	1845	23.8	12.6	59	2278	23.4	9.4	73	1310	7.5	0.3	trend
HR 6998	51	1789	15.3	20.8	23	2062	9.6	9.8	68	1044	1.7	0.3	
HR 7703	30	1042	10.3	11.6	31	2039	7.6	8.0	70	1722	4.7	0.3	trend
ϕ^2 Pav	90	1969	32.1	25.6	200	2062	17.1	23.9	60	1401	4.0	0.7	
HR 8323	20	1067	14.4	14.6	31	2124	11.4	10.1	122	1547	2.4	0.5	
ε Ind A	73	1888	11.9	9.1	54	2124	7.1	7.9	325	1763	8.0	0.3	trend(?)
HR 8501	66	1889	36.8	24.7	45	2125	36.6	16.1	57	1401	14.0	0.4	trend
HR 8883	31	1258	63.1	31.3	30	2125	66.9	23.6	45	1401	60.5	0.8	giant

Listed are the number of observations N, the time baseline T, the weighted rms of the time series and the effective mean internal radial velocity error $\overline{\Delta RV}$.

caused by an electronic offset after a strong signal (P. Sinclair, priv. comm.). This effect seems also to affect subsequent lines which may cause RV shifts depending on the line depth, i.e the weaker iodine lines may not receive the same shift as the stronger stellar lines.

The spatial profile has a width spanning more than 400 pixels offering a large cross-section for cosmic ray hits. For this reason the observing strategy aimed at three consecutive spectra in one night to be able to identify cosmics as outliers. However, we did not use this cosmics detection method because cosmics could also be efficiently identified as deviations from the spatial profile in the optimum extraction.

The VLC spectra were reduced with standard IRAF-tasks including bias-subtraction, flat-fielding, scattered light subtraction and optimum extraction (Horne, 1986) which also removes cosmics. Finally, the science spectra were roughly calibrated with a wavelength solution from a nightly ThAr spectrum.

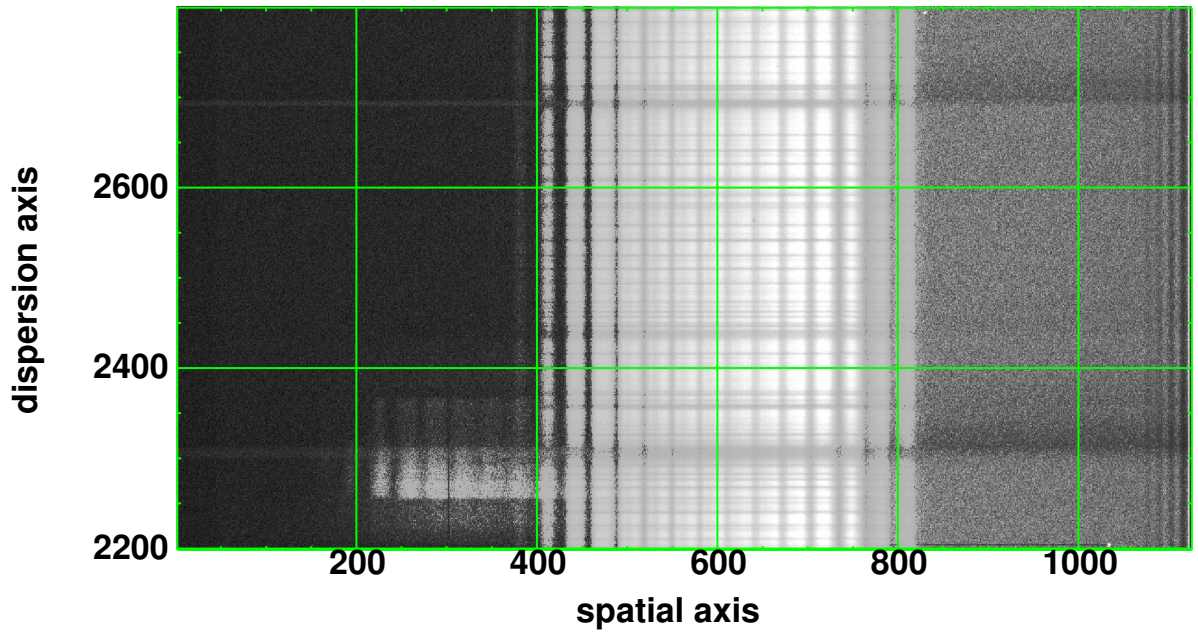

Figure 4.1: A small section of a VLC spectrum (star with iodine lines). The 14 slices span 400 pixels. The bright feature to the left near pixel row 2300 is a grating ghost. The area on the left side has a lower bias. The readout register is in the lower right corner of the chip (parallel clocking down, serial clocking to the right). Deeper stellar lines near row 2300 and 2700 have tails to the left and right.

The data reduction process largely removed the artefacts described above, however residual effects might explain systematic jumps observed in the RVs of the VLC data. The typical precision is 9.4 m/s calculated as the median rms in Table 4.3 for the stars without comments.

4.3.3 HARPS

With HARPS we monitored our targets from 2003-11-06 to 2007-09-21. The HARPS spectrograph is well described in the literature (e.g. Mayor et al., 2003; Pepe et al., 2004). It is fibre fed from the Cassegrain focus of the 3.6 m telescope and located in a pressure and temperature stabilised environment. An optical fibre sends light from a ThAr lamp to the Cassegrain adapter for wavelength calibration. For the RV computation 72 echelle orders ranging from 3800 Å to 6900 Å are available, a region much larger than for the CES.

We made use of the ESO advanced data products (ADP) to complement our time series. This archive provides fully reduced HARPS spectra including the final radial velocities processed by the pipeline DRS 3.0 (data reduction software). The radial velocities are drift corrected and the RV uncertainty estimated assuming photon noise[6]. The mean RV uncertainties range from 0.2 to 0.8 m/s. For data analysis a jitter term will be added in quadrature (see Sect. 4.4).

We recomputed some RVs, obtained from the archive that suffered from a misadjusted initial RV guess (off by 2 km/s) or from an inappropriate mask. A different mask, e.g. K5 instead of G2, can produce RV shifts up to 20 m/s. The additional data products are publicly available and originate from other (non-concurrent) programs as e.g. short-term asteroseismology campaigns. HARPS GTO (guaranteed time observations) were public at this time, but not in the ADP archive, and are not used here.

The HARPS data provide an absolute RV scale which is shown in Fig. 4.12–4.16 and can be transferred to the other instruments. The relative RVs are more precise than the absolute RVs (i.e. more precise than accurate). The median rms in Table 4.3 is 3.3 m/s.

[6]The pertinent information can be found in the *CCF_A.fits-file header (keywords RVC and DVRMS).

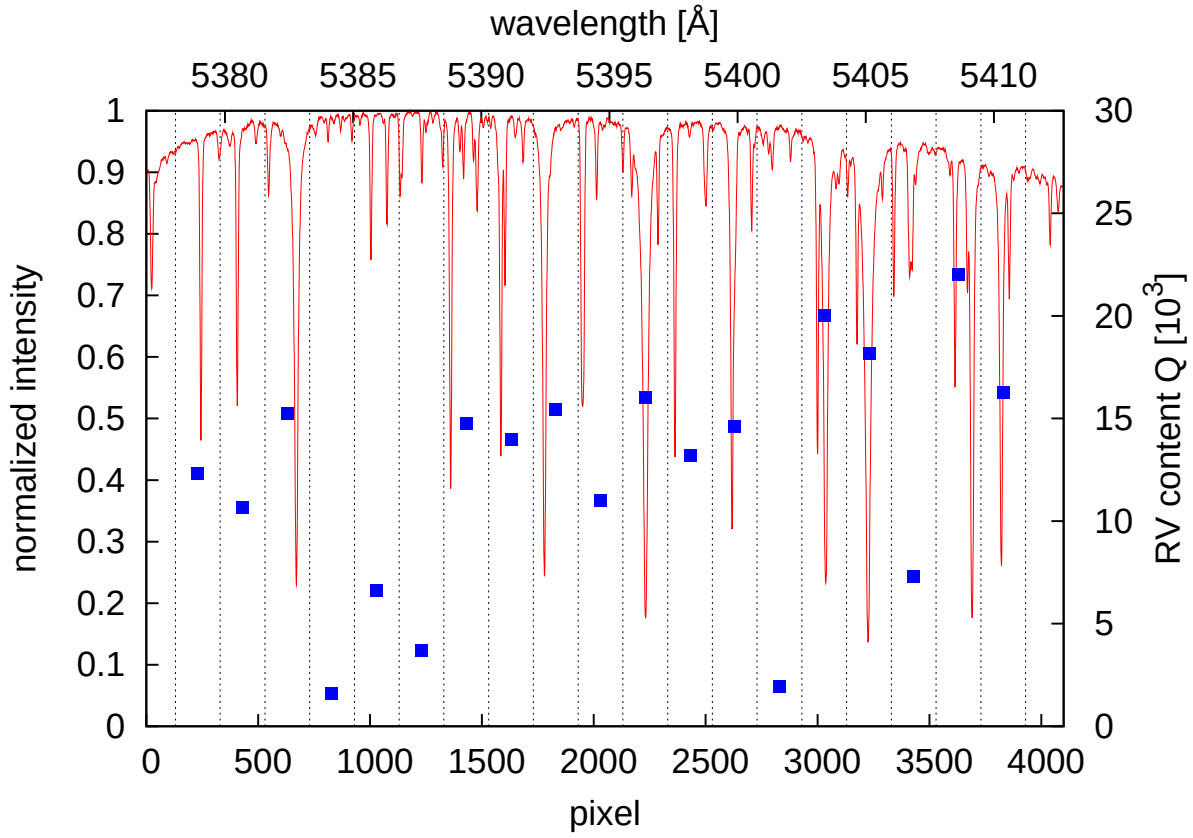

Figure 4.2: A VLC spectrum of τ Cet (without iodine cell) and the arrangement of the 200 pixel chunks with their individual Q-factors (blue squares). The intensity maximum of the spectrum is set to unity. The intensity declines to the edges due to instrumental effects (Blaze function).

To improve the combination of the HARPS and VLC data, spectra were taken in a few nights with both spectrographs immediately after each other making use of an easy switch possible with the common fibre adapter installed in May 2004.

4.3.4 Details of the RV computation for the CES+VLC data

To compute the RV of the VLC spectra we used the AUSTRAL code described in Endl et al. (2000) which is based on the modelling technique outlined in Butler et al. (1996). The spectral order was divided into 19 spectral segments (chunks) with a size of 200 pixels (1.8 Å) which we empirically found to yield optimal RV precision, probably because for a larger chunk size the assumption that the instrumental profile (IP) is constant over the chunk breaks down, while for smaller chunks the RV information content decreases. Figures 4.2 illustrates the alignment of the chunks with respect to the stellar spectrum which tries to avoid splitting up stellar lines between adjacent chunks. As one can see, the chunks contain only a few deep stellar lines or sometimes none. To quantify this, we calculated the quality factor Q (Connes, 1985; Butler et al., 1996; Bouchy et al., 2001) for each chunk in the stellar template obtained via deconvolution for a stellar spectrum taken without iodine cell. This factor sums in a flux-weighted way the squared gradients in a spectrum[7], hence measuring its RV information content. For photon noise, the estimated RV uncertainty is inversely proportional to Q, i.e. $\Delta RV \sim \frac{1}{Q}$. Hence, we weight each chunk RV with Q^2 when computing the RV mean. Chunks with $Q < 7000$ were discarded (cf. Fig. 4.2, right axis). For comparison, the quality factor is Q=12857 for the whole spectral range in Fig. 4.2 and $Q = 67000$ for an

[7] $Q = \sqrt{\frac{\sum A(i)\left(\frac{\partial \ln A(i)}{\partial \ln \lambda(i)}\right)^2}{\sum A(i)}}$, where $A(i)$ is the flux in the i-th pixel.

iodine spectrum (spectrum of a featureless B-star taken through the iodine cell).

The stellar spectrum can be shifted across the CCD by several pixels due to the barycentric velocity of the Earth (that we have calculated with the JPL ephemerides DE200, e.g. Standish 1990) and offsets in the instrument setup. To always have the same stellar lines in a chunk, we shifted the chunks back for compensation (1 pixel $\sim$ 500 m/s). So instead of having fixed chunk positions with respect to the CCD as originally implemented in the AUSTRAL code, this modification ensures always the same weighting factor for each chunk.

For τ Cet (GJ 71, HIP 8102, HR 509, HD 10700) which is known as an RV constant star (in our HARPS data it is constant to 4 m/s), we achieve with the CES+VLC a long-term precision of 8.1 m/s (Fig. 4.12, Table 4.3). The internal RV errors of the individual spectra ($\sim$8.8 m/s), calculated as the errors of the mean RV of the chunks (rms/$\sqrt{N_{\rm chunk}}$), are of the same order as the rms of the time series implying a fair error estimation.

4.3.5 Combining the LC and VLC data

The problem of instrumental offsets, i.e. different radial velocity zero points, occurs when data sets originate from different instruments (e.g. Wittenmyer et al., 2006) or after instrumental changes/upgrades. For instance, an offset of -1.8 m/s was reported by Rivera et al. (2010) after upgrading the Keck/HIRES spectrograph with a new CCD. An offset of only 0.9 m/s was mentioned by Vogt et al. (2010) when combining Keck and AAT data.

As described above we have used three different instruments/instrument configurations and we are also faced with the problem of the instrumental offset. There are basically two different methods for combining the data sets: (1) Simply fitting the offset, i.e. the data sets are considered to be completely independent and the zero points are free parameters in the model fitting. (2) If possible, measuring the offset physically by making use of some known relation between the data sets/instruments to keep the offset fixed.

In fact, we can measure the offset for the LC and VLC data albeit with a limited precision. The LC and VLC spectra were taken through the same iodine cell, i.e. the same wavelength calibrator. Because Endl et al. (2002) calculated the LC RV with different stellar templates and an iodine spectrum of lower resolution than used in this work, we re-calculated the RVs for all LC spectra with the same VLC stellar template (which is shorter than the LC spectra) and the new iodine cell scan to have the same reference for the LC and VLC. The re-calculated RVs are verified to have a precision similar to the published LC data.

Then we computed the mean of the re-calculated LC and VLC time series. If a star has a constant RV, one would expect that the means of both time series are the same, i.e. the offset $\overline{\rm RV}_{\rm VLC} - \overline{\rm RV}_{\rm LC} = 0$ within the uncertainties of the means ($\sigma_{\rm LC}$ and σ_{VLC}). This can be tested with the t-statistics, in particular Welch's t-test (for two independent samples with unequal sizes and variances). We suggest that keeping the offset fixed is valid, if the quantity

$$t = \frac{\overline{RV}_{\rm LC} - \overline{RV}_{\rm VLC}}{s} \quad \text{with} \quad s = \sqrt{\frac{\sigma_{\rm LC}^2}{N_{\rm LC}} + \frac{\sigma_{VLC}^2}{N_{\rm VLC}}} \tag{4.1}$$

is not rejected by the Null-hypothesis. s is an estimate for the standard error of the difference in the means and is calculated from sample variances σ_i^2 and sample sizes N_i. t follows a t-distribution with ν degrees of freedom[8]. For instance, for $|t| > 1.7$ and $\nu > 30$ the difference in the means is significant with a false alarm probability of FAP<10%. For some of our stars the FAP for the offset difference is not significant: δ Eri (64%), ε Eri (23%), HR 209 (92%), and HR 3259 (15%). However, from Fig. 4.3 it can be seen that there are also stars having significant offsets leaving doubts whether the offset can be kept fixed in general.

[8]The effective degree of freedom is $\nu = \frac{(s_1^2/N_1 + s_2^2/N_2)^2}{(s_1^2/N_1)^2/(N_1-1) + (s_2^2/N_2)^2/(N_2-1)}$ where s_1^2 and s_2^2 are the sample variances.

Figure 4.3 shows that for our sample an average offset of 10.4 m/s (±7.7 m/s) remains for the RV constant stars when comparing the RV means of the VLC and LC data. This offset might be due to systematics in the deconvolution process of the stellar template or in the modelling. E.g. due to the different resolution, the LC data have to be modelled with a different chunk size (154 pixels to cover two VLC chunks). We corrected all re-calculated LC RVs for this systematic offset. Finally, we adjusted the RV mean of the published LC time series (Endl et al., 2002) to fit the RV mean of the re-calculated time series. In Figs. 4.12–4.16 the LC and VLC data are always shown relative to each other with the measured and corrected offset (and *not* with a fitted RV offsets from Sect. 4.4) to conserve the true measurements.

The uncertainty of the offset found in the sample is rather large for the offset to be considered a fixed value. On the other hand the approximately known offset can hold important information, in particular in the case of HR 2400 or ε Ind A. Therefore we choose a compromise between a fixed offset and a free offset when fitting a function. Because one expects the difference of the zero point parameters to be zero ($c_{\mathrm{VLC}} - c_{\mathrm{LC}} \approx 0$), we introduce in the χ^2-fitting a counteracting potential term η^2, that increases when the zero point difference becomes larger

$$\hat{\chi}^2 = \chi^2 + \eta^2 \quad \text{with} \quad \eta = \frac{c_{\mathrm{VLC}} - c_{\mathrm{LC}}}{s}.$$

The resulting χ^2 (when minimising $\hat{\chi}^2$) will be higher compared to that obtained when fitting with free offsets but lower than for fixed offsets. The parameter s determines the coupling between the offsets. After performing the fit it can be checked, if the fit has spread the zero points too much (if $\eta \gg 1$ or if there are large jumps in the model curves in Figs. 4.12–4.16). For s we attributed the uncertainty of the offset correction of 7.7 m/s leading to a weak coupling.

It is worth mentioning, that in Bayesian analysis $\hat{\chi}^2$ can be identified with the likelihood when assuming a Gaussian distribution for the prior information that the expected zero point difference is zero.

4.3.6 Combining the CES and HARPS data

In principle, VLC and HARPS data could be combined in a similar way. They have different wavelength calibrators, but they are closely related in time since there are almost simultaneous measurements. The difference between these consecutive measurements should be zero so that it is tempting to bind the time series directly. However, this does not account for fluctuations due to the individual uncertainties. Again a coupling term[9] would be a more secure approach.

However, for reasons of simplicity we choose a fully free offset between the HARPS and the CES data. Because the VLC and the HARPS time series are well overlapping this is less critical, in contrast to the LC and VLC time series which are separated by a 2-year gap. The relative offsets between the CES and HARPS data as illustrated in Figs. 4.12–4.16 correspond to the common best fitting model (constant, slope, sinusoid, or Keplerian; cf. Sect. 4.4).

4.4 Analysis of the radial velocities

Before the data analysis we have binned the data into 2-hr intervals by calculating weighted means for the temporal midpoint, RV, and RV error. The 2-hr interval will especially down-weight nights with asteroseismology campaigns (see Sect. 4.3.3). Such intervals are employed for solar-like stars to average out the stellar jitter, i.e. intrinsic stellar RV variation caused by, e.g., oscillation or granulation in the atmospheres of the stars. In our survey we have usually taken three consecutive spectra in one night covering only 5–10 min. To estimate the short-period jitter, we calculated the weighted scatter[10] in each

[9] For one simultaneous measurement taken at the time t_s, this term could be written as $\eta = \dfrac{c_{\mathrm{H}} - c_{\mathrm{VLC}}}{\sqrt{\Delta RV_{\mathrm{H}}(t_s)^2 + \Delta RV_{\mathrm{VLC}}(t_s)^2}}$ where c is the zero point parameter, $\Delta RV(t_s)$ are the individual errors of the simultaneous measurements, and the indices H (HARPS) and VLC indicate the instruments. The VLC time series must be a priori adjusted by a zero point such that $RV_{\mathrm{VLC}}(t_s) := RV_{\mathrm{H}}(t_s)$.

[10] Weighting of the i-th measurement with its internal error $w_i \sim 1/\sigma^2_{\mathrm{int},i}$.

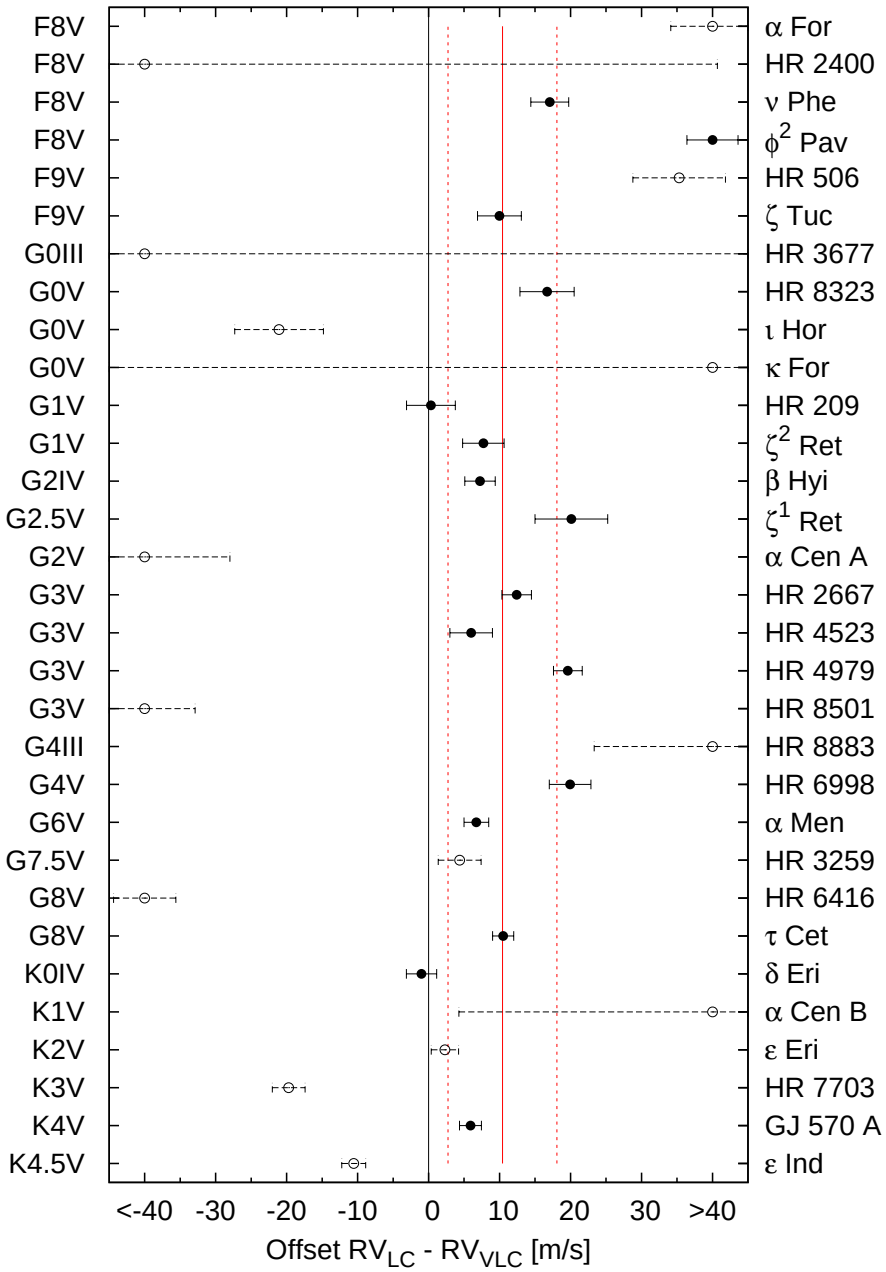

Figure 4.3: Difference between the means of the VLC and re-computed LC time series for all our stars ordered by spectral type. For RV constant stars (black filled circles) there occurs a systematic offset of 10.4±7.7 m/s (red solid line and red dashed lines). Stars shown with open circles were not included in the offset analysis (for reasons see comments in Table 4.3). The shown error bars correspond to the uncertainty in the means, i.e. parameter s from Eq. (4.1).

2-hr bin with at least 2 measurements and then the weighted mean of these scatters[11]. Table 4.10 lists the jitter estimate for each star and the mean time scale accessible for this estimate. Note that these time scales may not sufficiently cover the real jitter time scale in all cases.

There can be also a long-term jitter related to the rotation period or activity cycle of a star. Isaacson & Fischer (2010) provide jitter estimates as a function of $B-V$ colour and chromospheric activity index

[11] Weighting of the j-th bin with the number of measurements n_j and the mean internal error in that bin: $w_j \sim n_j/\sigma^2_{\mathrm{int},j}$. Note that bins with more measurements usually cover larger time intervals and get more weight.

$S_{\rm HK}$ based on Keck observations for more than 2600 main sequence star and subgiants. We use these relations to estimate the jitter for our stars (Table 4.10). These jitter terms were added in quadrature to the internal errors for all stars and lead to a more balanced fit with the CES data.

During the fits we account for the secular acceleration of the RVs. This perspective effect can become a measurable positive trend in some high proper motion stars (Schlesinger, 1917; Kürster et al., 2003; Zechmeister et al., 2009). In our sample, ε Ind A has the highest secular acceleration with 1.8 m/s/yr. Its contribution is depicted in Fig. 4.16 by a grey dashed line.

4.4.1 Excess variability

To investigate objects for excess variability it is common to compare the observed scatter with a noise estimate. A significantly larger scatter indicates variability. Because internal errors ΔRV_i and jitter estimations $\sigma_{\rm jit}$ are available, the quality of each measurement is assessed and allows to weight the measurements in the χ^2-statistics, $w_i = \frac{1}{\sigma_i^2} = \frac{1}{\Delta RV_i^2+\sigma_{\rm jit}^2}$. As the scatter we calculate the weighted unbiased rms which is here defined as

$$\mathrm{rms} = \sqrt{\frac{N}{N-\nu}\frac{1}{W}\sum_{i=1}^{N}\frac{(RV_i - f(t_i))^2}{\sigma_i^2}} = \sqrt{\frac{N}{N-\nu}\frac{\chi^2}{W}} \tag{4.2}$$

where $W = \sum w_i$ is the sum of the weights and ν the number of model parameters. Outliers with a large uncertainty will contribute less to the rms. The factor $\frac{N}{N-\nu}$ is a correction that converts the biased variance into an unbiased variance. In the unweighted case ($w_i = 1$, $W = N$) we obtain the well known formula for the unbiased rms: $\mathrm{rms} = \sqrt{\frac{1}{N-\nu}\sum(RV_i - f(t_i))^2}$.

Furthermore, we define the weighted mean noise term σ via the mean of the weights[12]

$$\sigma = \frac{1}{\sqrt{\langle w_i\rangle}} = \sqrt{\frac{N}{W}} = \sqrt{\frac{N}{\sum_{i=1}^{N}\frac{1}{\sigma_i^2}}}. \tag{4.3}$$

Again lower-quality measurements will contribute less to the mean noise level.

With these definitions the reduced χ^2 can be easily expressed as the ratio of weighted rms to weighted mean noise level

$$\chi^2_{\rm red} = \frac{\chi^2}{N-\nu} = \frac{\mathrm{rms}^2}{\sigma^2}. \tag{4.4}$$

To test for excess variability we have to fit a constant and to calculate the scatter around the fit. For the joint analysis we account for the zero point parameter of each data set when fitting a constant as outlined in Sect. 4.3.5. Table 4.4 summarises for the combined data set the weighted noise term σ, the weighted rms, and the χ^2-probability for this test. Table 4.11 lists additionally the individual rms for each instrument. These values can differ from Table 4.3, because in Table 4.4 secular acceleration is accounted for, jitter has been added, the data are binned, and the LC and VLC offsets are coupled. Because the HARPS data have a much higher precision, they dominate the statistics.

The small χ^2-probabilities for most of the stars indicate that they are variable with respect to our noise estimate σ. However, ζ Tuc, ν Phe, τ Cet[13], ζ^2 Ret, δ Eri, α Men, HR 2667, HR 6998, ϕ^2 Pav, and HR 8323 have $\mathrm{Prob}(\chi^2) > 1\%$, i.e. they show only low or no excess variability. There are also cases where the scatter is smaller than the noise level, i.e. $\chi^2_{\rm red} < 1$, implying an overestimation of the noise level for HR 2667, HR 6998, and HR8323. The jitter estimate for these star is 2.66 m/s, 2.84 m/s, and 3.09 m/s (Table 4.10), while the HARPS measurement have a scatter of only 1.44 m/s, 1.79 m/s, and 2.94 m/s of (Table 4.11), respectively.

[12] Another point of view leads to the same result: Gaussian errors are added in quadrature. Hence the trivial weighted mean is $\sqrt{\frac{1}{W}\sum w_i\sigma_i^2} = \sqrt{\frac{1}{W}\sum 1} = \sqrt{\frac{N}{W}}$.

[13] The last RVs of τ Cet seems to have a systematic offset of $\sim$6 m/s. The reason is not known to us. However, when excluding the last 100 days of RV measurements (70 binned data points), there is no significant variability, trend, or periodicity for the known RV constant star τ Cet.

Table 4.4: Summary of the tests for excess variability, slope, and periodicities (sinusoidal and Keplerian) for the combined data set. Significant trends and periods are printed in bold face (FAP$<1\%$). The index r indicates tests on residuals (see Sect. 4.4.5).

Star	$N_{\rm bin}$	T [yr]	σ [m/s]	rms [m/s]	Prob(χ^2)	$\rm rms_{slope}$ [m/s]	slope [m/s/yr]	FAP
ζ Tuc	72	14.9	5.01	5.51	0.11	5.55	-0.22	1
β Hyi	107	16.0	3.55	4.62	$1.4\cdot10^{-5}$	3.89	2.13	$\mathbf{1.6\cdot10^{-9}}$
HR 209	53	14.0	7.55	9.86	0.0014	9.72	1.70	0.13
ν Phe	71	14.9	4.81	5.52	0.041	5.48	-0.91	0.18
HR 506	51	14.0	5.77	14.48	$1.7\cdot10^{-38}$	14.57	-1.39	0.51
HR 506$_{\rm r}$				6.85	0.033	6.13	-2.53	**0.00075**
τ Cet	212	16.2	2.53	3.53	$9.1\cdot10^{-15}$	3.21	0.88	$\mathbf{1.7\cdot10^{-10}}$
τ Cet[13]	142	15.9	2.75	2.82	0.32	2.78	-0.35	0.025
κ For	78	14.8	3.77	718.44	0	50.54	-700.74	**0**
κ For$_{\rm r}$				4.11	0.13	4.10	0.36	0.31
ι Hor	152	14.8	5.90	29.88	0	29.97	1.07	0.77
ι Hor$_{\rm r}$				11.16	$1.1\cdot10^{-44}$	11.07	-1.73	0.072
α For	75	14.8	4.58	13.04	0	4.83	-11.20	$\mathbf{1.4\cdot10^{-32}}$
α For$_{\rm r}$				4.75	0.31	4.78	0.04	0.9
ζ^1 Ret	48	9.9	5.22	12.04	$2.9\cdot10^{-28}$	11.19	-3.94	0.0066
ζ^2 Ret	76	14.8	6.14	7.26	0.014	7.25	0.67	0.25
ε Eri	77	14.8	5.50	8.61	$5.7\cdot10^{-11}$	8.66	0.29	0.78
δ Eri	60	14.8	3.22	3.45	0.21	3.46	0.38	0.42
α Men	107	14.2	3.17	3.20	0.41	3.06	0.83	0.0012
HR 2400	77	14.4	4.57	268.97	0	216.26	-103.32	$\mathbf{1.1\cdot10^{-8}}$
HR 2400$_{\rm r}$				5.54	0.0053	5.42	-1.21	0.047
HR 2667	89	14.4	4.99	3.18	1	3.20	-0.03	0.95
HR 3259	63	14.2	3.85	5.71	$2.8\cdot10^{-7}$	5.70	-0.44	0.27
HR 3677	60	14.4	3.51	1002.86	0	234.84	834.34	$\mathbf{3.3\cdot10^{-37}}$
HR 3677$_{\rm r}$				8.86	0	8.94	0.15	0.85
HR 4523	81	15.3	3.52	4.88	$1.8\cdot10^{-6}$	4.81	0.64	0.075
HR 4979	73	14.6	4.09	5.17	0.0011	4.84	-1.55	0.0015
α Cen A	121	14.4	3.37	121.23	0	11.32	133.94	**0**
α Cen A$_{\rm r}$				2.90	0.98	2.92	-0.01	0.96
α Cen B	93	14.4	3.69	250.44	0	17.33	-159.23	**0**
α Cen B$_{\rm r}$				4.71	0.00015	4.73	-0.05	0.85
GJ 570 A	68	12.0	2.72	5.44	$4.2\cdot10^{-25}$	3.85	-3.01	$\mathbf{2\cdot10^{-11}}$
HR 6416	76	14.5	4.09	11.19	0	4.07	9.40	$\mathbf{1.4\cdot10^{-33}}$
HR 6416$_{\rm r}$				3.89	0.7	3.92	0.07	0.81
HR 6998	63	14.3	4.92	3.47	1	3.49	-0.53	0.57
HR 7703	56	13.2	3.21	4.77	$1\cdot10^{-6}$	2.45	3.49	$\mathbf{7.4\cdot10^{-17}}$
HR 7703$_{\rm r}$				2.40	1	2.42	0.01	0.98
ϕ^2 Pav	87	14.8	6.10	7.16	0.013	7.19	0.08	0.71
HR 8323	47	12.8	4.26	3.96	0.73	3.93	-0.50	0.22
ε Ind A	99	15.7	2.66	5.45	$2.6\cdot10^{-39}$	3.67	2.52	$\mathbf{3.2\cdot10^{-18}}$
HR 8501	77	14.8	5.88	20.29	0	5.01	17.15	**0**
HR 8501$_{\rm r}$				4.96	0.97	4.98	0.17	0.61
HR 8883	45	13.3	6.43	62.49	0	62.82	-6.49	0.46
HR 8883$_{\rm r}$				29.94	0	30.30	0.13	0.94

Table 4.5: Continuation of Table 4.4.

Star	rms_{sin} [m/s]	P_{sin} [d]	FAP	rms_{Kep} [m/s]	P_{Kep} [d]	FAP
ζ Tuc	5.09	1.60	1	4.05	1.95	$2.9 \cdot 10^{-5}$
β Hyi	3.65	1.00	$\mathbf{7.6 \cdot 10^{-8}}$	3.42	1.00	$2 \cdot 10^{-9}$
HR 209	7.49	1.24	0.0036	6.58	3.17	$9.2 \cdot 10^{-5}$
ν Phe	4.90	1.98	0.58	4.62	1.48	0.11
HR 506	7.07	963.01	$\mathbf{9 \cdot 10^{-12}}$	7.06	962.63	$2.6 \cdot 10^{-10}$
HR 506_r	5.47	2.43	0.059	4.93	1.87	0.0047
τ Cet	2.74	268.00	$\mathbf{3.2 \cdot 10^{-20}}$	2.27	5295.54	$3.1 \cdot 10^{-35}$
τ Cet[13]	2.59	30.57	0.023	0.00	0.00	0
κ For	8.56	>30 yr	$\mathbf{7.3 \cdot 10^{-138}}$	4.27	9706.51	$2.6 \cdot 10^{-154}$
κ For_r	3.69	2084.67	0.57	3.54	3.11	0.2
ι Hor	14.59	307.09	$\mathbf{3.6 \cdot 10^{-43}}$	11.31	306.94	$3.2 \cdot 10^{-57}$
ι Hor_r	9.43	5.71	$\mathbf{3.6 \cdot 10^{-8}}$	9.15	7.95	$6.5 \cdot 10^{-9}$
α For	4.82	>30 yr	$\mathbf{1.1 \cdot 10^{-27}}$	4.76	7652.36	$4.4 \cdot 10^{-26}$
α For_r	4.08	345.29	0.053	4.04	99.73	0.14
ζ^1 Ret	8.77	426.82	0.0016	7.52	21.41	$3.2 \cdot 10^{-5}$
ζ^2 Ret	6.80	1.23	1	5.88	1.01	0.005
ε Eri	7.20	6.30	0.0054	6.47	1.49	$2.8 \cdot 10^{-5}$
δ Eri	3.01	2.39	0.69	2.68	1.70	0.014
α Men	2.93	1.02	0.19	2.71	9.57	0.00066
HR 2400	108.05	5859.67	$\mathbf{6 \cdot 10^{-26}}$	5.83	9494.06	$8.5 \cdot 10^{-113}$
HR 2400_r	5.25	1.33	1	4.47	6.29	0.0032
HR 2667	2.92	3.49	0.81	2.78	1.01	0.12
HR 3259	4.62	1.12	0.009	4.13	2.25	0.00016
HR 3677	32.89	>30 yr	$\mathbf{4.6 \cdot 10^{-79}}$	9.17	>30 yr	$1.9 \cdot 10^{-104}$
HR 3677_r	6.14	8.79	$\mathbf{3.4 \cdot 10^{-6}}$	5.37	62.18	$4.2 \cdot 10^{-8}$
HR 4523	4.46	1.44	0.87	3.31	5.07	$5.2 \cdot 10^{-9}$
HR 4979	4.36	1.34	0.02	3.76	1.33	$1 \cdot 10^{-5}$
α Cen A	3.35	>30 yr	$\mathbf{3.2 \cdot 10^{-178}}$	2.95	>30 yr	$5.5 \cdot 10^{-180}$
α Cen A_r	2.61	3.97	0.0079	2.51	3.97	0.00073
α Cen B	4.87	>30 yr	$\mathbf{4.7 \cdot 10^{-148}}$	4.82	>30 yr	$8.6 \cdot 10^{-144}$
α Cen B_r	4.10	1.01	0.011	3.71	387.95	$1.9 \cdot 10^{-5}$
GJ 570 A	3.87	>30 yr	$\mathbf{8.3 \cdot 10^{-7}}$	3.69	2444.42	$6.3 \cdot 10^{-7}$
HR 6416	3.95	>30 yr	$\mathbf{1.6 \cdot 10^{-29}}$	4.01	>30 yr	$4.1 \cdot 10^{-27}$
HR 6416_r	3.66	13.49	1	3.31	1.22	0.12
HR 6998	3.09	3.47	0.9	2.91	717.43	0.33
HR 7703	2.45	>30 yr	$\mathbf{2.8 \cdot 10^{-12}}$	2.39	5690.56	$2.7 \cdot 10^{-11}$
HR 7703_r	2.10	2.38	0.84	1.83	1.34	0.017
ϕ^2 Pav	6.54	1.90	0.71	6.25	4.64	0.16
HR 8323	3.29	1.38	0.56	2.80	1.93	0.0087
ε Ind A	3.57	3827.54	$\mathbf{1.1 \cdot 10^{-14}}$	3.49	1969.69	$3.9 \cdot 10^{-14}$
HR 8501	5.05	>30 yr	$\mathbf{6.6 \cdot 10^{-41}}$	5.01	6704.59	$8.2 \cdot 10^{-39}$
HR 8501_r	4.46	1.47	0.61	4.24	2.17	0.14
HR 8883	30.78	7.60	$\mathbf{9.2 \cdot 10^{-10}}$	25.65	13.08	$2.5 \cdot 10^{-11}$
HR 8883_r	18.01	3.00	$\mathbf{2.7 \cdot 10^{-6}}$	15.84	1.19	$3.4 \cdot 10^{-7}$

Listed are the number of binned observations N_{bin}, the combined time baseline T, the mean combined noise term σ (including jitter), the combined weighted rms of the time series, the χ^2-probability for fitting a constant, and the false alarm probabilities (FAP) for the other tests. Also listed are the weighted scatter of the residuals (rms_{slope}, rms_{sin}, rms_{Kep}) and some best-fitting parameters (slope and the periods P_{sin} and P_{Kep}).

Table 4.6: Information about wide companions. Listed are separation, period estimate, references, and our estimates for minimum masses $M_{\rm min}$ from measured slopes via Eq. (4.5). Minimum masses in brackets were derived from non-significant trends.

Star	Companion	ρ [″]	ρ [AU]	P [yr]	Ref.	$M_{\rm min}$ [$M_{\rm Jup}$]	further companions
α For	GJ 127 B (G7V)	4.4	62	314	[BP, H, P]	236	
α Men	HD 43834 B (M3.5)	3.05	31		[E]	(4)	
HR 2667	GJ 9223 B (K0V)	20.5	332		[F, WD]	(6)	
HR 4523	GJ 442 B (M4V)	25.4	234		[P]	(181)	
GJ 570 A	GJ 570 BC (M1.5V+M3V)	24.7	146		[B]	358	GJ 570 D (T, 258.″3)
HR 6416	GJ 666 B (M0V)	10.4	92	550	[LH, P]	432	GJ 666 C (M6.5V, 41.″8)
							GJ 666 D (M7V, 40.″7)
HR 7703	GJ 783 B (M3.5)	7.1	43		[P]	35	
ε Ind A	GJ 845 Bab (T1+T6)	402.3	1459		[S]	29920	
HR 8501	GJ 853 B ($V < 10$ mag)	2.5–3.4	41		[M, WD]	163	

References: [BP] Baize & Petit (1989), [B] Burgasser et al. (2000), [E] Eggenberger et al. (2007), [F] Favata et al. (1997), [H] Heintz (1978), [LH] Luyten & Hughes (1980), [M] Mason et al. (2001), [P] Poveda et al. (1994), [S] Scholz et al. (2003), [WD] Worley & Douglass (1997).

4.4.2 Long-term trends

Because potential planets or companions can have orbital periods much longer than our observations, these objects may betray themselves by a trend in the RVs. We searched for trends by fitting a slope to the data and derived its significance via the fit improvement with respect to the constant model (previous Sect.) via

$$F_{\rm slope} = (N-4)\frac{\chi^2_{\rm constant} - \chi^2_{\rm slope}}{\chi^2_{\rm slope}}$$

or when expressed with unbiased weighted variances

$$F_{\rm slope} = \frac{(N-3)\,{\rm rms}^2_{\rm constant} - (N-4)\,{\rm rms}^2_{\rm slope}}{{\rm rms}^2_{\rm slope}}.$$

The associated probability for this F-value follows a $F_{1,N-4}$-distribution (4 parameters: 1 slope, 3 zero points). Again Table 4.4 summarises the test for long-term trends. When adopting a false alarm probability threshold of $< 10^{-3}$ fitting a slope improves significantly the rms of all binaries (κ For, α For, HR 2400, HR 3677, α Cen A, α Cen B, HR 6416, HR 7703, and HR 8501) as well as that of β Hyi, GJ 570 A, and ε Ind A. We note that for β Hyi, α For, GJ 570 A, HR 6416, HR 7703, ε Ind A, and HR 8501 the trend is a sufficient model (regarding sinusoid and Keplerian fit, see next Section), because of the smaller FAP or unbiased weighted rms. For these stars the trend is depicted in Figs. 4.12–4.16.

Some of our stars have known wide visual companions with a known separation ρ listed in Table 4.6. Whether these objects are able to cause the observed trend, can be verified by the estimate ($\ddot{r}_{\rm A} = G\frac{m_{\rm B}}{r^2}$)

$$m_{\rm B} \geq \frac{|\ddot{z}_{\rm A}|r^2}{G} \geq \frac{|\ddot{z}_{\rm A}|\rho^2}{G} = 5.6\cdot10^{-3} M_{\rm Jup}\frac{|\ddot{z}_{\rm A}|}{\rm m/s/yr}\left(\frac{\rho}{\rm AU}\right)^2 \tag{4.5}$$

with the radial acceleration $|\ddot{z}_{\rm A}| < \ddot{r}_{\rm A}$ of the observed component A and the projected separation $\rho < r$ between both components. For comparison, Jupiter at 5.2 AU can accelerate the Sun by 6.6 m/s/yr. Table 4.6 shows that the minimum companion masses derived from the measured slopes are below 0.5 $M_\odot$ for α For, GJ 570 A, HR 6416, HR 7703, and HR 8501. These masses are in agreement with the masses as expected from the spectral type of their companions. However, ε Ind B (112 $M_{\rm Jup}$, King et al. 2010)

is too far from ε Ind A. It can induce only an acceleration of 0.009 m/s/yr and hence cannot explain the measured trend.

The other possibility for a trend is an unknown and unseen companion. Whether the strength and the long duration of a trend is still compatible with a planetary companion, can be estimated more conveniently, when Eq. (4.5) is expressed in terms of the orbital period P which is also unknown but has to be (for circular orbits) at least twice as large as the time span of observations T. With Kepler's 3rd law $\frac{a^3}{P^2} = G\frac{M+m}{4\pi^2}$, Eq. (4.5) can be written as

$$\begin{aligned} m_\mathrm{B} &\geq G^{-1/3}|\ddot{z}| \left(\frac{P}{2\pi}\right)^{4/3} (M_\mathrm{A}+m_\mathrm{B})^{2/3} \\ &= 5.6\cdot 10^{-3} M_\mathrm{Jup} \frac{|\ddot{z}|}{\mathrm{m/s/yr}} \left(\frac{P}{\mathrm{yr}}\right)^{4/3} \left(\frac{M_\mathrm{A}+m_\mathrm{B}}{\mathrm{M}_\odot}\right)^{2/3} \end{aligned} \tag{4.6}$$

For ε Ind A we find its companion to have $m\sin i \gtrsim 1.11\,M_\mathrm{Jup}$ for $P > 30$ yr. The trend for ε Ind A originally announced by Endl et al. (2002) is probably of highest interest since it might be caused by a planet. The common slope of 2.5 m/s/yr is predominantly based on the more precise HARPS data. This trend improves the individual rms of the LC and VLC only slightly (see Table 4.11), however the rms for both data sets is close to or below the stated precision. The scatter of the VLC data is even only 4.5 m/s, making it the most precise star in the VLC data set[14]. In the overall picture the trend seems to be present for the whole observation. The fit spreads the offset between LC and VLC to -7.0 m/s (Table 4.13, visible as the jump in the fit in Fig. 4.16, $\eta = 0.91$), i.e. is consistent with our physically estimated offset.

For β Hyi Endl et al. (2002) announced a trend of 7 m/s/yr with a remaining scatter of 19 m/s. Here the best common trend is only 2.13 m/s/yr depicted with a black solid line in Fig. 4.12 (plus the secular acceleration of 0.86 m/s). The scatter around the HARPS data decreases to only 2.9 m/s. However, the trend increases the VLC scatter from 7.4 m/s to 9.5 m/s (see Table 4.11) and the fitted LC-VLC offset departs by 2.7σ (-21 m/s, Table 4.13) from the measured offset. Thus, it is ambiguous whether the trend is steady.

4.4.3 Search for Periodicities and Keplerian orbits

To search for the best-fitting sinusoidal and Keplerian orbits, we employed the generalised Lomb-Scargle (GLS) algorithm described in Zechmeister & Kürster (2009). It was adapted to treat all three data sets with different offsets and also incorporates the weak coupling described before. Searching for sine waves is a robust method to find periodicities and orbits with low eccentricities, while for highly eccentric orbits the Keplerian model should be applied.

Figures 4.4–4.7 shows the periodograms for some of the stars discussed here. The periodograms for the rest of the stars are available in Sect. 4.8. The periodograms are normalised as

$$p = \frac{\chi^2_\mathrm{constant} - \chi^2_\mathrm{sin}}{\chi^2_\mathrm{constant}} \quad \text{and} \quad p_\mathrm{Kep} = \frac{\chi^2_\mathrm{constant} - \chi^2_\mathrm{Kep}}{\chi^2_\mathrm{constant}}.$$

involving the χ^2 of the constant, sinusoidal, and Keplerian model, respectively. Analogous to Cumming et al. 2008 and Zechmeister & Kürster (2009), we calculated the probabilities of the power values for the best-fitting sinusoid and Keplerian orbit (p_best and $p_\mathrm{Kep,best}$) via

$$\begin{aligned} \mathrm{Prob}(p > p_\mathrm{best}) &= (1-p_\mathrm{best})^{\frac{N-5}{2}} \quad \text{and} \\ \mathrm{Prob}(p_\mathrm{Kep} > p_\mathrm{Kep,best}) &= (1+\tfrac{N-7}{2}p_\mathrm{Kep,best})(1-p_\mathrm{Kep,best})^{\frac{N-7}{2}}, \end{aligned}$$

[14] ε Ind A has the spectral type K which has numerous stellar lines (high quality factor Q, Bouchy et al. 2001) allowing more precise RV measurements.

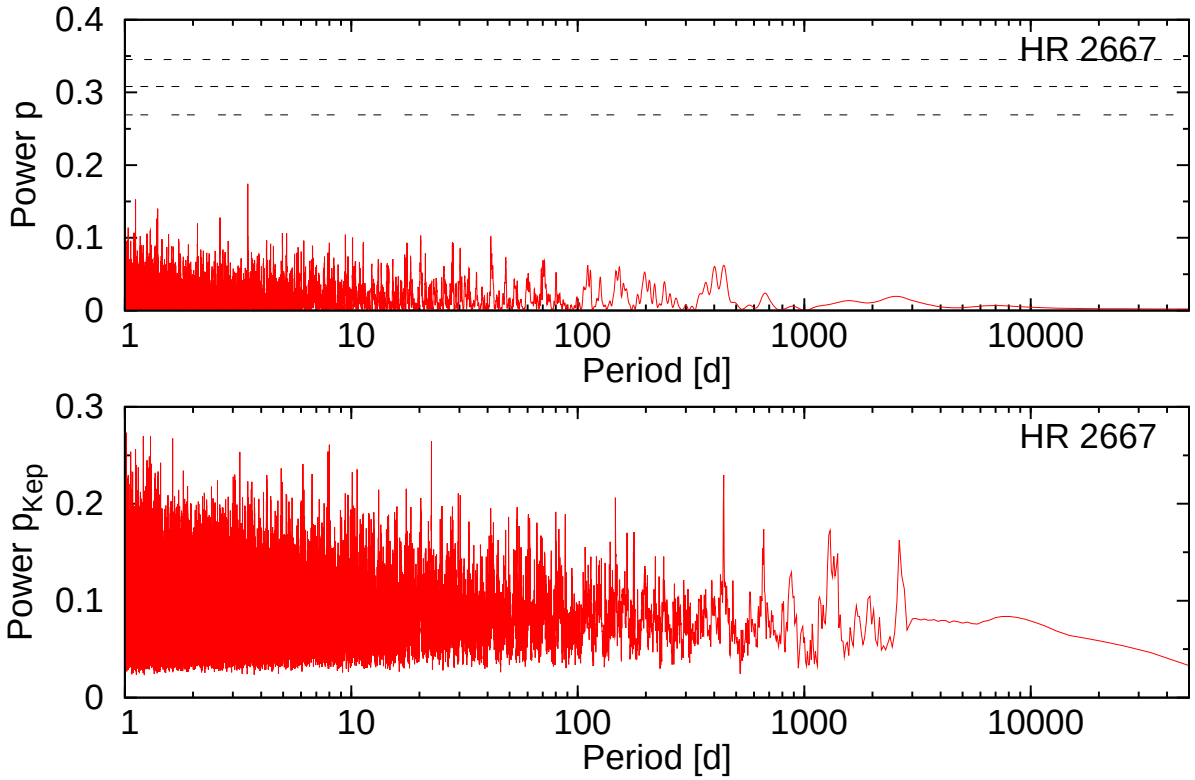

Figure 4.4: GLS (top) and Keplerian (bottom) periodogram for HR 2667 which is constant to 3.1 m/s. The horizontal lines mark the 10^{-2}, 10^{-3}, and 10^{-4} false alarm probabilities (FAP).

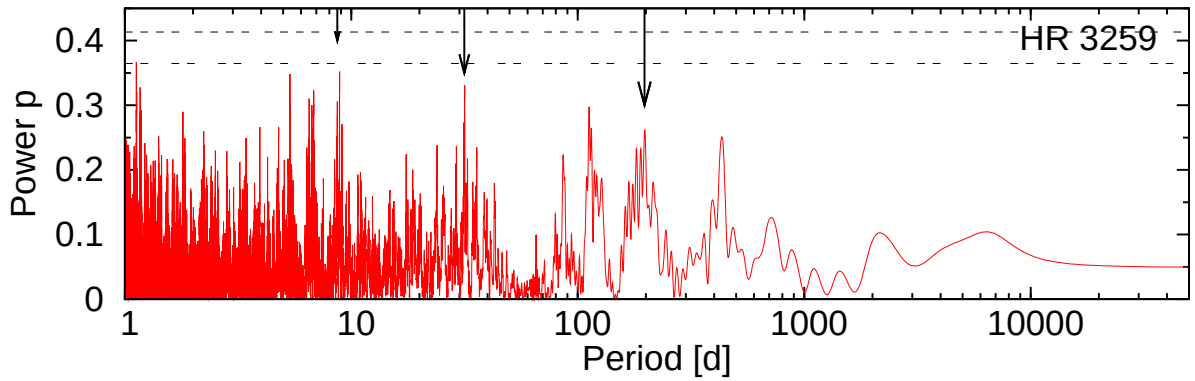

Figure 4.5: GLS periodogram for HR 3259. The vertical arrows indicate the periods for the three planets announced by Lovis et al. (2006).

respectively. Compared to the probility functions given by these authors which account for one offset, here are slight modifications in the equations (numerator in the fractional terms decreased by 2) arising from the three zero points, i.e. two more free parameters[15].

The final false alarm probability (FAP) for the period search accounts for the number of independent frequencies M with the simple estimate $M \approx fT$ (Cumming, 2004), i.e. the frequency range f and the time baseline T, and is given by

$$\mathrm{FAP} = 1 - [1 - \mathrm{Prob}(p > p_{\mathrm{best}})]^M$$

[15]The corresponding normalisation as $z = \frac{(\chi^2_{\mathrm{constant}} - \chi^2)/(\nu - \nu_{\mathrm{constant}})}{\chi^2_{\mathrm{best}}/(N-\nu)}$ follows a $F_{2,N-5}$ and $F_{4,N-7}$-distribution, respectively.

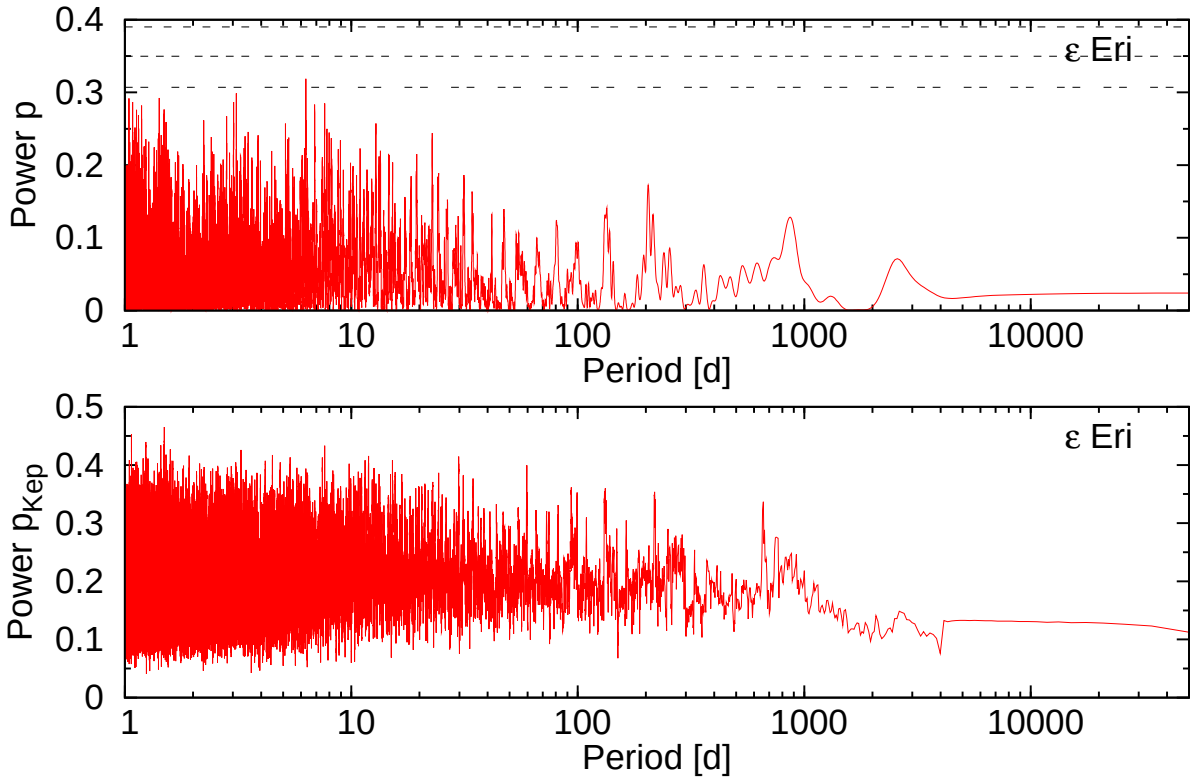

Figure 4.6: GLS (top) and Keplerian (bottom) periodogram for ε Eri. There is no significant power at the period of the putative planet ε Eri b ($P = 2500$ d).

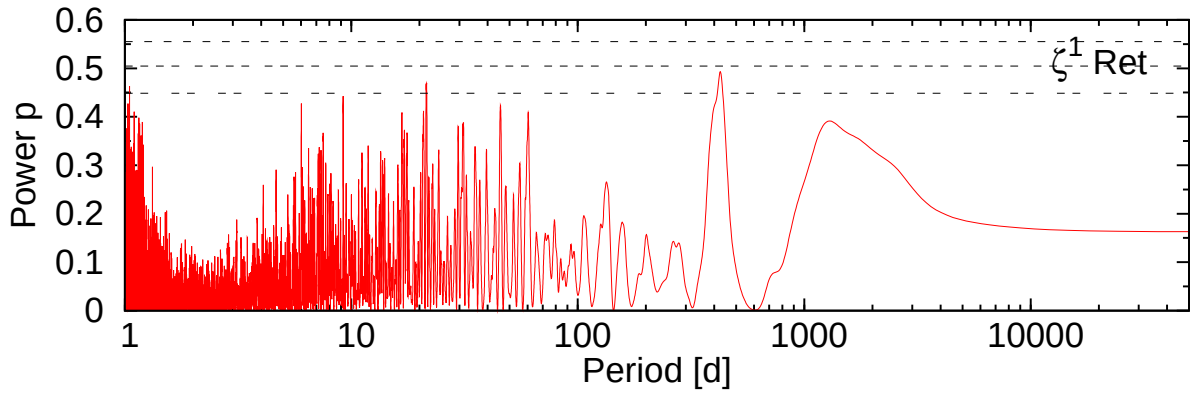

Figure 4.7: GLS periodogram for ζ^1 Ret.

and can be approximated by FAP $\approx M \cdot \mathrm{Prob}(p > p_{\mathrm{best}})$ for FAP $\ll 1$. Since our frequency search interval ranges from 0 to 1 d^{-1}, we have typically $M \sim 5500$ for a 15 year time baseline.

Table 4.4 summarises the formal best-fitting sinusoidal and Keplerian periods (P_{sin} and P_{Kep}) found by the periodograms along with their residual weighted rms and FAP. Our approach recovers all stars that exhibit long-term trends emulated by long periods and generally decreases the rms down to a few m/s.

We identify for ι Hor and HR 506 the same periods that were previously announced as planetary signals (Kürster et al., 2000, Mayor et al., 2003). For both stars we derive refined orbital solutions in the next section.

HR 3259: For HR 3259 Lovis et al. (2006) reported three Neptune-mass planets with periods (amplitudes) of 8.667 d (3.51 m/s), 31.56 d (2.66 m/s), and 197 d (2.20 m/s). We stress that our HARPS

data set is complementary to the HARPS GTO programme and that we see also excess power at these periods (Fig. 4.5). The corresponding peak heights are in the same order as suggested by the given amplitudes. Although these peaks do not reach our FAP threshold, they are compatible of the published periods. However, while 74 data points were available to Lovis et al. (2006), we have only 18 binned HARPS data points and considerable spectral leakage (aliasing). The best-fitting period of 1.1235 d listed in Table 4.4 with a FAP<1% can be shown to be an alias to 8.66 d: The one-day alias of 1.1235 d is 8.871 d ($\frac{1}{8.871} = \frac{1}{0.9972} - \frac{1}{1.1235}$, where we used the sidereal day 23h56m=0.9972 d). The 8.871 d period has a higher power in our periodogram than the nearby 8.66 d period, moreover both are related by one-year aliasing ($\frac{1}{8.66} = \frac{1}{8.871} + \frac{1}{365.2422}$).

ε Eri: In the periodogram for ε Eri (Fig. 4.6) we cannot find any evidence for the long-period planet (P=2500 d) suggested by Hatzes et al. (2000) whose orbital solution is plotted in Fig. 4.13 for comparison. ε Eri is an active star and has a stellar rotation period of 11.2 d (Fröhlich, 2007). On a short time scale of 86 min its variability is 0.88 m/s (Table 4.10), while the long term jitter estimate is 3.6 m/s (Table 4.10). Our best-fitting sine function has a period of 6.3 d, reduces the scatter from 8.6 m/s to only 7.2 m/s, and is not significant.

β Hyi: The 1.00 d period (more precisely 1.00026 d) tabulated for β Hyi is a one-day alias of a 4500 d (12.3 yr) period which the second highest peak in the periodogram ($\frac{1}{4500} \simeq \frac{1}{1} - \frac{1}{1.00026}$). We plot this long period with a grey dashed line in Fig. 4.12. This period matches that of a Jupiter analogue, while the amplitude of 7.5 m/s results in a formal minimum mass of 0.65 $M_{\rm Jup}$. Compared to the trend in the previous section the fitted LC-VLC offset is less discrepant (-6.6 m/s), but the sine fit is still not supported by the VLC data, because their scatter increases from 7.3 m/s to 8.3 m/s.

ζ^1 Ret: Even though the best-fitting sinusoidal period of P=427 d for the star ζ^1 Ret has a significance below our chosen threshold of 10^{-3} (Fig. 4.7), we display the fit (including the secular acceleration of 0.61 m/s) in Fig. 4.13. The relatively large scatter of 12.0 m/s is indicative of excess variability. Also the residuals of the sine fit have a large scatter of 8.3 m/s. Both cannot be explained only by the jitter estimate of 4.0 m/s for ζ^1 Ret which is a quite high value within our sample. Multiple planetary signals might be an explanation. More observations are needed to clarify this.

HR 8883: The period of 7.6 d found for the giant HR 8883 does only improve the HARPS rms, but not the LC and VLC rms (Table 4.11). Endl et al. (2002) found strong Ca II H&K emission in a FEROS spectrum (cf. $S_{\rm HK} = 0.492$ in Table 4.10) and mentioned the high X-ray luminosity. Hence the variations for this star might be intrinsic to the giant (rotation, solar-like oscillations).

One should finally look at the column in Table 4.4 which lists the rms after fitting a Keplerian orbit. For most of stars the rms is only a few m/s.

4.4.4 Orbital solutions

For the refinement of the orbital parameters and the error estimation we used the program GaussFit (Jefferys et al., 1988) which can solve general nonlinear fit-problems by weighted least squares and robust estimation. As initial guess we provided the parameters found with the Keplerian periodogram in the previous section.

The orbital solution for HR 2400 is given in Table 4.7. The companion has a minimum mass of $0.17 M_{\odot}$ indicating an M dwarf at a separation of 9.6 AU ($0\farcs26$). Hence, HR 2400 is a single-lined spectroscopic binary (SB1). Figure 4.17 displays the RV residuals for HR 2400 along with four other binaries that are discussed in the following.

In our analysis we recovered the planetary signal seen for ι Hor by Kürster et al. (2000). We refined the orbital parameters with our data sets and involved also the AAT (Butler et al., 2006) and CORALIE data (Naef et al., 2001) as shown in Fig. 4.8. For these two data sets the jitter estimate was added to the measurements error. Due to the activity of the star the residuals have a high scatter. The orbital parameters

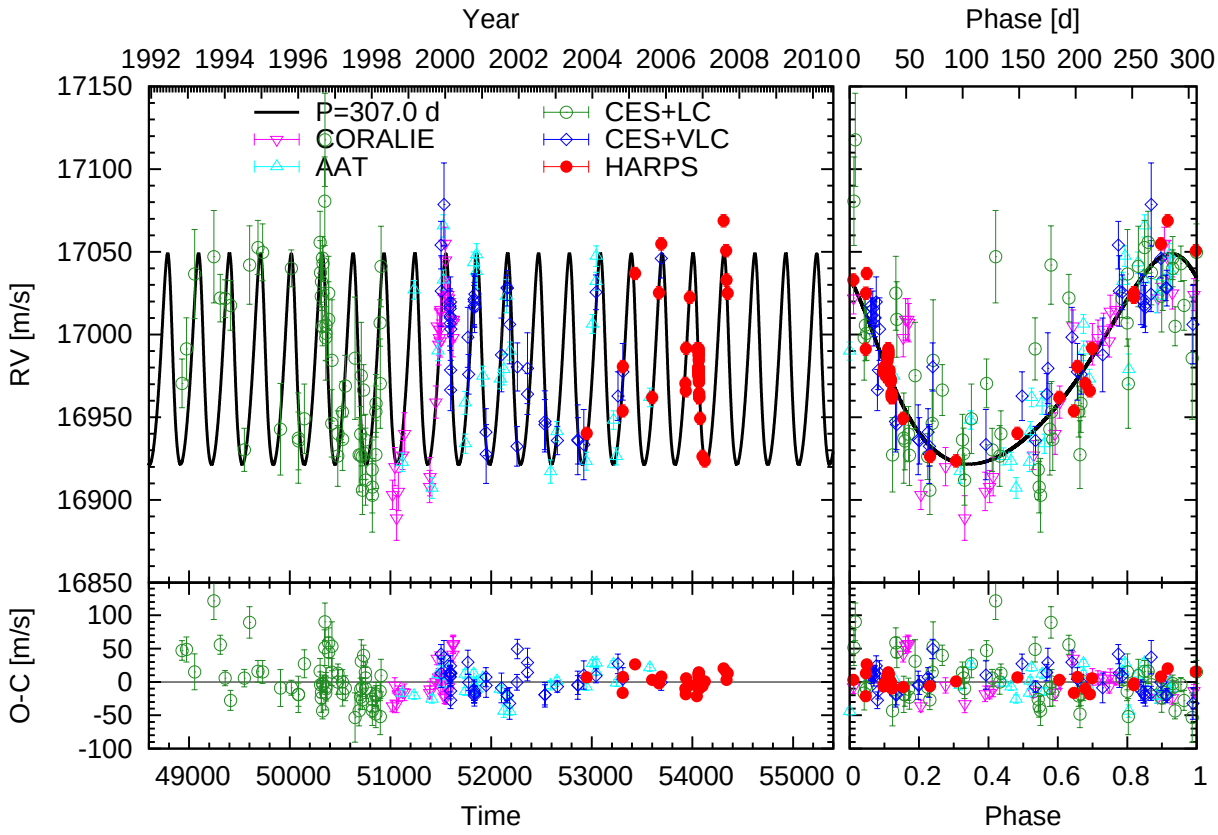

Figure 4.8: (Left) RV time series for ι Hor combined with AAT and CORALIE data. (Right) RV phase folded to the period of $P = 307$ d and the residuals (bottom).

are listed in Table 4.8. The orbital period of 307 d is different from the rotation period of ∼8 d and the magnetic activity cycle of ∼1.6 yr (Metcalfe et al., 2010) (see also Sect. 4.4.5).

Also for HR 506 do we combine our observations with AAT data (Butler et al., 2006) and CORALIE data (Mayor et al.)[5] to fit the orbit. Because more cycles have been covered, our combined solution gives a more precise period compared to the solutions given by the other authors ($P = (1003 \pm 56)$ d, $e = 0.16 \pm 0.22$ and $P = (1040 \pm 37)$ d, $e = 0.18 \pm 0.08$, respectively). For our three data sets an eccentric orbit does not fit much better (Table 4.4) and also in the combined solution the eccentricity vanished. Therefore a circular obit was fitted (e and ω fixed to zero, Table 4.9, Fig. 4.9).

For κ For, α Cen A+B and the giant HR 3677 it is not possible to give a reliable orbital solution since our measurements cover only a small piece of their orbits. We refer to Pourbaix et al. (2002) for the orbital solution for α Cen A+B with a period of 80 yr. We would just like to point out that the fitted trends in Sect. 4.4.2, although obviously not a sufficient model, can be interpreted as a mean acceleration and that the ratio of these slopes is a measure of the mass ratio $\frac{M_A}{M_B} = -\frac{\dot{RV}_A}{\dot{RV}_B} = \frac{159.2\,\mathrm{m/s/yr}}{133.9\,\mathrm{m/s/yr}} = 1.189$ which agrees with the value of $\frac{M_A}{M_B} = \frac{1.105\,M_\odot}{0.934\,M_\odot} = 1.183$ derived from Pourbaix et al. (2002).

The orbit of the companion to the giant HR 3677 is eccentric indicated by the much lower residuals when fitting a Keplerian orbit (9.2 m/s) compared to a circular orbit (33 m/s). Using the slope and Eq. (4.6) a raw estimate for the minimum companion mass is $0.68\,M_\odot$.

The RVs of κ For descend over the whole time baseline of 14 yr which indicates an orbital period longer than the estimate of 21 yr given in Endl et al. (2002). The period of 9700 d listed in Table 4.4 (26.6 yr) is not well constrained. However, again with the slope and Eq. (4.6) this period might be used to assess a minimum mass of $0.32\,M_\odot$ for the companion.

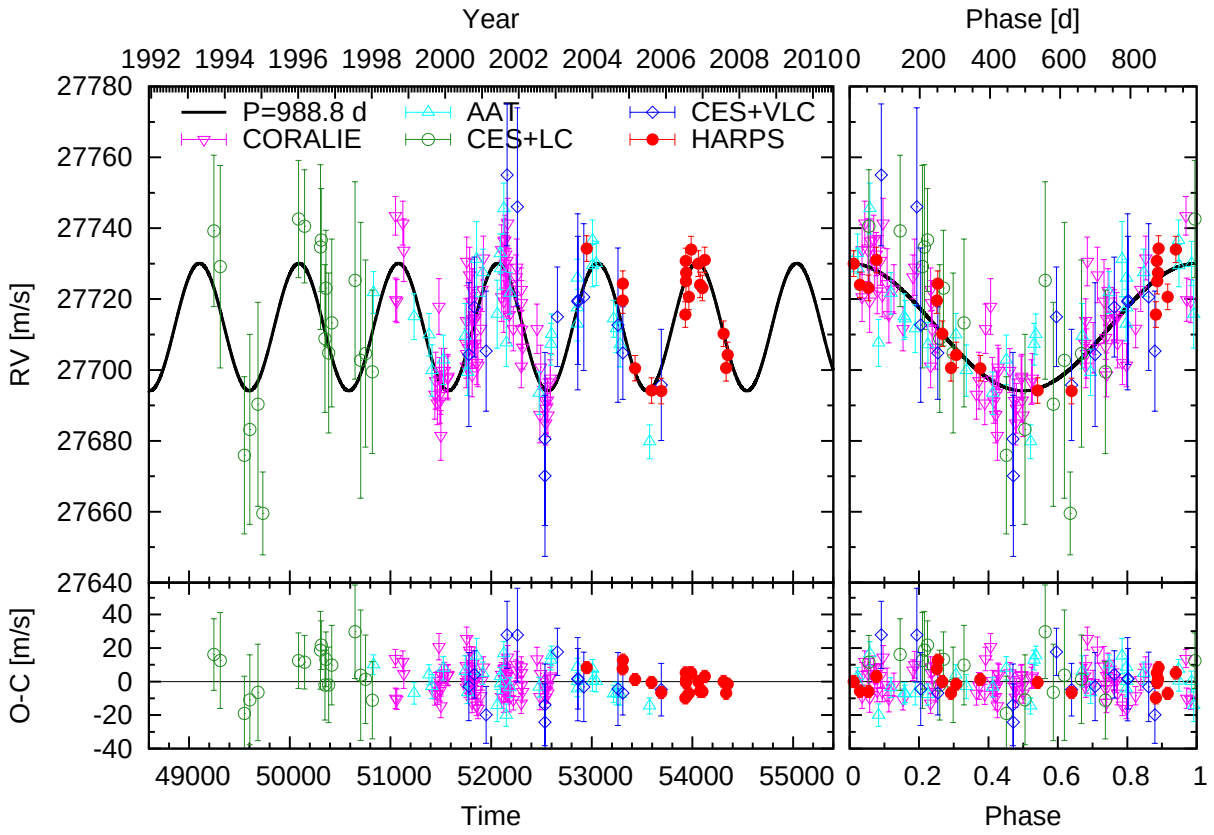

Figure 4.9: (Right) RV time series for HR 506 combined with AAT and CORALIE data. (Left) RV phase folded to the period of $P = 989$ d and the residuals (bottom).

Table 4.7: Orbital parameters for the companion to HR 2400.

Parameter		Value
P	[d]	9340 ± 557
K	[m/s]	1712 ± 83
T_0	[JD]	$2\,451\,881 \pm 16$
ω	[°]	279 ± 1
e		0.58 ± 0.01
a	[AU]	9.6 ± 1.1
$M \sin i$	[$M_\odot$]	0.17 ± 0.01
rms	[m/s]	5.07

4.4.5 Tests on the residuals of the companion hosting stars

To search for additional companions we repeated the previous tests on the residuals of the binaries and planet hosting stars. As can be seen from Table 4.4 (objects with index r) the variability is in excess only for ι Hor and α Cen B and the two giant stars which probably have an underestimated jitter, while the residual of the rest (HR 506, κ For, α For, HR 2400, α Cen A, HR 6416, HR 7703, and HR 8501) does not exhibit a significant variability.

For almost all stars we also find no significant trends. Only HR 506 has a marginal significant of trend -2.53 m/s/yr which however increases the rms of the LC data (from 17.9 m/s to 19.3 m/s, Table 4.11).

Significant periodicities in the residuals are only found for ι Hor, HR 3677, and HR 8883. As already discussed for the giants, the cause is likely intrinsic to the stars. The same seems to the case for ι Hor. The periodogram on the residuals for ι Hor (Fig. 4.10) shows power at periods of 5.7 d as well as 8 d.

Table 4.8: Orbital parameters for the planetary companion to ι Hor.

Parameter		Value
P	[d]	307.0 ± 0.3
K	[m/s]	63.6 ± 2.2
T_0	[JD]	$2\,449\,117 \pm 7$
ω	[°]	39.4 ± 6.8
e		0.20 ± 0.03
a	[AU]	0.96 ± 0.05
$M \sin i$	[$M_{\rm Jup}$]	2.41 ± 0.08
rms	[m/s]	14.0

Table 4.9: Orbital parameters for the planetary companion to HR 506.

Parameter		Value
P	[d]	988.8 ± 8.5
K	[m/s]	18.0 ± 1.0
T_0	[JD]	$2\,450\,091 \pm 24$
ω	[°]	0 (fixed)
e		0 (fixed)
a	[AU]	2.04 ± 0.24
$M \sin i$	[$M_{\rm Jup}$]	0.98 ± 0.05
rms	[m/s]	8.33

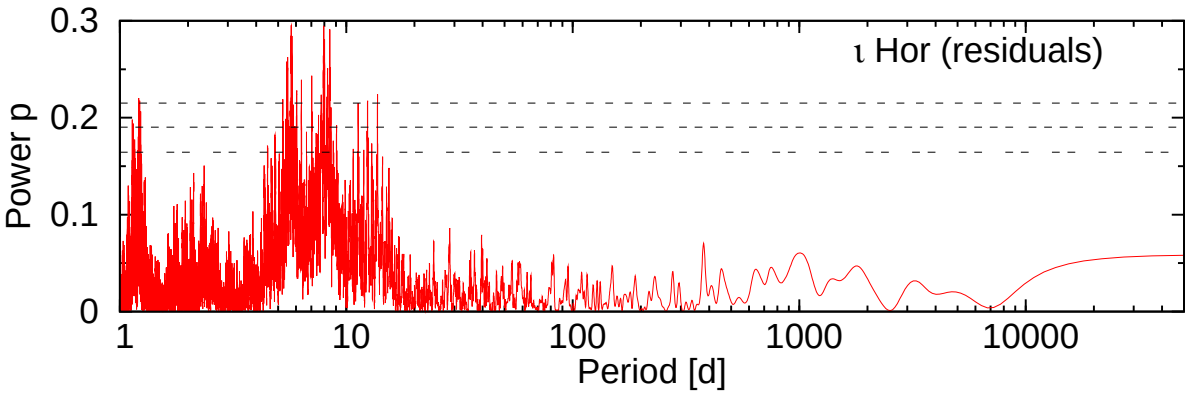

Figure 4.10: GLS periodogram on the residuals for ι Hor.

From the two peaks at 7.94 d and 8.45 d the latter coincides with periodic variations (8.5 d) found in the $S_{\rm HK}$ index by Metcalfe et al. (2010). Hence these periods are probably due to the rotation of this star.

4.4.6 Detection limits

To demonstrate the sensitivity of our survey, we have calculated for each star conservative 99.9% detection limits for circular orbits following the method outlined in Zechmeister et al. (2009). As an example, Fig. 4.11 illustrates the upper mass limit for HR 2667 (one of our most constant stars) showing that we are approximately sensitive to Jupiter analogues. Because the more precise HARPS data typically cover only 1500 d, there is a loss of sensitivity for longer periods indicated by a steep increase of the upper mass limit. The longer time baseline gained with the CES data pushes a bit the limit at longer periods.

The detection limits of the other stars have a qualitatively similar shape to that shown in Fig. 4.11

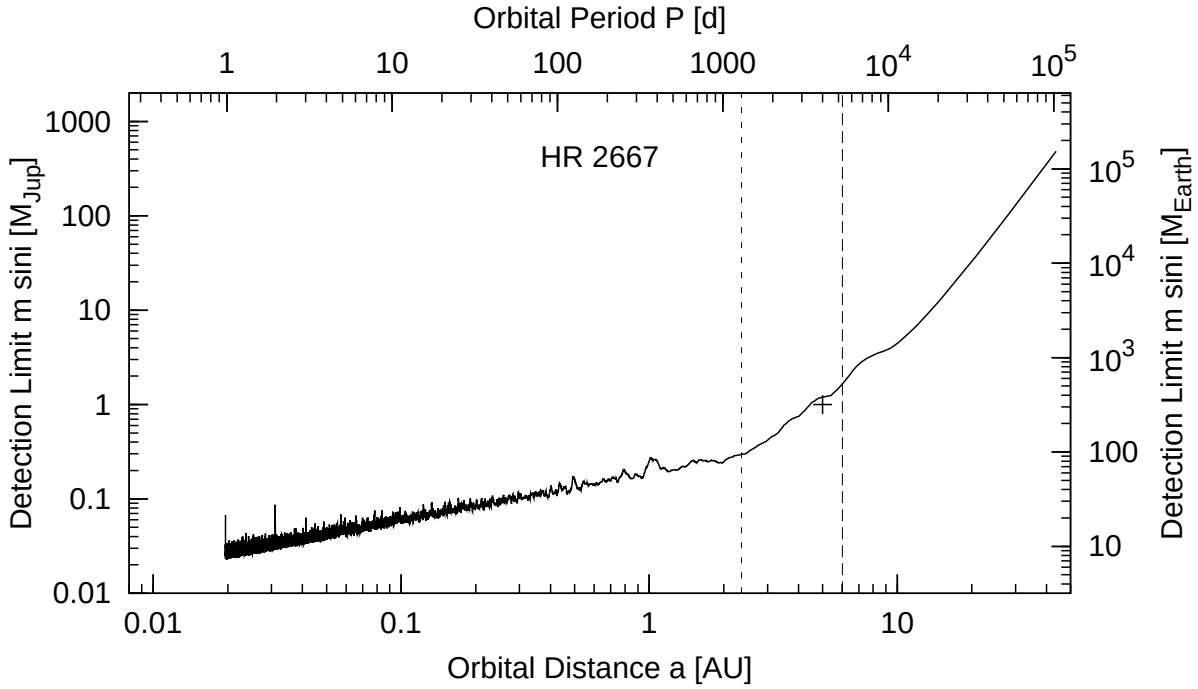

Figure 4.11: Detection limit for HR 2667. The cross marks the distance and $m \sin i$ of a Jupiter analogue for $i = 90°$. The vertical lines indicate the time baseline of the HARPS and all combined measurements, respectively.

and are available in Sect. 4.9. For one star (the residuals of HR 7703) the upper mass limit is lower than $1\,M_{\rm Jup}$ (due to the lower stellar mass of $0.7\,M_{\odot}$). For 12 stars the limit is still lower than $2\,M_{\rm Jup}$ and for 27 stars lower than $4\,M_{\rm Jup}$.

4.5 Summary and Conclusion

Our sample consists of three planet hosting stars. These planets are already known and we are able to trace their periodic RV signals allowing to confirm their reality. The planet hosting stars are ι Hor, discovered by this survey (Kürster et al., 2000), as well as HR 506 (Mayor et al.)[5] and HR 3259 (Lovis et al., 2006) which even has a system of three planets. However, we have no clear additional planet detection in our sample, while some promising or controversial cases like β Hyi, ζ^1 Ret, or ε Eri call for follow-up observations.

Compared to our previous results in Endl et al. (2002), we confirm that:

- κ For, HR 2400, and HR 3677 are SB1 spectroscopic binaries with long periods.
- α For, HR 6416, and HR 8501 exhibits trends consistent with their wide stellar companions.
- ε Ind A has a steady long-term trend still explicable by a planetary companion.

Moreover, we see a trend for HR 7703 and GJ 570 A which can also be explained by the known wide stellar companion listed in Table 4.6. However, the RV trend of 7 m/s/yr reported for β Hyi is only 2.1 m/s/yr in the combined data set and is not seen in the VLC data. We cannot confirm a linear drift reported by Eggenberger et al. (2007) for α Men and the planet ε Eri b reported by Hatzes et al. (2000).

Our upper mass limits demonstrate that we are sensitive to Jupiter-mass planets up to 5 AU, i.e. Jupiter analogues. Although our sample size is too small to provide a meaningful number for the occurrence rate of Jupiters, the two Jupiter-mass planets in our sample imply that our results are in agreement with the planet frequency of other much larger surveys. E.g. from the ELODIE survey Naef et al. (2005)

estimated a fraction of $7.5 \pm 1.5\%$ for the stars hosting giant planets with periods smaller than 10 yr, while Cumming et al. (2008) derived a frequency of $12 \pm 1.6\%$ from the Keck survey.

The main reason for the limited VLC precision of $\sim$9 m/s is the short wavelength coverage of only 39 Å. Useful iodine lines cover a total wavelength range of 1000 Å. If this 25 time larger range could have been used, the extrapolated VLC precision would be 5 times higher, i.e. 1.8 m/s.

The outperforming precision of the active stabilised HARPS spectrograph is mostly due to the large wavelength coverage. The higher resolution of the CES+VLC is not necessarily an advantage because the stellar lines are nearly resolved already at the lower resolution of HARPS, i.e. they become broader but not sharper and therefore provide not much more RV information[16]. Nevertheless the CES data are valuable for extending the time baseline to 15 years.

The problem of combining long-term precision RV data from different instruments complicates the analysis. We could derive the zero point offset between LC and VLC only with a limited precision which leads to a loss of sensitivity for trends and long periods. However, this problem can occur in long-term surveys quite frequently as spectrographs receive upgrades or survey projects are transferred to new instruments. Long-term access to the same instrument is therefore important.

While the RV method probes the inner region of the stellar environment, the outer regions can be explored for planets with direct imaging. Since both methods complement each other, their combination leads to a more complete picture about the existence and nature of planets around stars. An example is ε Ind A, where despite the high imaging sensitivity by Janson et al. (2009) the non-detection put constraints to the companion which induces the observed RV trend of 2.5 m/s/yr. Hence the results and detection limits from our survey can be valuable for other campaigns which target these bright stars.

Some of our nearby and bright stars are also the subject of projects searching and studying surrounding debris disks. Structures in these disks permit conclusions about the presence of outer planets. E.g. the HERSCHEL satellite has resolved exo-Kuiper belts around ζ^2 Ret (Eiroa et al., 2010) and around HR 506 (q^1 Eri, Liseau et al., 2010). In the case of the RV planet-hosting star HR 506, the structure of a ring at 35-40 AU provides a hint for another planet. Similarly, the structure of the known debris disk of ε Eri suggests an outer planet (Quillen & Thorndike, 2002). But then for HR 8501 that has an RV trend likely due to its wide stellar companion, Eiroa et al. (2010) exclude a cold debris disk.

[16]The thermal line broadening of a line with frequency f is given by

$$\frac{\Delta f}{f} = \sqrt{8 \ln 2 \frac{kT}{mc^2}} = \frac{1}{1.4 \cdot 10^6} \sqrt{\frac{T/\mathrm{K}}{m/\mathrm{amu}}}$$

and depends on the temperature T and the atomic/molecular mass m. Therefore resolving hydrogen lines ($m_\mathrm{H} = 1$ amu) in a solar-like star ($T = 6000$ K) requires a resolution of $R = \frac{\lambda}{\Delta\lambda} \approx 18\,000$ and for iron lines ($m_\mathrm{Fe} = 56$ amu) $R = 135\,000$. A higher resolution as provided by the CES leads to an oversampling or stretching of the lines but does not resolve new lines or sharper features which would improve the RV measurements. Contrariwise, for iodine gas ($T = 323$ K, $m_{\mathrm{I}_2} = 154$ amu) the thermal line broadening effect corresponds to $R = 2\,400\,000$.

4.6 Plots of all radial velocity time series

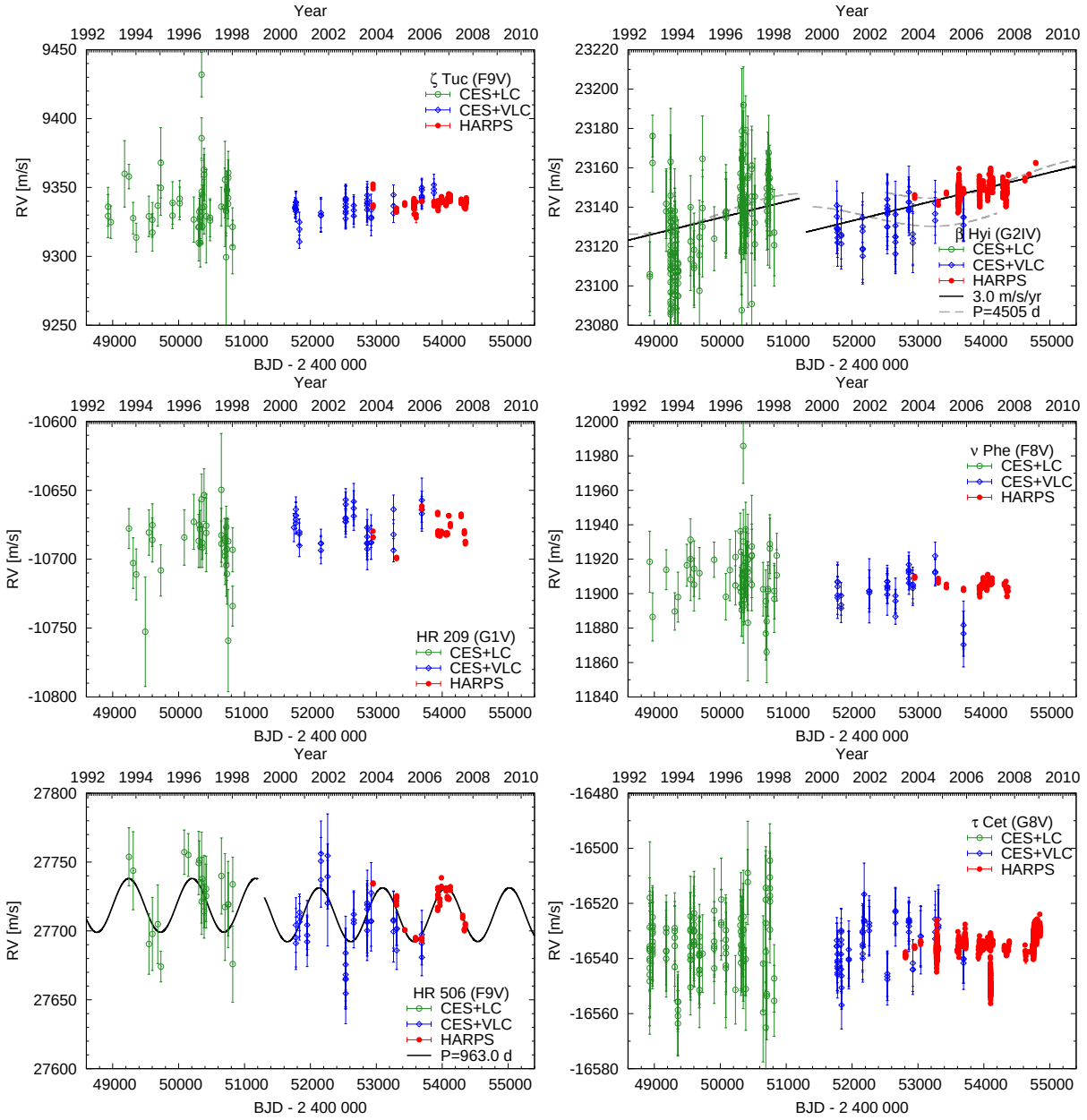

Figure 4.12: Radial velocity time series (unbinned data). The error bars depict the internal measurement errors ΔRV_i, i.e. not including jitter. LC (green open circles) and VLC (blue open diamonds) data are displayed with their measured offsets. Jumps in the curves indicates the difference between the measured (Sect. 4.3.5) and fitted (Sect. 4.4) offset. HARPS data are in red filled circles. The solid black lines indicate significant models, while gray dashed lines illustrate less or non-significant alternative models. All models include secular acceleration. Model curves are shown for β Hyi (trend and long-period sinusoid, see text for discussion), and HR 506 (sinusoid).

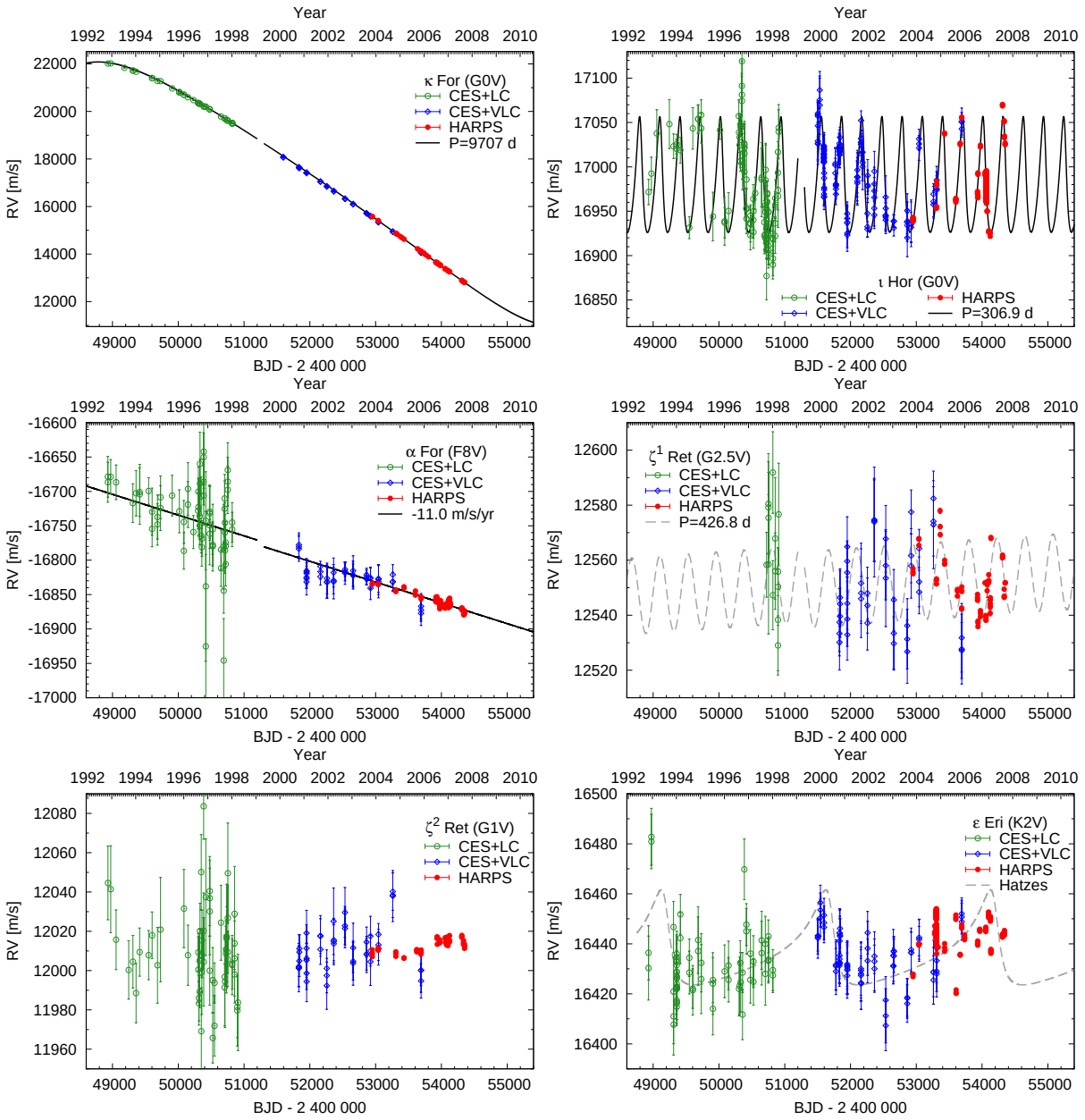

Figure 4.13: Radial velocities. Continuation of Fig. 4.12. Model curves are shown for κ For (Keplerian), ι Hor (Keplerian), α For (trend), and ζ^1 Ret (sinusoid). The Keplerian orbit for ε Eri taken from Hatzes et al. (2000) is not significant in this work.

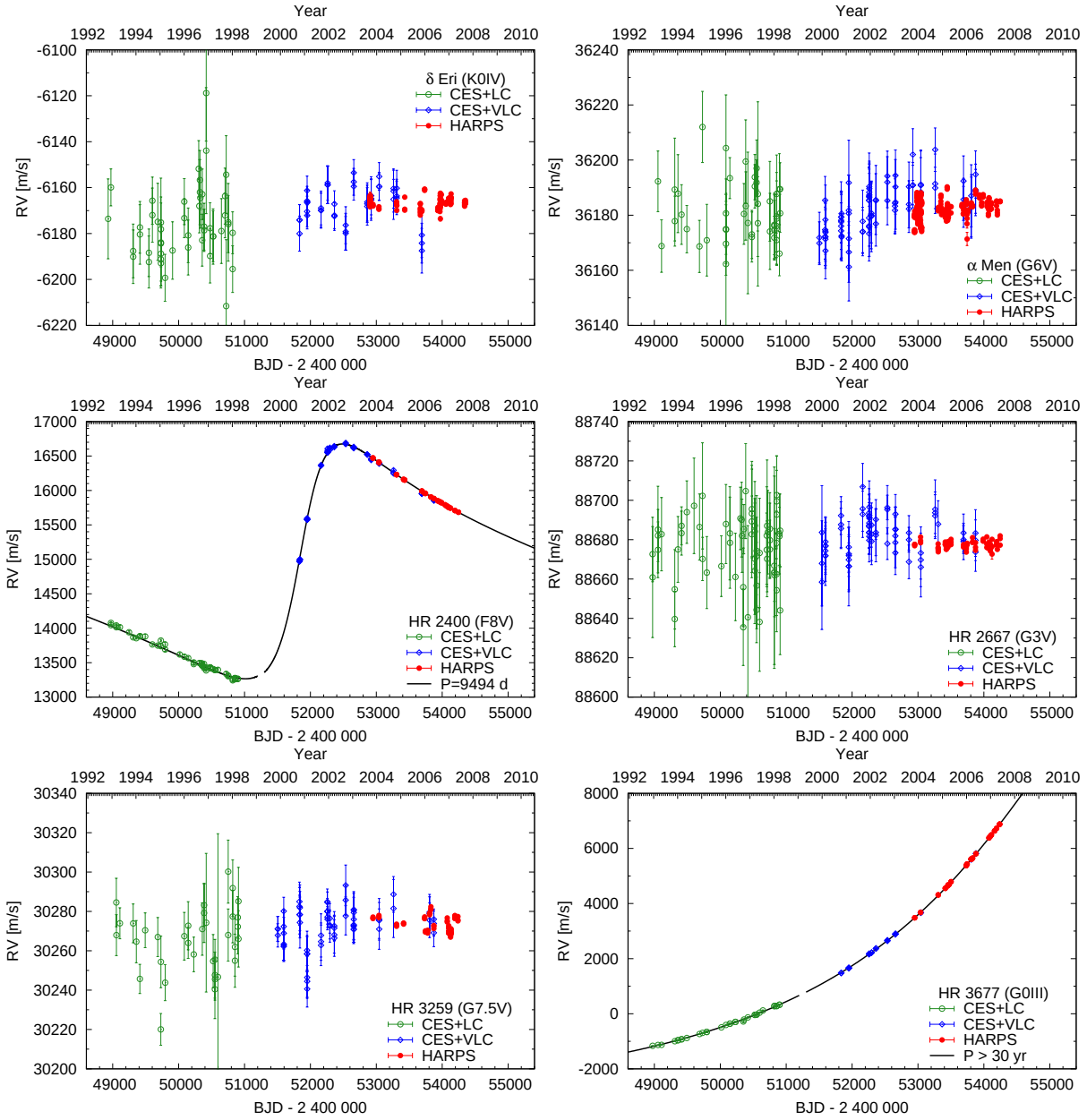

Figure 4.14: Radial velocities. Continuation of Figs. 4.12 and 4.13. Model curves are shown for HR 2400 (Keplerian) and HR 3677 (Keplerian).

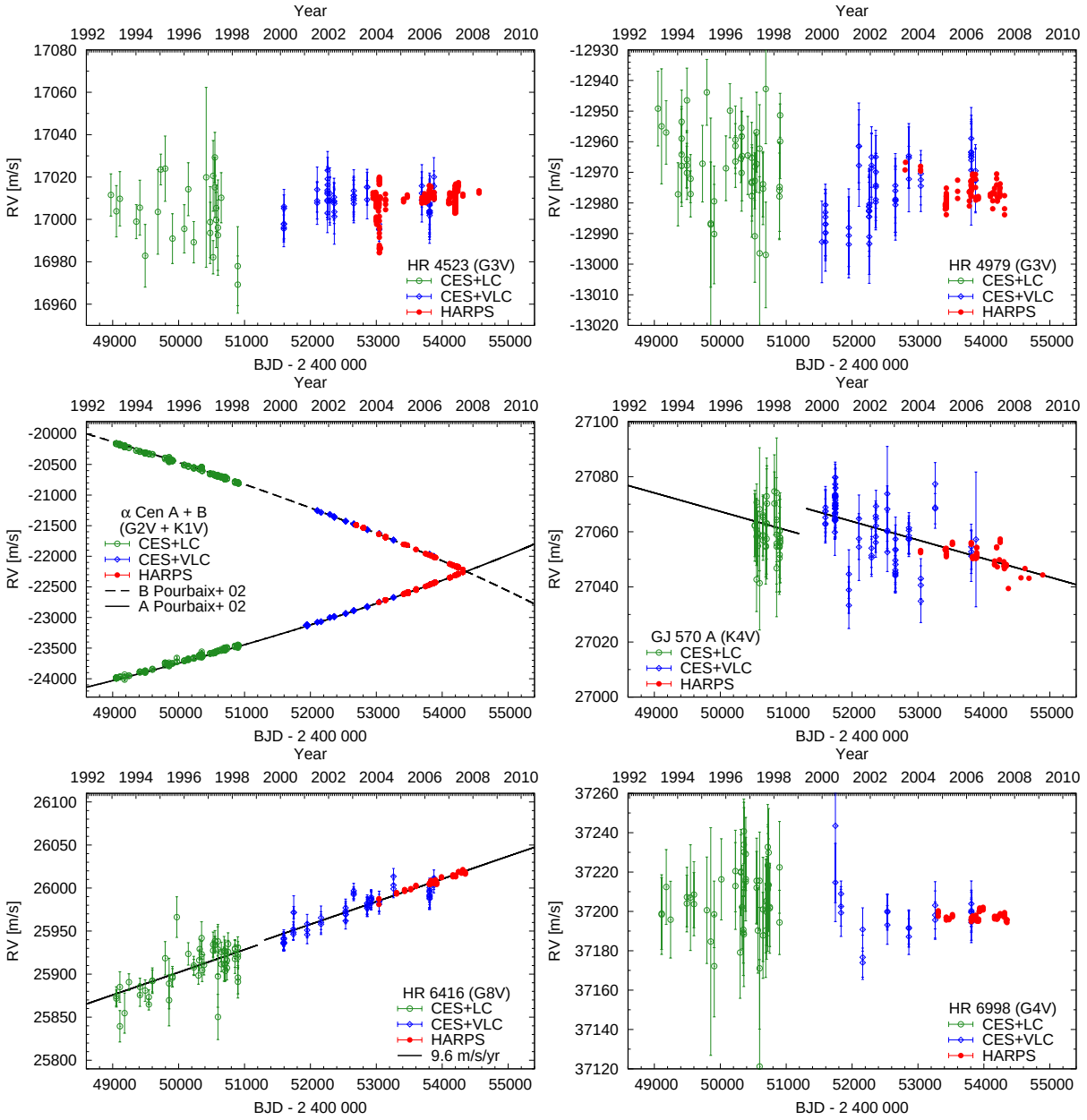

Figure 4.15: Radial velocities. Continuation of Figs. 4.12–4.14. Model curves are shown for α Cen A and α Cen B (Keplerian orbit from Pourbaix et al. 2002), GJ 570 A (trend), and HR 6416 (trend).

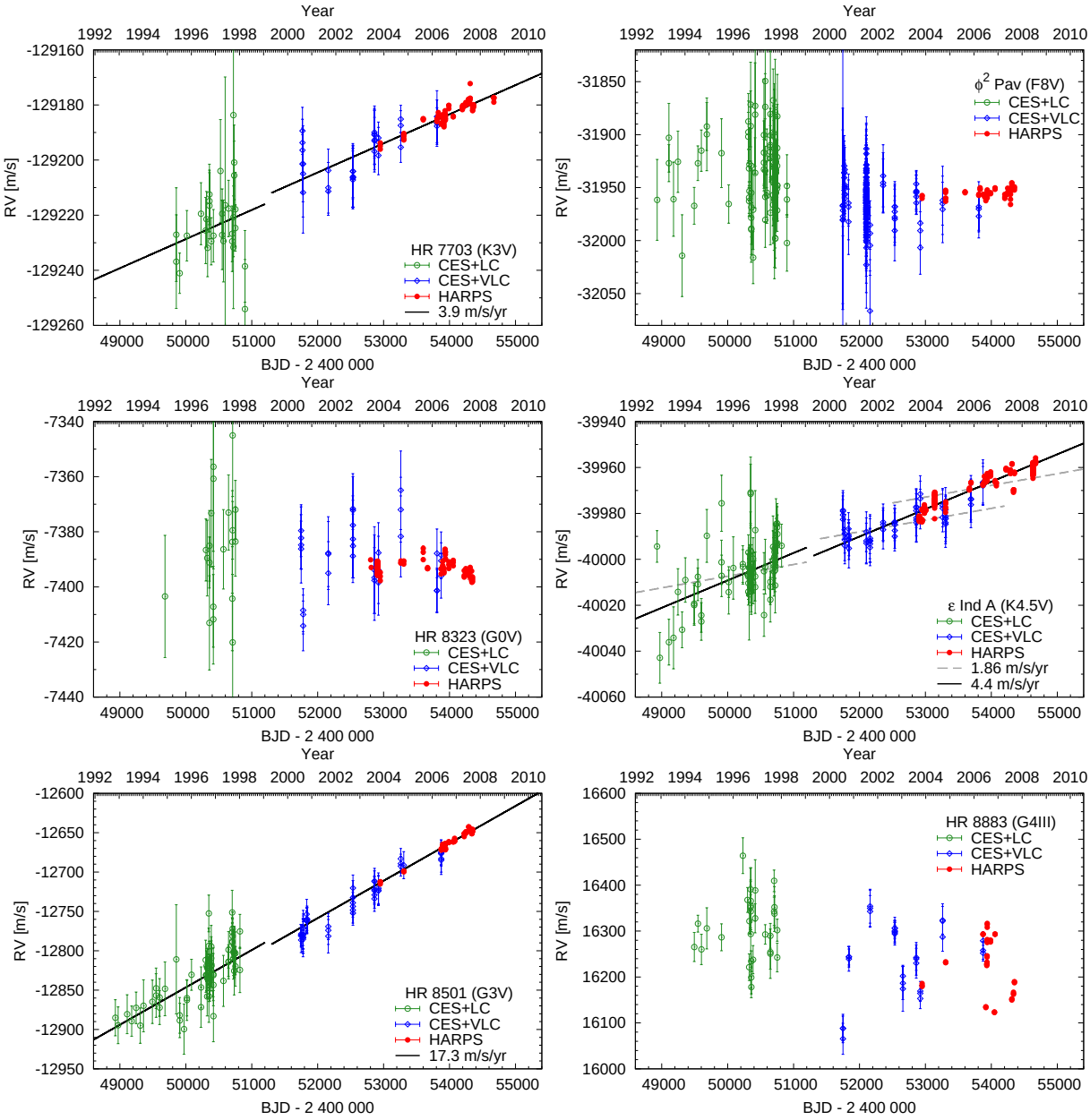

Figure 4.16: Radial velocities. Continuation of Figs. 4.12–4.15. Model curves are shown for HR 7703 (trend), ε Ind A (constant, i.e. only secular acceleration of 1.86 m/s/yr, and trend), and HR 8501 (trend).

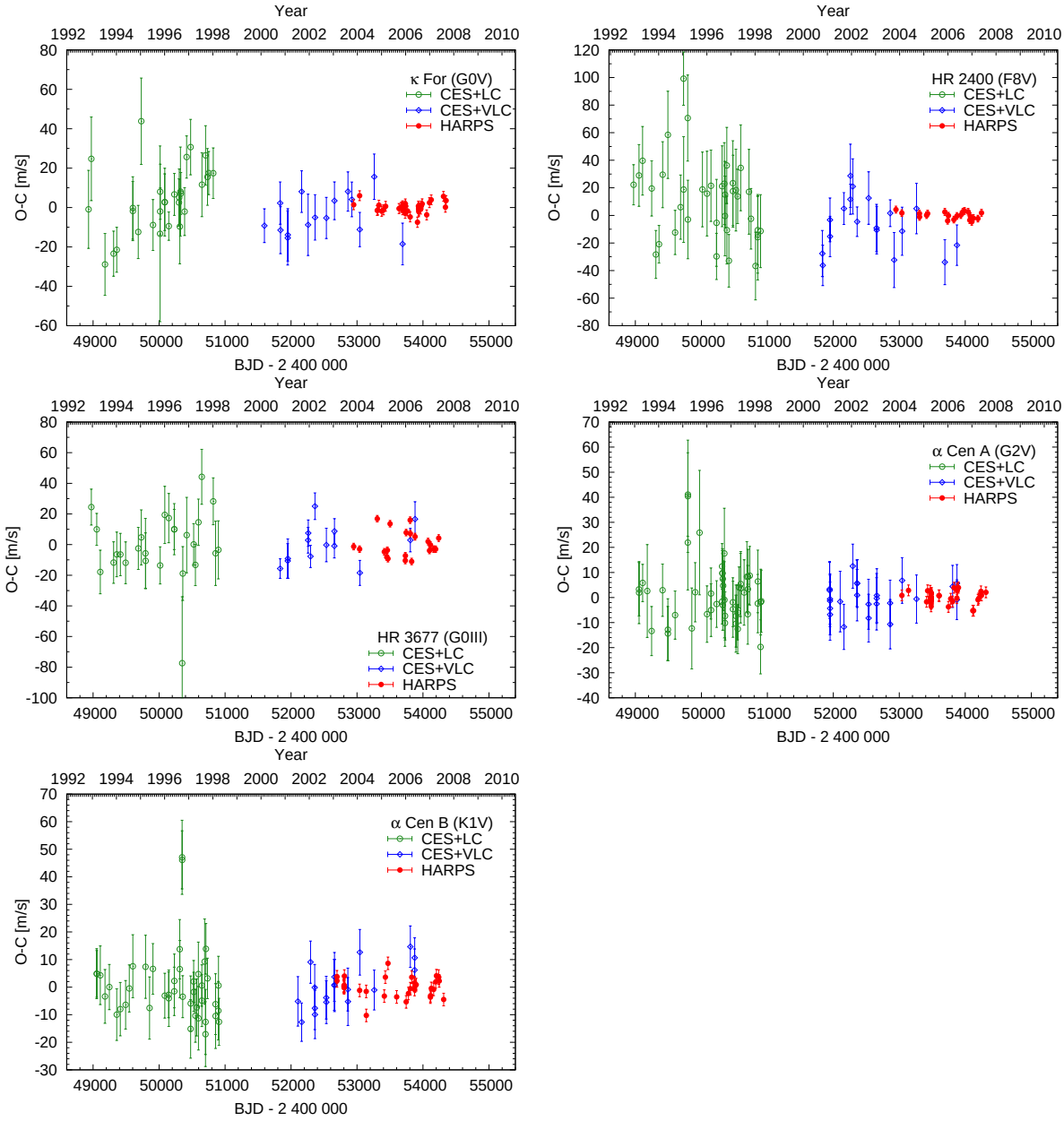

Figure 4.17: Residual RVs (binned) for the spectroscopic binaries.

4.7 Accompanying Tables

Table 4.10: Jitter estimation. The time scales τ were used for the computation of σ_{jit} (which may not cover the real jitter time scales in all cases). The jitter in the last column was derived from B-V (Perryman et al., 1997) and the mean activity index S_{HK} ([H] Henry et al. 1996, [G] Gray et al. 2006, [W] Wright et al. 2004) as described in Isaacson & Fischer (2010).

Star	σ_{jit} [m/s]	τ [min]	B-V [mag]	S_{HK}	σ_{jit} [m/s]
ζ Tuc	1.73	38.3	0.576	0.179 [H]	2.89
β Hyi	2.33	109.9	0.618	0.158 [H]	2.48
HR 209	0.69	9.9	0.635	0.279 [H]	4.57
ν Phe	1.11	8.9	0.571	0.161 [H]	2.58
HR 506	1.07	7.8	0.551	0.217 [G]	3.58
τ Cet	1.12	90.8	0.727	0.171 [H]	2.19
κ For	1.36	19.2	0.608	0.158 [G]	2.49
ι Hor	1.39	112.5	0.561	0.225 [H]	3.71
α For	2.25	17.1	0.543	0.162 [G]	2.62
ζ^1 Ret	0.74	11.1	0.641	0.245 [H]	3.97
ζ^2 Ret	0.87	9.3	0.600	0.196 [H]	3.15
ε Eri	0.88	86.5	0.881	0.483 [H]	3.59
δ Eri	1.28	21.3	0.915	0.129 [H]	1.87
α Men	2.63	67.4	0.714	0.175 [H]	2.21
HR 2400	2.05	17.5	0.534	0.146 [G]	2.35
HR 2667	0.98	11.8	0.624	0.169 [H]	2.66
HR 3259	0.67	22.0	0.754	0.167 [G]	2.17
HR 3677	0.83	13.1	0.827	-	2.10
HR 4523	3.84	70.2	0.664	0.168 [H]	2.61
HR 4979	1.74	40.5	0.693	0.153 [H]	2.34
α Cen A	2.17	111.6	0.710	0.162 [H]	2.15
α Cen B	0.79	90.5	0.900	0.209 [H]	2.27
GJ 570 A	0.61	21.3	1.024	0.709 [H]	1.60
HR 6416	0.69	38.4	0.764	0.179 [H]	2.23
HR 6998	0.61	20.5	0.673	0.181 [H]	2.84
HR 7703	0.66	12.6	0.868	0.180 [H]	2.18
ϕ^2 Pav	1.45	7.0	0.544	0.177 [G]	2.88
HR 8323	0.87	35.3	0.601	0.192 [H]	3.09
ε Ind A	0.73	55.6	1.056	0.668 [H]	1.60
HR 8501	0.94	9.2	0.614	0.181 [H]	2.88
HR 8883	1.48	7.6	0.817	0.492 [W]	3.69

Table 4.11: Residual rms detailed for each instrument resulting from the joint analysis for fitting a constant, slope, sinusoid, and Keplerian orbit.

Star	$rms_{constant}$ [m/s]			rms_{slope} [m/s]		
	LC	VLC	HARPS	LC	VLC	HARPS
ζ Tuc	17.88	7.30	2.66	17.88	7.54	2.61
β Hyi	19.01	7.37	3.91	19.11	9.45	2.92
HR 209	15.80	9.82	8.69	15.71	9.75	8.41
ν Phe	15.78	9.72	3.12	15.84	9.94	2.92
HR 506	29.87	18.96	13.08	29.95	17.67	13.05
HR 506_r	17.92	14.25	5.56	19.32	13.46	4.45
τ Cet	10.93	7.71	3.37	11.00	7.56	3.03
τ Cet[13]	10.93	7.71	2.47	10.96	7.85	2.40
κ For	867.88	1329.45	674.70	247.93	62.38	21.61
κ For_r	15.44	9.55	2.66	15.17	9.53	2.66
ι Hor	50.50	36.89	27.72	51.18	37.33	27.62
ι Hor_r	30.17	18.73	8.47	29.09	18.89	8.46
α For	48.76	27.08	11.32	31.67	12.17	2.93
α For_r	30.83	11.97	2.97	30.84	11.96	2.97
ζ^1 Ret	14.80	14.48	11.35	13.69	16.28	10.13
ζ^2 Ret	19.78	9.63	2.83	20.04	9.56	2.42
ε Eri	13.61	9.88	7.29	13.68	10.00	7.24
δ Eri	12.44	7.24	2.03	12.44	7.17	2.01
α Men	9.84	7.68	2.56	9.91	6.61	2.43
HR 2400	672.81	745.01	224.69	804.82	898.48	119.96
HR 2400_r	30.30	16.46	2.47	29.79	16.02	2.32
HR 2667	13.28	6.38	1.44	13.28	6.38	1.44
HR 3259	16.23	8.30	3.95	16.31	8.53	3.80
HR 3677	795.89	1354.55	963.87	1055.50	368.63	149.46
HR 3677_r	16.19	12.12	8.20	16.17	12.05	8.20
HR 4523	13.56	6.07	4.35	13.92	5.96	4.21
HR 4979	11.50	8.86	4.03	10.91	10.88	3.40
α Cen A	159.66	247.40	112.48	43.95	15.92	6.87
α Cen A_r	9.46	5.81	2.07	9.46	5.82	2.07
α Cen B	204.73	264.57	248.44	54.71	16.69	8.83
α Cen B_r	10.78	7.91	3.49	10.77	7.97	3.49
GJ 570 A	5.51	9.93	4.87	5.75	8.10	3.21
HR 6416	23.10	24.35	8.69	13.45	9.69	1.68
HR 6416_r	13.14	9.26	1.56	13.14	9.24	1.56
HR 6998	13.84	9.91	1.79	13.87	9.67	1.80
HR 7703	10.03	7.88	4.24	8.59	4.86	1.73
HR 7703_r	8.53	5.06	1.67	8.53	5.06	1.67
ϕ^2 Pav	30.76	21.10	3.71	30.78	21.19	3.68
HR 8323	10.76	10.64	2.94	10.81	10.81	2.82
ε Ind A	10.42	4.97	5.06	10.04	4.48	3.02
HR 8501	42.80	46.91	17.28	21.18	9.70	2.73
HR 8501_r	21.39	9.06	2.69	21.34	9.07	2.69
HR 8883	64.92	73.35	60.06	63.36	72.14	59.70
HR 8883_r	67.39	66.80	26.53	67.38	66.97	26.52

Table 4.12: Continuation of Table 4.11

Star	rms_{sine} [m/s]			rms_{Kep} [m/s]		
	LC	VLC	HARPS	LC	VLC	HARPS
ζ Tuc	16.91	7.03	1.99	11.61	7.24	1.90
β Hyi	19.59	8.29	2.56	18.76	7.99	2.30
HR 209	14.07	8.39	5.81	16.46	7.24	3.56
ν Phe	14.66	8.40	2.42	12.87	8.78	2.36
HR 506	18.34	14.83	5.56	18.04	15.11	5.37
HR 506_r	16.63	13.97	3.78	15.67	12.18	3.20
τ Cet	10.93	8.36	2.51	10.68	7.79	2.00
τ Cet[13]	10.67	7.45	2.21	11.61	7.24	1.90
κ For	30.29	33.23	3.79	15.62	10.01	2.66
κ For_r	13.97	8.67	2.28	14.42	8.32	1.87
ι Hor	32.29	18.15	12.62	30.17	18.73	8.47
ι Hor_r	29.47	18.87	5.81	28.74	16.94	5.73
α For	30.86	12.01	2.97	31.34	11.40	2.76
α For_r	30.71	10.57	1.79	30.89	11.16	1.43
ζ^1 Ret	12.92	13.92	7.62	13.72	14.94	5.74
ζ^2 Ret	18.65	8.85	2.27	14.73	8.73	2.48
ε Eri	14.08	9.30	4.93	12.54	10.28	3.67
δ Eri	11.56	6.83	1.39	10.69	5.98	1.00
α Men	9.65	7.40	2.21	9.95	7.32	1.84
HR 2400	311.69	408.94	74.33	30.94	17.30	2.47
HR 2400_r	29.66	16.46	1.75	22.05	15.37	1.92
HR 2667	12.62	6.33	0.95	11.49	4.83	1.29
HR 3259	15.67	7.61	2.13	11.15	7.40	2.48
HR 3677	139.32	79.54	18.33	16.28	12.17	8.18
HR 3677_r	16.37	13.92	4.76	15.18	12.57	3.92
HR 4523	13.41	6.31	3.79	14.12	5.18	2.28
HR 4979	11.88	8.72	2.64	9.13	9.05	2.27
α Cen A	10.52	7.48	2.35	9.46	5.81	2.07
α Cen A_r	9.33	5.75	1.60	9.22	6.00	1.40
α Cen B	11.03	9.09	3.45	10.78	7.93	3.49
α Cen B_r	10.33	6.65	2.75	7.34	6.84	2.83
GJ 570 A	5.54	8.49	3.15	5.61	8.53	2.84
HR 6416	13.15	9.27	1.56	13.14	9.27	1.56
HR 6416_r	12.41	8.86	1.25	10.96	6.16	1.58
HR 6998	13.48	8.83	1.10	12.12	8.96	0.99
HR 7703	8.53	5.06	1.67	8.32	4.78	1.59
HR 7703_r	8.23	5.45	1.15	7.82	2.18	1.04
ϕ^2 Pav	29.65	20.74	2.56	27.06	20.35	2.62
HR 8323	10.58	10.51	1.90	9.90	5.71	1.89
ε Ind A	10.14	4.49	2.85	8.64	7.45	2.80
HR 8501	21.47	9.35	2.69	20.78	10.02	2.61
HR 8501_r	20.99	8.23	1.69	18.21	8.91	1.97
HR 8883	68.14	68.69	26.53	61.16	70.16	20.58
HR 8883_r	66.10	74.01	11.18	69.07	68.86	6.88

Table 4.13: Offsets $c_{\mathrm{VLC}} - c_{\mathrm{LC}}$ [m/s] in the fits.

Star	const	slope	sine	Kep
ζ Tuc	-4.95	-3.78	-5.09	-2.22
β Hyi	-9.17	-17.98	-6.63	-9.02
HR 209	5.83	-0.30	4.77	3.29
ν Phe	-6.51	-1.81	-6.29	-5.92
HR 506	-8.98	-4.94	-6.95	-7.59
τ Cet	-0.73	-5.15	-1.33	0.04
κ For	-3006.87	249.64	-26.57	-13.57
ι Hor	8.63	4.45	-3.60	0.28
α For	-40.30	-6.73	-2.00	-4.77
ζ^1 Ret	-6.09	2.37	-2.09	-6.66
ζ^2 Ret	1.03	-2.07	0.62	3.15
ε Eri	3.04	1.57	1.76	3.12
δ Eri	6.41	4.39	6.59	5.91
α Men	0.49	-3.62	0.68	-0.45
HR 2400	1425.06	1830.99	527.64	-16.08
HR 2667	-0.37	-0.24	-0.29	-0.03
HR 3259	8.42	10.78	7.06	5.79
HR 3677	2317.93	-1896.05	-106.35	-6.59
HR 4523	0.26	-3.26	1.34	0.91
HR 4979	-11.44	-3.97	-12.21	-11.29
α Cen A	660.88	-100.47	-11.33	0.65
α Cen B	-861.32	120.52	12.94	4.47
GJ 570 A	0.01	9.86	5.10	1.06
HR 6416	49.09	3.07	-2.96	-2.87
HR 6998	-6.47	-4.51	-5.61	-6.31
HR 7703	19.57	3.04	-0.35	1.01
ϕ^2 Pav	-12.28	-12.50	-12.68	-9.96
HR 8323	-3.14	-1.43	-2.65	-1.40
ε Ind A	9.17	-4.80	15.31	9.91
HR 8501	53.79	-6.89	-4.81	-3.26
HR 8883	-13.20	-3.05	-12.08	-17.15

4.8 Plots of all periodograms

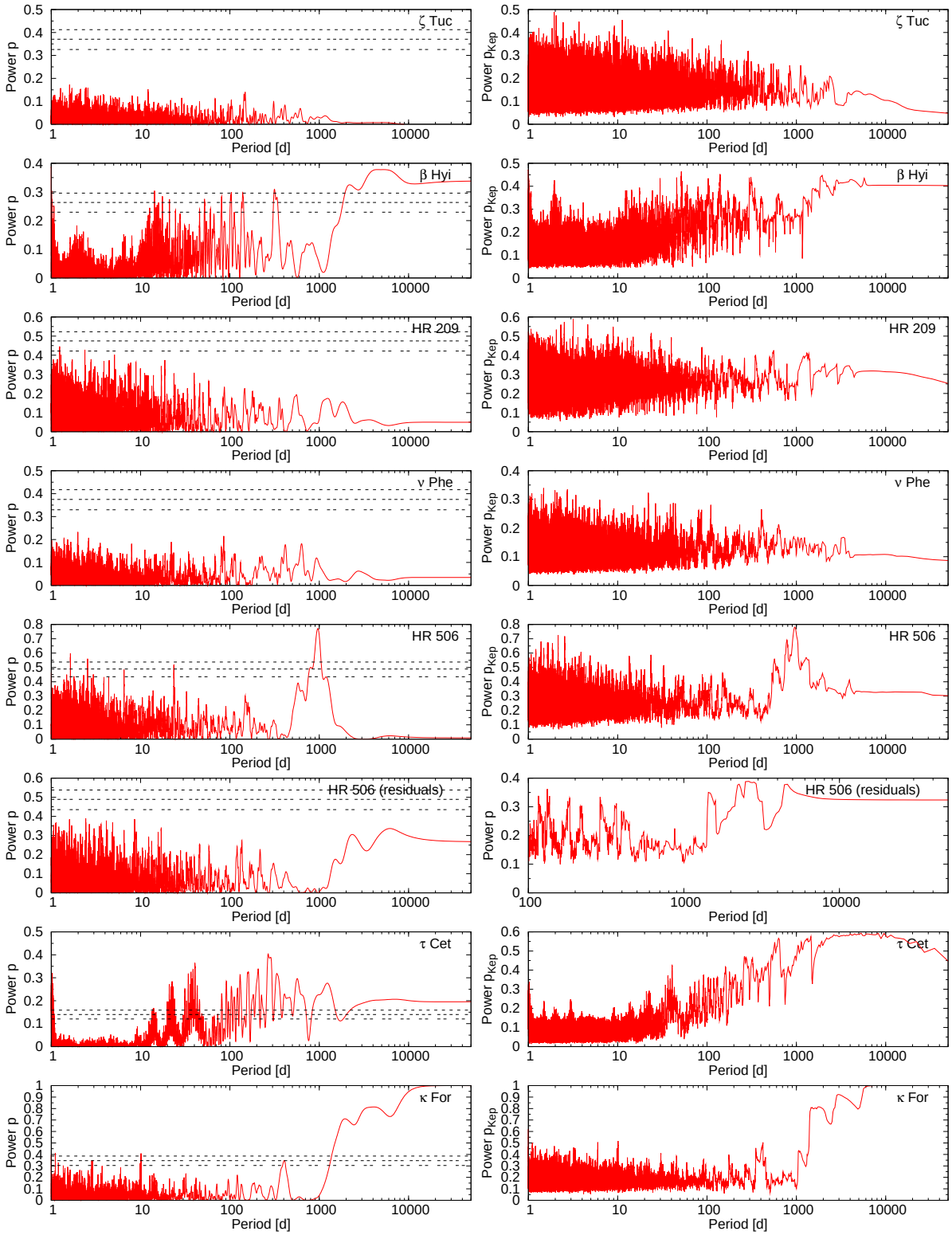

Figure 4.18: GLS and Keplerian periodograms.

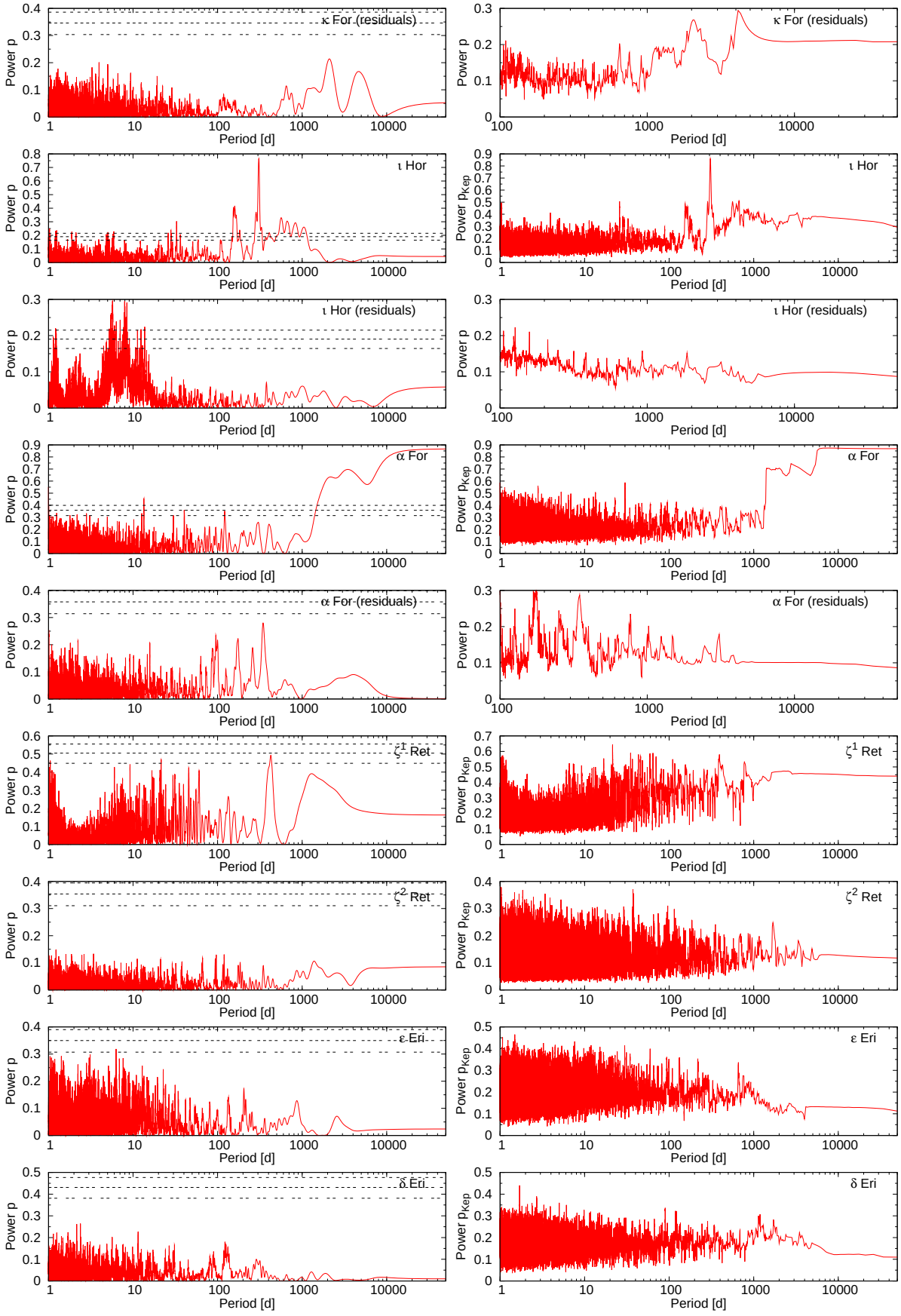

Figure 4.19: GLS and Keplerian periodograms. Continuation of Fig. 4.18.

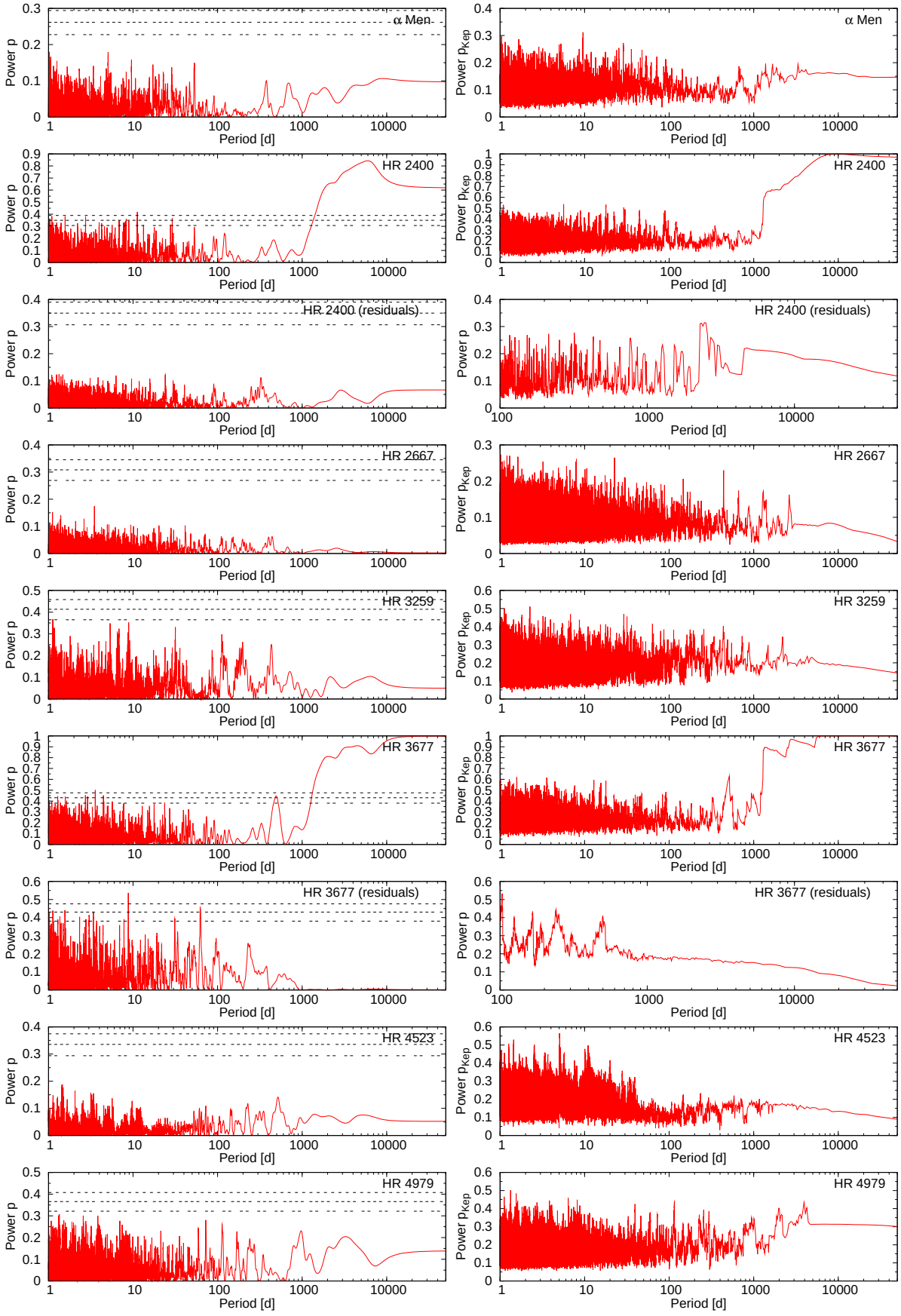

Figure 4.20: GLS and Keplerian periodgrams. Continuation of Figs. 4.18 and 4.19.

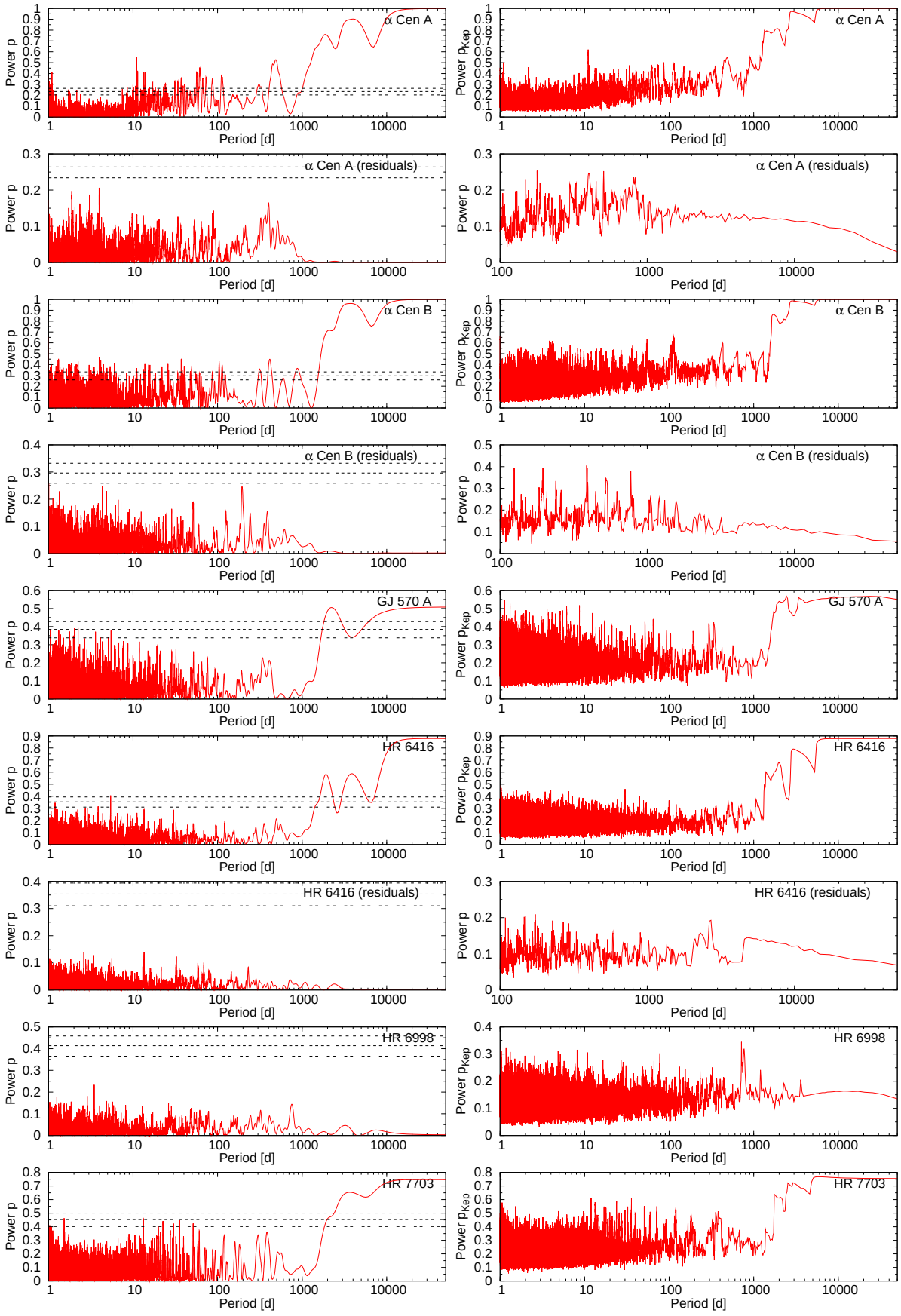

Figure 4.21: GLS and Keplerian periodgrams. Continuation of Figs. 4.18–4.20.

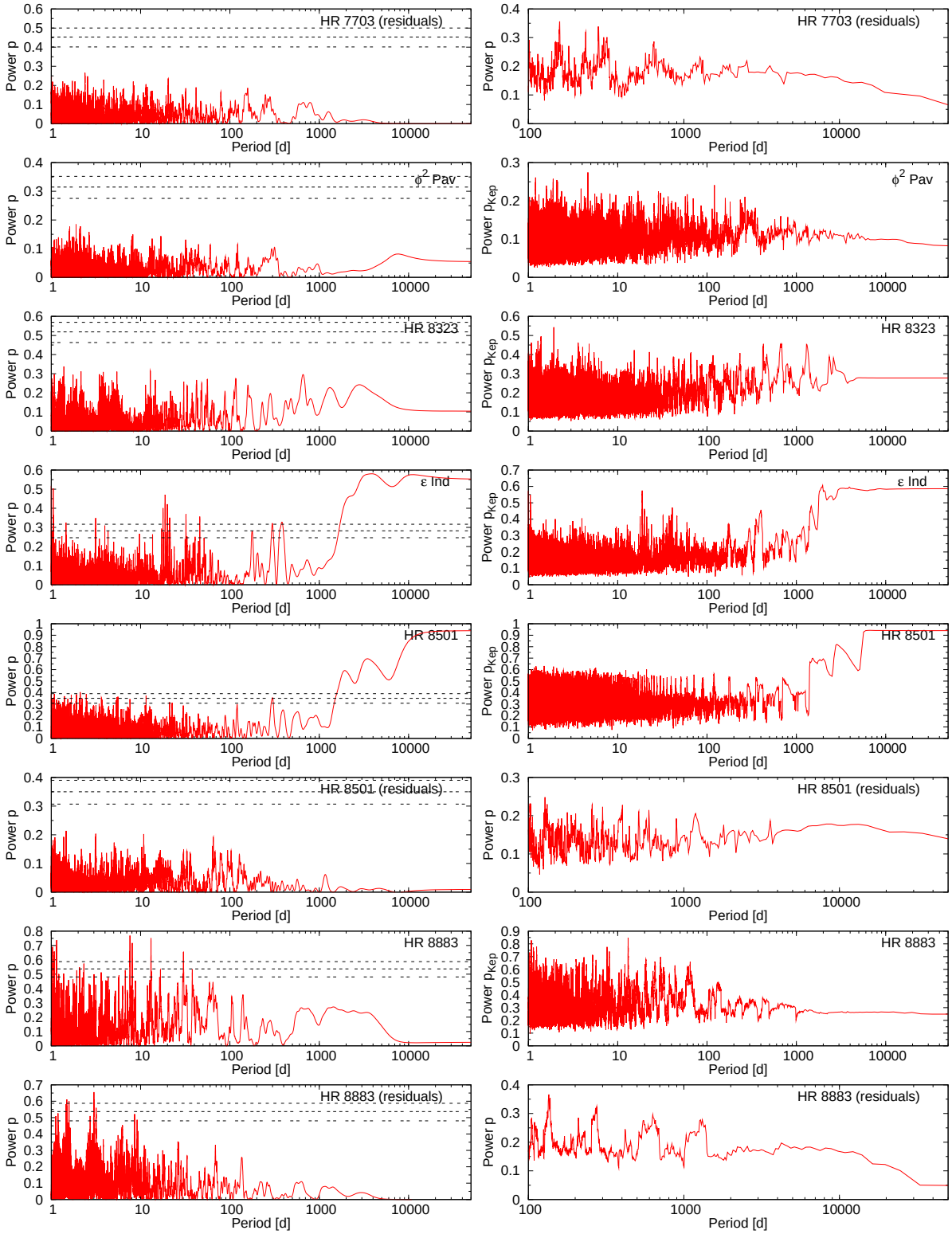

Figure 4.22: GLS and Keplerian periodgrams. Continuation of Figs. 4.18–4.21.

4.9 Plots of all detection limits

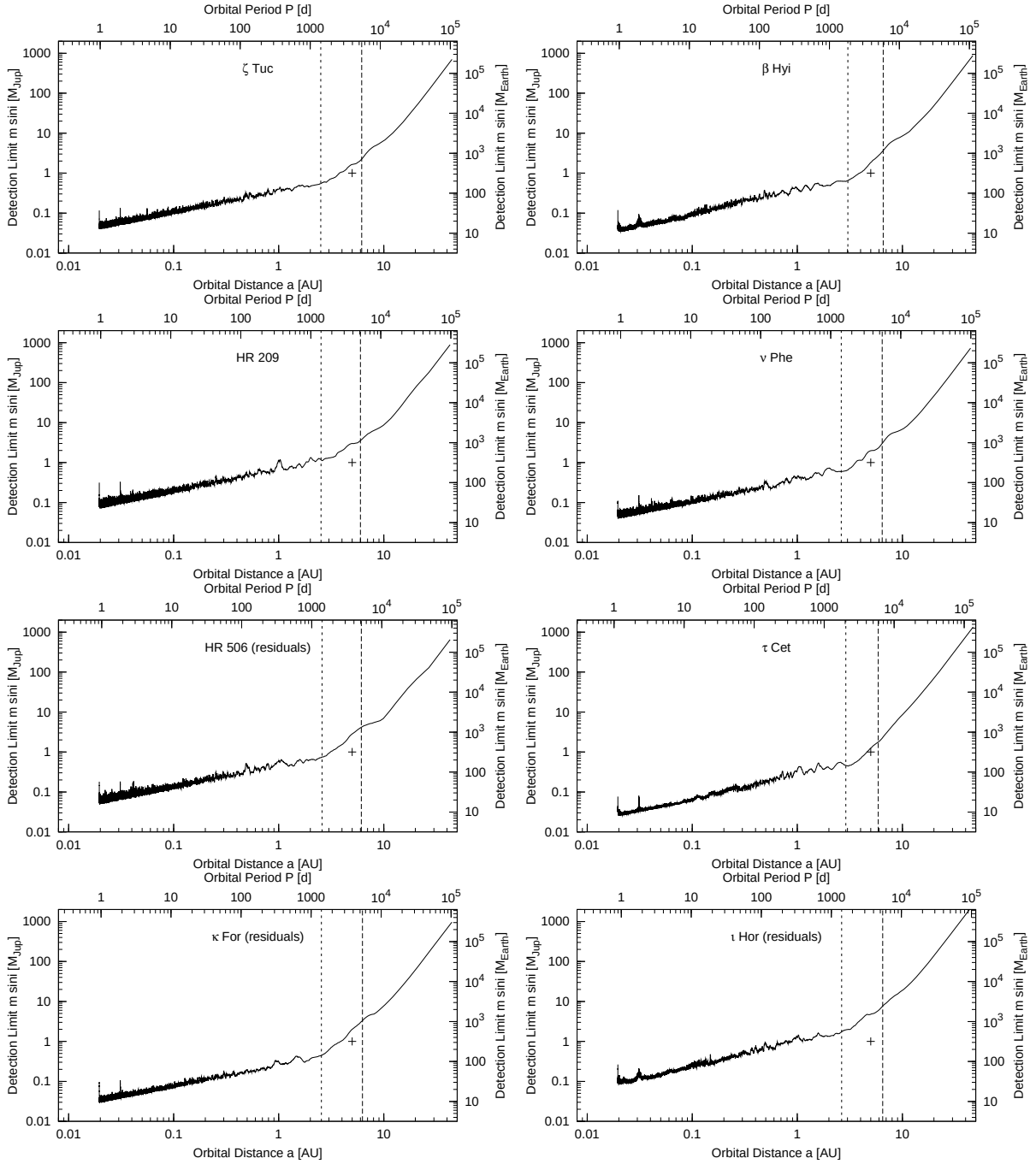

Figure 4.23: Upper mass limits.

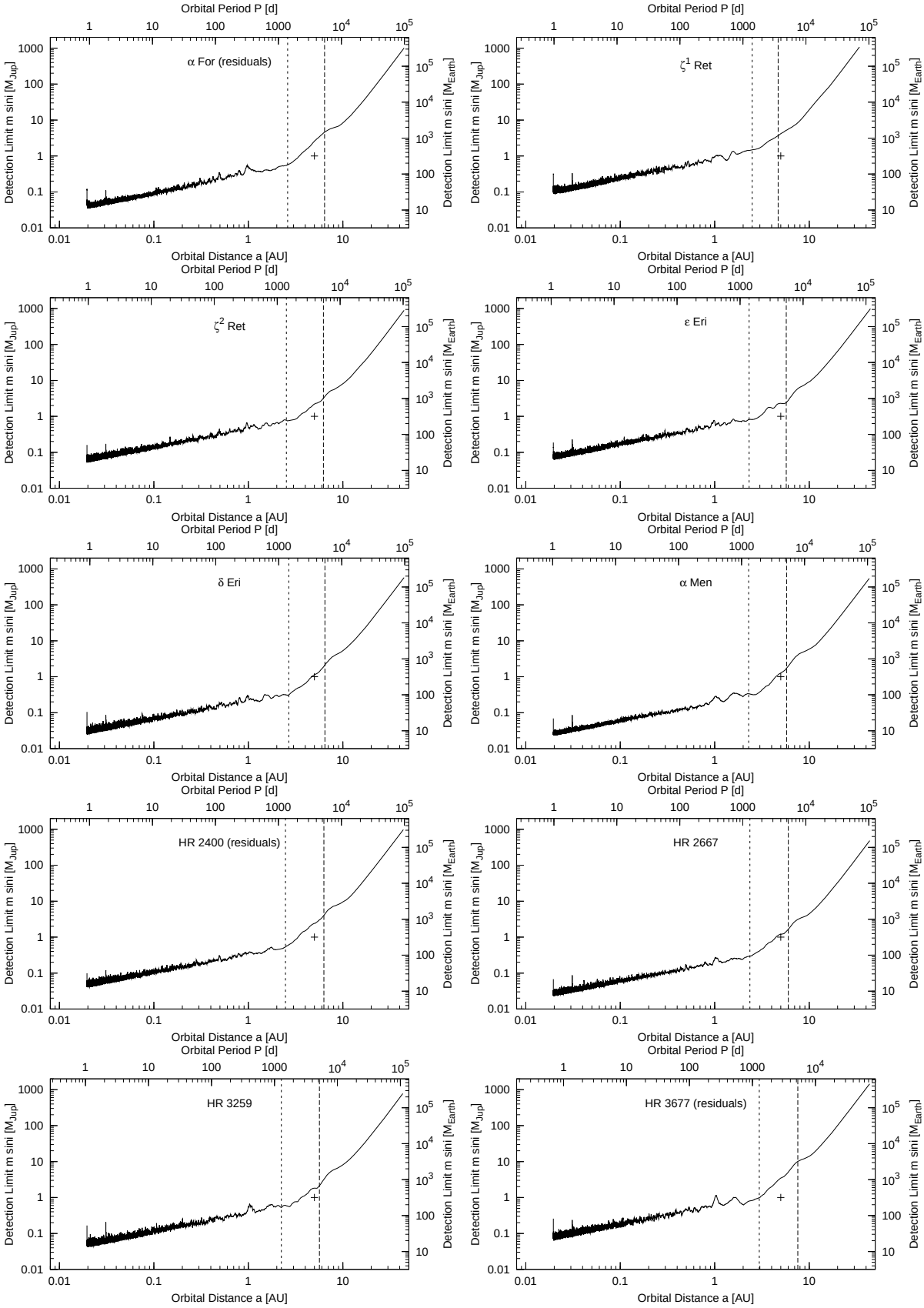

Figure 4.24: Upper mass limits. Continuation of Fig. 4.23.

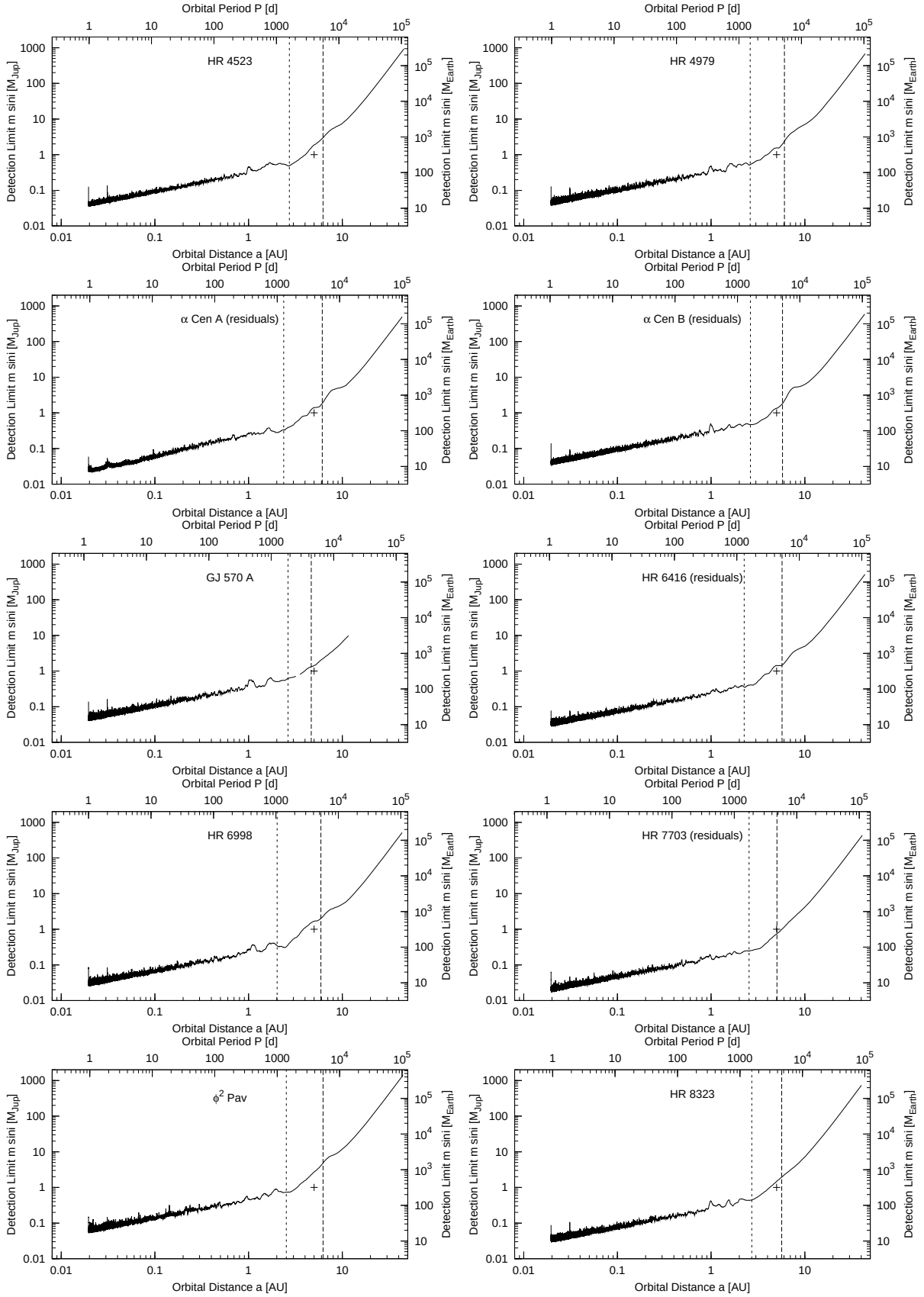

Figure 4.25: Upper mass limits. Continuation of Figs. 4.23 and 4.24.

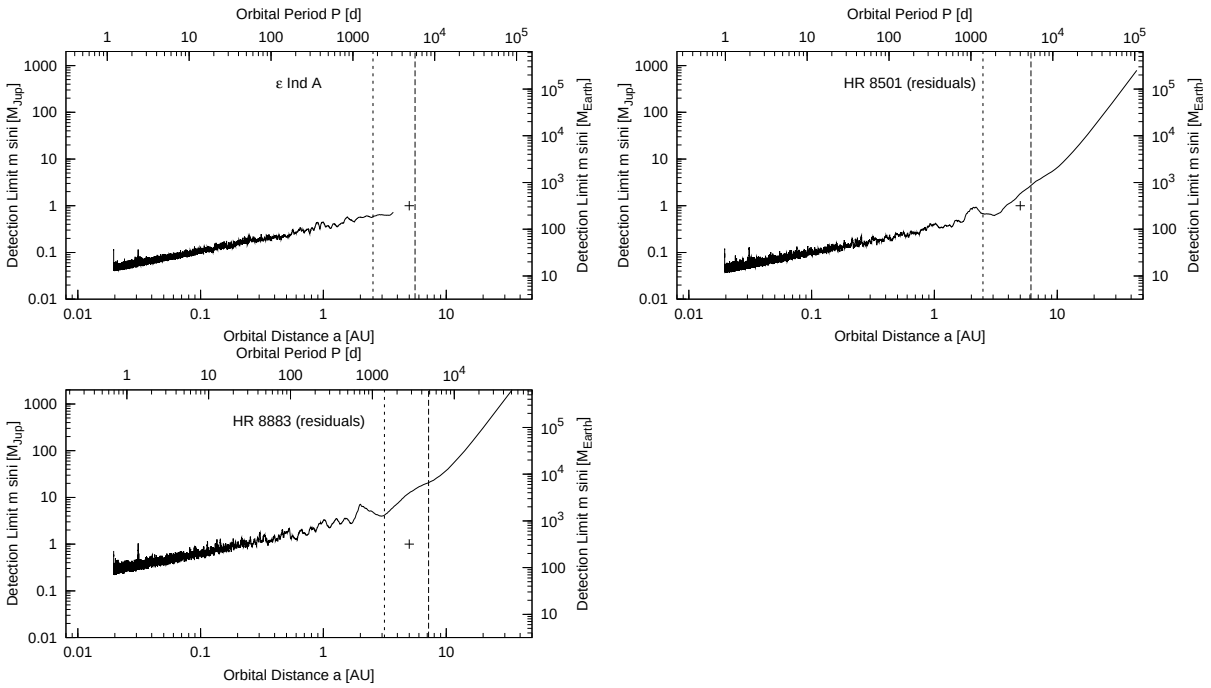

Figure 4.26: Upper mass limits. Continuation of Figs. 4.23–4.25.

Chapter 5

Summarising Conclusions

We have generalised the Lomb-Scargle periodogram which is an often used period search algorithm. The GLS was very helpful in this work. We hope to have established a better standard in the period analysis and that the GLS finds favour with the whole astronomical community, since it can be also applied to problems other than planet search. Indeed, it has been already employed in different fields of astronomy, e.g. to study photometric variable stars, for asteroseismology, or to study X-ray sources. Even an archaeologist showed interest to analyse palaeoclimatic data with the GLS.

We have analysed and discussed two long-term RV surveys. Unfortunately, we have no new planet discovery in our two samples of 40 M dwarfs and 30 solar-like stars. For both surveys we do have the appropriate RV precision, and our conservative detection limits demonstrate the feasibility to discover habitable terrestrial planets around M dwarfs and Jupiter analogues around solar-like stars with our instruments.

The reason for the non-detections in our UVES sample is likely the low frequency of Jupiter-mass planets around M dwarfs. This was theoretically predicted and seems to be supported by our survey and by other ongoing ones (e.g. HARPS, HIRES). However, a comparison of the observational results is difficult, since most of the other groups have not yet published their non-detections, but only the discoveries from their surveys. Our sample alone would make only low number statistics possible. Similarly, the incidental discovery of a close-in brown dwarf (GJ 1046 B, Kürster et al. 2008) in our UVES sample is not representative for the frequency of brown dwarfs orbiting around M dwarfs. Indeed, this interesting object is so far the only close-in brown dwarf found around a single M dwarf[1].

Our constant stars can serve as a reference for other surveys. E.g. Bean et al. (2010b) demonstrated for Barnard's star and Proxima Centauri a precision of 5 m/s which is remarkable for near-infrared RV measurements and the used instrumental setup (CRIRES, small wavelength coverage). But there seems to be potential for improvements, since we know from our survey that these stars are constant to 3 m/s. Our precision is also fairly comparable with that presented for several M dwarfs from the HIRES sample (Butler et al., 2009). Recent publications using HARPS and HIRES data show that even a precision of < 2 m/s is feasible for quiet M dwarfs with current instruments (Mayor et al., 2009a; Vogt et al., 2010).

In our second sample of 30 solar-like stars there are two Jupiter-mass planets which were already known (Kürster et al., 2000, Mayor et al.) whereas the planet ι Hor b was dicovered in the early stage of this survey. The corresponding detection rate of $\sim$7% agrees well with an estimate of 10% for the frequency of Jupiter-mass planet in the regime of 2–2000 d from the Keck planet search (Cumming et al., 2008). Taken into account possible long-period candidates, such as ε Ind A, our results do not seem to contradict the extrapolated frequency of 17-20% for gas giants with in 20 AU (Cumming et al., 2008). We cannot draw conclusions about the frequency of low mass planets around solar-like star, since our data sets are not sufficient to detect those planets. Albeit we found traces of the three known Neptun-mass planet around HR 3259 (Lovis et al., 2006) in our periodgram, their detections was yet not significant.

A successful planet search with radial velocities requires of course high RV precision, a large sample,

[1] There are only three more close-in brown dwarfs to M dwarfs which however are located in binary systems (Santos et al., 2002; Irwin et al., 2010; Johnson et al., 2010).

sufficient observation time, and long-term access to the instruments.

5.1 Outlook

The precision RV method is nowadays a standard technique and will remain an important work horse in the future. It probes the stellar environment out to a few AU which is complementary to the direct imaging as well as the transit methods. With the growing time baseline of several large surveys, more long-period planets should appear in the exoplanet list and follow-up observations of planet-hosting stars should reveal more planetary systems. These discoveries will be reserved for groups with privileged access to dedicated instruments.

Among the ESO facilities only three spectrographs (HARPS, UVES, and CRIRES) are able to achieve a high RV precision. Out of these, only HARPS is a dedicated planet searcher, but the current scheduling policy (at least three consecutive nights) makes access to this instrument difficult for most of the astronomers. Therefore, the CARMENES spectrograph (Quirrenbach et al., 2010) for the Calar Alto 3.5 m telescope is an important facility for the Max Planck Institute for Astronomy (MPIA) to keep competitive in the field of precision RV planet search. CARMENES is designed as a high-resolution spectrograph for near-infrared and optical RV measurements aiming at a 1 m/s precision. As for our UVES survey, the goal of CARMENES is to search for terrestrial planets in the habitable zones of M dwarfs. Given the large amount of dedicated observing time (180 nights per year over 5 years), CARMENES can monitor a large sample (300 M dwarfs) with a considerable number of data points (70 per star). With the experience from our UVES survey, we find that the concept of CARMENES is well shaped.

Since the CARMENES sample is much larger than our UVES sample, we can expect several detections and a meaningful estimate for the planet frequency around M dwarfs. Since it becomes evident that the frequency of Jupiter-mass planets around M dwarfs is low, the CARMENES survey will result in many non-detections. Our analysis method of Chapter 3 and 4 might then be adapted for these as well.

In the following, we highlight some aspects which are interesting for the further development of the RV method.

5.1.1 Precision RV measurements in the near-infrared

There is a current trend to observe stars with late spectral types, like M dwarfs, in the infrared and near-infrared (NIR). The simple reason is that they are much brighter in this wavelength region than in the optical. Therefore, surveys for these stars can be carried out more efficiently with higher S/N and/or shorter exposures. Another benefit of the NIR is the lower influence of stellar activity onto the RVs (Reiners et al., 2010; Barnes et al., 2010). However, the handling of the numerous telluric lines is complex.

Different methods for wavelength calibration have been investigated. The naturally present telluric lines are variable to several tens of m/s with the atmospheric conditions. However, a precision of 5 m/s appears achievable with careful monitoring of the atmospheric conditions and sophisticated modelling of telluric lines (Figueira et al., 2010; Seifahrt et al., 2010). Other approaches are the Uranium-Neon lamp (Ramsey et al., 2008, 2010), which has many more lines compared to the ThAr lamp, or a gas cell filled with ammonia (Bean et al., 2010b) or gas mixtures (Valdivielso et al., 2010), as an analogue to the iodine cell.

Moreover, NIR-RV may also help to confirm or disprove optical RV planet candidates. Since the geometric reflex motion of a star does not depend on the wavelength, the measured RV amplitude should be the same in all wavelength regions, if the cause is a planet. In this context, K giants are interesting targets, since their long-period RV variations are mostly explained by planet candidates while their long rotation periods or non-radial pulsations (Hatzes & Cochran, 1999; Hekker et al., 2006) are excluded as a cause.

When observing in the NIR, we investigate molecular lines, i.e the cooler, outer parts of the stellar envelope, while in the visual region the deeper regions of the stellar atmosphere are probed through metal

Table 5.1: Comparison of the calibration sources: ThAr emission lamp, iodine gas absorption cell, Fabry Perot etalon, and Laser frequency comb (from Murphy et al., 2007)[2].

Calibration lines	ThAr	I_2 cell	Etalon	Comb
From fundamental physics	Yes	Yes	No	Yes
Individually unresolved	Mostly	Yes	Possibly	Yes
Resolved from each other	No	No	Possibly	Possibly
Uniformly spaced	No	No	Yes	Yes
Cover optical range	Yes	No	Yes	Possibly
Uniform strength	No	No	Possibly	Possibly
Long-term stability	No	Yes	No	Yes
Maintain object S/N	Yes	No	Yes	Yes
Exchangeable	Yes	Yes	Possibly	Yes
Easy to use	Yes	Yes	Possibly	Possibly
Reasonably low cost	Yes	Yes	Yes	Possibly

lines. Hence, by measuring Doppler shifts in the visual and NIR we may learn more about the processes in stellar atmospheres.

5.1.2 New calibration sources

In the future, it is important to improve the wavelength calibration for high RV precision instruments. As mentioned in Sects. 1.2.2 and 1.2.3, the two main standard calibration sources, ThAr lamp and iodine cell, are not optimal. Their precision is limited to $\sim$1 m/s. However, a much better RV precision is required to find an Earth analogue, i.e. a 1 $M_\oplus$-mass planet at 1 AU distance from a solar-like star. The Earth induces just an RV amplitude of 9 cm/s to the Sun! The ultimate solution might be the Laser frequency comb which is potentially capable to provide a calibration precision of 1 cm/s (Murphy et al., 2007). A cm/s precision also opens the door to study phenomena totally different from exoplanets, e.g. the expansion of the universe or the variability of physical constants (Pasquini et al., 2010).

The Laser frequency comb is a technique which was awarded with the Nobel Prize in Physics in 2005 and was proposed as a new wavelength calibration source in astronomy (Murphy et al., 2007). It provides equally and accurately spaced calibration lines and is currently explored as a new wavelength calibration source for HARPS with a reported calibration precision of 9 cm/s (Wilken et al., 2010).

Table 5.1 lists several properties of an ideal calibration source and compares various calibration sources. The Laser comb obviously matches these properties best. So far however, the comb requires an expensive and complex system and covers only a small wavelength range. In the case of HARPS, it covers just one order of 72 orders (Wilken et al., 2010). The goal for the future will be to stabilise the construction and to broaden the frequency comb. One technical problem of the comb is the too dense spacing of the calibration lines which are not resolved by common spectrographs. As a solution Fabry-Perot cavities are implemented to suppress modes (Murphy et al., 2007; Li et al., 2008).

Frequency combs are also investigated for the near-infrared wavelength regime where appropriate wavelength calibrators are still missing. A precision of 1 m/s was reported with the astro-comb in the wavelength region of 7800–8800 Å for the TRES echelle spectrograph (Li et al., 2010).

The Fabry-Perot, which is required for the frequency comb, may receive a revival as a stand-alone calibration source (Sect. 1.2.4). The Fabry-Perot etalons provides also regulary spaced calibration lines and is adaptable over a wide wavelength range. It is also considered for HARPS and during one night a stability of 10 cm/s has been already demonstrated (Wildi et al., 2010). However, how to guarantee the long-term stability is still an open question. The FPI will surely need a vacuum enclosure and probably an additional calibration source, e.g. a Fourier transform spectrometer (Sect. 1.2.4), to track instrumental

drifts.

5.1.3 Stellar noise as the limiting factor?

The higher the precision, the more stars are variable. At a cm/s precision level probably all stars are intrinsically variable and it becomes more difficult to distinguish these variations from planetary signals. Stellar jitter is the obstacle in RV planet search. It is caused by oscillations, granulations, and other surface features (Sect. 4.4). For solar-like stars the noise can range from 1 m/s to several m/s which is one magnitude larger than the signal of an Earth analogue!

It is not yet clear, if the stellar jitter is a conquerable barrier. It is theoretically possible to detect amplitudes smaller than the noise. It requires a huge number of data points to get such a periodic signal significant in the presence of heavy, stochastic noise. New observing strategies propose to take three 10 min exposures, 2 h apart, to average out the oscillations (Dumusque et al., 2010). This already means tripling the observing time! However, one man's noise is another man's signal. Asteroseismologists will benefit in any case from these efforts and the new RV precision may improve our understanding of surface phenomena and stellar oscillations.

[2]Considering erratums in the Table of Murphy et al. (2007), we changed the entry for optical range coverage of the Etalon from no to yes (see Wildi et al. 2010 for the feasibility) and the entry for the long-term stability of the iodine cell from possibly to yes.

Bibliography

Agol, E., Steffen, J., Sari, R., & Clarkson, W. 2005, MNRAS, 359, 567, ADS (p. 7)

Anderson, D. R., Hellier, C., Gillon, M., et al. 2010, ApJ, 709, 159, ADS (p. 7)

Backer, D. C., Foster, R. S., & Sallmen, S. 1993, Nature, 365, 817, ADS (p. 5)

Bailey, J., Butler, R. P., Tinney, C. G., et al. 2009, ApJ, 690, 743, ADS (p. 38)

Baize, P. & Petit, M. 1989, A&AS, 77, 497, ADS (p. 74)

Balan, S. T. & Lahav, O. 2009, MNRAS, 394, 1936, ADS (p. 23)

Baliunas, S. L., Horne, J. H., Porter, A., et al. 1985, ApJ, 294, 310, ADS (p. 33)

Baluev, R. V. 2008, MNRAS, 385, 1279, ADS (p. 19)

Baranne, A., Queloz, D., Mayor, M., et al. 1996, A&AS, 119, 373, ADS (p. 13)

Barnes, J. R., Jeffers, S. V., & Jones, H. R. A. 2010, ArXiv e-prints, ADS (p. 104)

Barning, F. J. M. 1963, Bull. Astron. Inst. Netherlands, 17, 22, ADS (p. 15)

Bean, J. L., McArthur, B. E., Benedict, G. F., et al. 2007, AJ, 134, 749, ADS (p. 8, 11)

Bean, J. L., Seifahrt, A., Hartman, H., et al. 2010a, ApJ, 711, L19, ADS (p. 8)

—. 2010b, ApJ, 713, 410, ADS (p. 103, 104)

Beaulieu, J.-P., Bennett, D. P., Fouqué, P., et al. 2006, Nature, 439, 437, ADS (p. 39)

Beckers, J. M. 1976, Nature, 260, 227, ADS (p. 13)

Bedding, T. R., Kjeldsen, H., Arentoft, T., et al. 2007, ApJ, 663, 1315, ADS (p. 62)

Benedict, G. F., McArthur, B. E., Forveille, T., et al. 2002, ApJ, 581, L115, ADS (p. 8, 38)

Benedict, G. F., McArthur, B. E., Gatewood, G., et al. 2006, AJ, 132, 2206, ADS (p. 63)

Bennett, D. P., Rhie, S. H., Nikolaev, S., et al. 2010, ApJ, 713, 837, ADS (p. 9)

Bernstein, H.-H. 1997, in ESA Special Publication, Vol. 402, Hipparcos - Venice '97, ed. R. M. Bonnet, E. Høg, P. L. Bernacca, L. Emiliani, A. Blaauw, C. Turon, J. Kovalevsky, L. Lindegren, H. Hassan, M. Bouffard, B. Strim, D. Heger, M. A. C. Perryman, & L. Woltjer, 705–708, ADS (p. 54)

Beuermann, K., Hessman, F. V., Dreizler, S., et al. 2010, ArXiv e-prints, ADS (p. 9)

Beuzit, J.-L., Ségransan, D., Forveille, T., et al. 2004, A&A, 425, 997, ADS (p. 43, 54)

Bloemen, S., Marsh, T. R., Østensen, R. H., et al. 2010, MNRAS, 1640, ADS (p. 10)

Bond, I. A., Udalski, A., Jaroszyński, M., et al. 2004, ApJ, 606, L155, ADS (p. 8)

Bonfils, X., Forveille, T., Delfosse, X., et al. 2005, A&A, 443, L15, ADS (p. 38)

Bonfils, X., Mayor, M., Delfosse, X., et al. 2007, A&A, 474, 293, ADS (p. 38, 54, 55)

Borucki, W. J. & the Kepler Team. 2010, ArXiv e-prints, ADS (p. 7)

Boss, A. P. 2006, ApJ, 644, L79, ADS (p. 39)

Bouchy, F., Pepe, F., & Queloz, D. 2001, A&A, 374, 733, ADS (p. 12, 67, 75)

Breger, M., Handler, G., Garrido, R., et al. 1999, A&A, 349, 225, ADS (p. 30)

Bretthorst, G. L. 2001, in American Institute of Physics Conference Series, Vol. 568, Bayesian Inference and Maximum Entropy Methods in Science and Engineering, ed. A. Mohammad-Djafari, 241–245, ADS (p. 27)

Burgasser, A. J., Kirkpatrick, J. D., Cutri, R. M., et al. 2000, ApJ, 531, L57, ADS (p. 74)

Butler, R. P., Howard, A. W., Vogt, S. S., & Wright, J. T. 2009, ApJ, 691, 1738, ADS (p. 38, 103)

Butler, R. P., Johnson, J. A., Marcy, G. W., et al. 2006, PASP, 118, 1685, ADS (p. 38, 62, 78, 79)

Butler, R. P., Marcy, G. W., Williams, E., et al. 1996, PASP, 108, 500, ADS (p. 12, 13, 67)

Butler, R. P., Tinney, C. G., Marcy, G. W., et al. 2001, ApJ, 555, 410, ADS (p. 62)

Butler, R. P., Vogt, S. S., Marcy, G. W., et al. 2004, ApJ, 617, 580, ADS (p. 38)

Cameron, A. C., Bruce, V. A., Miller, G. R. M., Triaud, A. H. M. J., & Queloz, D. 2010a, MNRAS, 403, 151, ADS (p. 7)

Cameron, A. C., Guenther, E., Smalley, B., et al. 2010b, MNRAS, 407, 507, ADS (p. 7)

Campbell, B. & Walker, G. A. H. 1979, PASP, 91, 540, ADS (p. 13)

Campbell, B., Walker, G. A. H., & Yang, S. 1988, ApJ, 331, 902, ADS (p. 5, 13)

Charbonneau, D., Brown, T. M., Latham, D. W., & Mayor, M. 2000, ApJ, 529, L45, ADS (p. 7)

Charbonneau, D., Brown, T. M., Noyes, R. W., & Gilliland, R. L. 2002, ApJ, 568, 377, ADS (p. 7)

Chauvin, G., Lagrange, A., Dumas, C., et al. 2004, A&A, 425, L29, ADS (p. 6)

Cochran, W. D., Hatzes, A. P., & Hancock, T. J. 1991, ApJ, 380, L35, ADS (p. 5)

Cochran, W. D., Smith, H. J., & Smith, W. H. 1982, in Society of Photo-Optical Instrumentation Engineers (SPIE) Conference Series, Vol. 331, Society of Photo-Optical Instrumentation Engineers (SPIE) Conference Series, 315–+, ADS (p. 14)

Connes, P. 1985, Ap&SS, 110, 211, ADS (p. 12, 14, 67)

Cumming, A. 2004, MNRAS, 354, 1165, ADS (p. 19, 22, 25, 26, 49, 76)

Cumming, A., Butler, R. P., Marcy, G. W., et al. 2008, PASP, 120, 531, ADS (p. 25, 38, 62, 75, 83, 103)

Cumming, A., Marcy, G. W., & Butler, R. P. 1999, ApJ, 526, 890, ADS (p. 16, 18, 19, 26, 27, 34, 35, 43)

Delfosse, X., Forveille, T., Mayor, M., et al. 1998, A&A, 338, L67, ADS (p. 38, 55)

Delfosse, X., Forveille, T., Ségransan, D., et al. 2000, A&A, 364, 217, ADS (p. 39, 40)

Drake, J. J. & Smith, G. 1993, ApJ, 412, 797, ADS (p. 63)

Dravins, D., Lindegren, L., & Madsen, S. 1999, A&A, 348, 1040, ADS (p. 14)

Dravins, D., Lindegren, L., & Vandenberg, D. A. 1998, A&A, 330, 1077, ADS (p. 63)

Dumusque, X., Udry, S., Lovis, C., Santos, N. C., & Monteiro, M. J. F. P. G. 2010, ArXiv e-prints, ADS (p. 106)

Eggenberger, A., Udry, S., Chauvin, G., et al. 2007, A&A, 474, 273, ADS (p. 63, 74, 82)

Eiroa, C., Fedele, D., Maldonado, J., et al. 2010, A&A, 518, L131+, ADS (p. 83)

Endl, M., Cochran, W. D., Kürster, M., et al. 2006, ApJ, 649, 436, ADS (p. 38, 39, 55)

Endl, M., Cochran, W. D., Wittenmyer, R. A., & Boss, A. P. 2008, ApJ, 673, 1165, ADS (p. 38)

Endl, M. & Kürster, M. 2008, A&A, 488, 1149, ADS (p. 39, 47, 49, 54)

Endl, M., Kürster, M., & Els, S. 2000, A&A, 362, 585, ADS (p. 39, 67)

Endl, M., Kürster, M., Els, S., et al. 2002, A&A, 392, 671, ADS (p. 43, 49, 62, 64, 68, 69, 75, 78, 79, 82)

Favata, F., Micela, G., & Sciortino, S. 1997, A&A, 323, 809, ADS (p. 74)

Ferraz-Mello, S. 1981, AJ, 86, 619, ADS (p. 16, 26)

Figueira, P., Pepe, F., Lovis, C., & Mayor, M. 2010, A&A, 515, A106+, ADS (p. 104)

Ford, E. B. & Gregory, P. C. 2007, in Astronomical Society of the Pacific Conference Series, Vol. 371, Statistical Challenges in Modern Astronomy IV, ed. G. J. Babu & E. D. Feigelson, 189–+, ADS (p. 23)

Forveille, T., Bonfils, X., Delfosse, X., et al. 2009, A&A, 493, 645, ADS (p. 38)

Fröhlich, H. 2007, Astronomische Nachrichten, 328, 1037, ADS (p. 78)

Gaudi, B. S., Bennett, D. P., Udalski, A., et al. 2008, Science, 319, 927, ADS (p. 9)

Ge, J. 2002, ApJ, 571, L165, ADS (p. 14)

Ge, J., van Eyken, J., Mahadevan, S., et al. 2006, ApJ, 648, 683, ADS (p. 14)

Gilliland, R. L. & Baliunas, S. L. 1987, ApJ, 314, 766, ADS (p. 16)

Gilliland, R. L. & Fisher, R. 1985, PASP, 97, 285, ADS (p. 33)

Gillon, M., Pont, F., Demory, B.-O., et al. 2007, A&A, 472, L13, ADS (p. 38)

Gould, A. 1996, ApJ, 470, 201, ADS (p. 9)

Gould, A., Udalski, A., An, D., et al. 2006, ApJ, 644, L37, ADS (p. 9, 39)

Gray, D. F. 1988, Lectures on spectral-line analysis: F,G, and K stars, ed. Gray, D. F., ADS (p. 63)

Gray, R. O., Corbally, C. J., Garrison, R. F., et al. 2006, AJ, 132, 161, ADS (p. 90)

Grießmeier, J., Zarka, P., & Spreeuw, H. 2007, A&A, 475, 359, ADS (p. 9)

Griffin, M., Swinyard, B., Vigroux, L., et al. 2008, in Society of Photo-Optical Instrumentation Engineers (SPIE) Conference Series, Vol. 7010, Society of Photo-Optical Instrumentation Engineers (SPIE) Conference Series, ADS (p. 14)

Griffin, R. & Griffin, R. 1973, MNRAS, 162, 255, ADS (p. 12)

Guenther, E. W., Cabrera, J., Erikson, A., et al. 2010, ArXiv e-prints, ADS (p. 7)

Guinan, E. F. & Engle, S. G. 2009, ArXiv e-prints, ADS (p. 37)

Hajian, A. R., Behr, B. B., Cenko, A. T., et al. 2007, ApJ, 661, 616, ADS (p. 14)

Hatzes, A. P. & Cochran, W. D. 1999, MNRAS, 304, 109, ADS (p. 104)

Hatzes, A. P., Cochran, W. D., Endl, M., et al. 2003, ApJ, 599, 1383, ADS (p. 5)

Hatzes, A. P., Cochran, W. D., McArthur, B., et al. 2000, ApJ, 544, L145, ADS (p. 63, 78, 82, 85)

Hébrard, G., Bouchy, F., Pont, F., et al. 2008, A&A, 488, 763, ADS (p. 7)

Heintz, W. D. 1978, ApJ, 220, 931, ADS (p. 5, 74)

Hekker, S., Reffert, S., & Quirrenbach, A. 2006, Communications in Asteroseismology, 147, 121, ADS (p. 104)

Henry, T. J., Soderblom, D. R., Donahue, R. A., & Baliunas, S. L. 1996, AJ, 111, 439, ADS (p. 90)

Hoffleit, D. & Jaschek, C. 1991, The Bright star catalogue, ed. Hoffleit, D. & Jaschek, C., ADS (p. 62, 63)

Holman, M. J. & Murray, N. W. 2005, Science, 307, 1288, ADS (p. 7)

Horne, J. H. & Baliunas, S. L. 1986, ApJ, 302, 757, ADS (p. 18)

Horne, K. 1986, PASP, 98, 609, ADS (p. 65)

Hünsch, M., Schmitt, J. H. M. M., Sterzik, M. F., & Voges, W. 1999, A&AS, 135, 319, ADS (p. 39)

Ida, S. & Lin, D. N. C. 2005, ApJ, 626, 1045, ADS (p. 39)

Ingrosso, G., Novati, S. C., de Paolis, F., et al. 2009, MNRAS, 399, 219, ADS (p. 9)

Irwin, A. W., Campbell, B., Morbey, C. L., Walker, G. A. H., & Yang, S. 1989, PASP, 101, 147, ADS (p. 16)

Irwin, J., Buchhave, L., Berta, Z. K., et al. 2010, ApJ, 718, 1353, ADS (p. 103)

Irwin, J., Charbonneau, D., Nutzman, P., & Falco, E. 2009, 253, 37, ADS (p. 55)

Isaacson, H. & Fischer, D. A. 2010, ArXiv e-prints, ADS (p. 70, 90)

Janson, M., Apai, D., Zechmeister, M., et al. 2009, MNRAS, 399, 377, ADS (p. 83)

Janson, M., Bergfors, C., Goto, M., Brandner, W., & Lafrenière, D. 2010, ApJ, 710, L35, ADS (p. 6)

Jefferys, W. H., Fitzpatrick, M. J., & McArthur, B. E. 1988, Celestial Mechanics, 41, 39, ADS (p. 78)

Johnson, J. A., Apps, K., Gazak, J. Z., et al. 2010, ArXiv e-prints, ADS (p. 103)

Johnson, J. A., Butler, R. P., Marcy, G. W., et al. 2007, ApJ, 670, 833, ADS (p. 38)

Jones, H. R. A., Butler, R. P., Tinney, C. G., et al. 2006, MNRAS, 369, 249, ADS (p. 25)

Jones, H. R. A., Butler, R. P., Tinney, C. G., et al. 2004, in Astronomical Society of the Pacific Conference Series, Vol. 321, Extrasolar Planets: Today and Tomorrow, ed. J. Beaulieu, A. Lecavelier Des Etangs, & C. Terquem, 298–+, ADS (p. 62)

Kalas, P., Graham, J. R., Chiang, E., et al. 2008, Science, 322, 1345, ADS (p. 6, 9)

Kallinger, T., Reegen, P., & Weiss, W. W. 2008, A&A, 481, 571, ADS (p. 30, 33)

Kasting, J. F., Whitmire, D. P., & Reynolds, R. T. 1993, Icarus, 101, 108, ADS (p. 38, 50, 51)

King, R. R., McCaughrean, M. J., Homeier, D., et al. 2010, A&A, 510, A99+, ADS (p. 74)

Knutson, H. A., Charbonneau, D., Allen, L. E., et al. 2007, Nature, 447, 183, ADS (p. 7)

Koen, C. 1990, ApJ, 348, 700, ADS (p. 18)

Kovacs, G. 1981, Ap&SS, 78, 175, ADS (p. 33)

Kozhevatov, I. E., Kulikova, E. K., & Cheragin, N. P. 1995, Astronomy Letters, 21, 418, ADS (p. 14)

Kürster, M., Endl, M., Els, S., et al. 2000, A&A, 353, L33, ADS (p. 62, 77, 78, 82, 103)

Kürster, M., Endl, M., & Reffert, S. 2008, A&A, 483, 869, ADS (p. 11, 23, 42, 47, 103)

Kürster, M., Endl, M., Rouesnel, F., et al. 2003, A&A, 403, 1077, ADS (p. 39, 47, 50, 54, 71)

Kürster, M., Schmitt, J. H. M. M., Cutispoto, G., & Dennerl, K. 1997, A&A, 320, 831, ADS (p. 47)

Latham, D. W., Stefanik, R. P., Mazeh, T., Mayor, M., & Burki, G. 1989, Nature, 339, 38, ADS (p. 5)

Laughlin, G., Bodenheimer, P., & Adams, F. C. 2004, ApJ, 612, L73, ADS (p. 38)

Leinert, C., Henry, T., Glindemann, A., & McCarthy, Jr., D. W. 1997, A&A, 325, 159, ADS (p. 54)

Lendl, M., Afonso, C., Koppenhoefer, J., et al. 2010, A&A, 522, A29+, ADS (p. 7)

Li, C., Benedick, A. J., Fendel, P., et al. 2008, Nature, 452, 610, ADS (p. 105)

Li, C., Phillips, D. F., Glenday, A. G., et al. 2010, in Society of Photo-Optical Instrumentation Engineers (SPIE) Conference Series, Vol. 7735, Society of Photo-Optical Instrumentation Engineers (SPIE) Conference Series, ADS (p. 105)

Liebig, C. & Wambsganss, J. 2010, A&A, 520, A68+, ADS (p. 9)

Liseau, R., Eiroa, C., Fedele, D., et al. 2010, A&A, 518, L132+, ADS (p. 83)

Lomb, N. R. 1976, Ap&SS, 39, 447, ADS (p. 15, 16, 18, 27)

Lovis, C., Mayor, M., Pepe, F., et al. 2006, Nature, 441, 305, ADS (p. 14, 63, 76, 77, 78, 82, 103)

Lovis, C. & Pepe, F. 2007, A&A, 468, 1115, ADS (p. 13)

Luyten, W. J. & Hughes, H. S. 1980, Proper motion survey with the forty-eight inch Schmidt telescope. LV. First supplement to the NLTT catalogue., by Luyten, W. J.; Hughes, H. S.. Sep. print University of Minnesota, Minneapolis, MN (USA), 16 p., 55, 1, ADS (p. 74)

Maciejewski, G., Dimitrov, D., Neuhaeuser, R., et al. 2010, ArXiv e-prints, ADS (p. 7)

Marcy, G. W. & Butler, R. P. 1992, PASP, 104, 270, ADS (p. 13)

Marcy, G. W. & Butler, R. P. 1995, in Bulletin of the American Astronomical Society, Vol. 27, Bulletin of the American Astronomical Society, 1379–+, ADS (p. 5)

Marcy, G. W., Butler, R. P., Fischer, D., et al. 2001, ApJ, 556, 296, ADS (p. 38, 55)

Marcy, G. W., Butler, R. P., Vogt, S. S., Fischer, D., & Lissauer, J. J. 1998, ApJ, 505, L147, ADS (p. 38, 55)

Marcy, G. W., Butler, R. P., Vogt, S. S., et al. 2008, Physica Scripta Volume T, 130, 014001, ADS (p. 62)

Marcy, G. W., Butler, R. P., Williams, E., et al. 1997, ApJ, 481, 926, ADS (p. 5)

Marois, C., Macintosh, B., Barman, T., et al. 2008, Science, 322, 1348, ADS (p. 6)

Mason, B. D., Wycoff, G. L., Hartkopf, W. I., Douglass, G. G., & Worley, C. E. 2001, AJ, 122, 3466, ADS (p. 74)

Mayor, M., Bonfils, X., Forveille, T., et al. 2009a, A&A, 507, 487, ADS (p. 38, 103)

Mayor, M., Pepe, F., Queloz, D., et al. 2003, The Messenger, 114, 20, ADS (p. 13, 66)

Mayor, M. & Queloz, D. 1995, Nature, 378, 355, ADS (p. 5, 6, 13, 62)

Mayor, M., Udry, S., Lovis, C., et al. 2009b, A&A, 493, 639, ADS (p. 14)

McCarthy, C. & Zuckerman, B. 2004, AJ, 127, 2871, ADS (p. 54)

McLaughlin, D. B. 1924, ApJ, 60, 22, ADS (p. 7)

McMillan, R. S., Moore, T. L., Perry, M. L., & Smith, P. H. 1994, Ap&SS, 212, 271, ADS (p. 14)

McMillan, R. S., Smith, P. H., Perry, M. L., Moore, T. L., & Merline, W. J. 1990, in Society of Photo-Optical Instrumentation Engineers (SPIE) Conference Series, Vol. 1235, Society of Photo-Optical Instrumentation Engineers (SPIE) Conference Series, ed. D. L. Crawford, 601–609, ADS (p. 14)

Metcalfe, T. S., Basu, S., Henry, T. J., et al. 2010, ApJ, 723, L213, ADS (p. 79, 81)

Montgomery, M. H. & Odonoghue, D. 1999, Delta Scuti Star Newsletter, 13, 28, ADS (p. 30, 32, 33)

Moya, A., Amado, P. J., Barrado, D., et al. 2010, MNRAS, 405, L81, ADS (p. 6)

Murakami, N., Kawada, M., Takahashi, H., et al. 2010, PASJ, 62, 1155, ADS (p. 14)

Murphy, M. T., Udem, T., Holzwarth, R., et al. 2007, MNRAS, 380, 839, ADS (p. 105, 106)

Naef, D., Mayor, M., Beuzit, J., et al. 2005, in ESA Special Publication, Vol. 560, 13th Cambridge Workshop on Cool Stars, Stellar Systems and the Sun, ed. F. Favata, G. A. J. Hussain, & B. Battrick, 833–+, ADS (p. 62, 82)

Naef, D., Mayor, M., Korzennik, S. G., et al. 2003, A&A, 410, 1051, ADS (p. 62)

Naef, D., Mayor, M., Lo Curto, G., et al. 2010, A&A, 523, A15+, ADS (p. 62)

Naef, D., Mayor, M., Pepe, F., et al. 2001, A&A, 375, 205, ADS (p. 62, 78)

Nakajima, T., Oppenheimer, B. R., Kulkarni, S. R., et al. 1995, Nature, 378, 463, ADS (p. 47, 54)

Nelson, A. F. & Angel, J. R. P. 1998, ApJ, 500, 940, ADS (p. 49)

Neuhäuser, R., Guenther, E. W., Wuchterl, G., et al. 2005, A&A, 435, L13, ADS (p. 6)

Ohta, Y., Taruya, A., & Suto, Y. 2005, ApJ, 622, 1118, ADS (p. 7)

O'Toole, S. J., Butler, R. P., Tinney, C. G., et al. 2007, ApJ, 660, 1636, ADS (p. 23)

O'Toole, S. J., Jones, H. R. A., Tinney, C. G., et al. 2009a, ApJ, 701, 1732, ADS (p. 62)

O'Toole, S. J., Tinney, C. G., Jones, H. R. A., et al. 2009b, MNRAS, 392, 641, ADS (p. 23, 24, 25, 26)

Pasquini, L., Cristiani, S., Garcia-Lopez, R., Haehnelt, M., & Mayor, M. 2010, The Messenger, 140, 20, ADS (p. 105)

Pelt, J. 2009, Baltic Astronomy, 18, 83, ADS (p. 47)

Pepe, F., Mayor, M., Queloz, D., et al. 2004, A&A, 423, 385, ADS (p. 66)

Perryman, M. A. C., Lindegren, L., Kovalevsky, J., et al. 1997, A&A, 323, L49, ADS (p. 63, 90)

Pourbaix, D., Nidever, D., McCarthy, C., et al. 2002, A&A, 386, 280, ADS (p. 63, 79, 87)

Poveda, A., Herrera, M. A., Allen, C., Cordero, G., & Lavalley, C. 1994, Revista Mexicana de Astronomia y Astrofisica, 28, 43, ADS (p. 74)

Pravdo, S. H. & Shaklan, S. B. 2009, ApJ, 700, 623, ADS (p. 8)

Press, W. H. & Rybicki, G. B. 1989, ApJ, 338, 277, ADS (p. 18)

Press, W. H., Teukolsky, S. A., Vetterling, W. T., & Flannery, B. P. 1992, Numerical recipes in FORTRAN. The art of scientific computing (Cambridge: University Press, |c1992, 2nd ed.), ADS (p. 18)

Quillen, A. C. & Thorndike, S. 2002, ApJ, 578, L149, ADS (p. 9, 83)

Quirrenbach, A., Amado, P. J., Mandel, H., et al. 2010, in Society of Photo-Optical Instrumentation Engineers (SPIE) Conference Series, Vol. 7735, Society of Photo-Optical Instrumentation Engineers (SPIE) Conference Series, ADS (p. 104)

Ramsey, L. W., Barnes, J., Redman, S. L., et al. 2008, PASP, 120, 887, ADS (p. 104)

Ramsey, L. W., Mahadevan, S., Redman, S., et al. 2010, in Society of Photo-Optical Instrumentation Engineers (SPIE) Conference Series, Vol. 7735, Society of Photo-Optical Instrumentation Engineers (SPIE) Conference Series, ADS (p. 104)

Reegen, P. 2007, A&A, 467, 1353, ADS (p. 16, 20, 21, 27, 33)

Reiners, A., Bean, J. L., Huber, K. F., et al. 2010, ApJ, 710, 432, ADS (p. 104)

Rivera, E. J., Butler, R. P., Vogt, S. S., et al. 2010, ApJ, 708, 1492, ADS (p. 68)

Rivera, E. J., Lissauer, J. J., Butler, R. P., et al. 2005, ApJ, 634, 625, ADS (p. 38, 55)

Rodler, F., Kürster, M., & Henning, T. 2010, A&A, 514, A23+, ADS (p. 9)

Rossiter, R. A. 1924, ApJ, 60, 15, ADS (p. 7)

Santos, N. C., Mayor, M., Naef, D., et al. 2002, A&A, 392, 215, ADS (p. 103)

Scargle, J. D. 1982, ApJ, 263, 835, ADS (p. 15, 18, 21)

Schlesinger, F. 1910, Publications of the Allegheny Observatory of the University of Pittsburgh, 1, 123, ADS (p. 7)

—. 1917, AJ, 30, 137, ADS (p. 71)

Scholz, R., McCaughrean, M. J., Lodieu, N., & Kuhlbrodt, B. 2003, A&A, 398, L29, ADS (p. 74)

Ségransan, D., Udry, S., Mayor, M., et al. 2010, A&A, 511, A45+, ADS (p. 62)

Seifahrt, A., Käufl, H. U., Zängl, G., et al. 2010, ArXiv e-prints, ADS (p. 104)

Shkolnik, E., Walker, G. A. H., & Bohlender, D. A. 2003, ApJ, 597, 1092, ADS (p. 10)

Shrager, R. I. 2001, Ap&SS, 277, 519, ADS (p. 16)

Silvotti, R., Schuh, S., Janulis, R., et al. 2007, Nature, 449, 189, ADS (p. 9)

Simon, A., Szatmáry, K., & Szabó, G. M. 2007, A&A, 470, 727, ADS (p. 7)

Sion, E. M., Greenstein, J. L., Landstreet, J. D., et al. 1983, ApJ, 269, 253, ADS (p. 9)

Snellen, I. A. G., Albrecht, S., de Mooij, E. J. W., & Le Poole, R. S. 2008, A&A, 487, 357, ADS (p. 7)

Snellen, I. A. G., de Kok, R. J., de Mooij, E. J. W., & Albrecht, S. 2010, Nature, 465, 1049, ADS (p. 7)

Standish, Jr., E. M. 1990, A&A, 233, 252, ADS (p. 12, 68)

Strand, K. A. 1943, PASP, 55, 29, ADS (p. 5)

—. 1957, AJ, 62, 35, ADS (p. 5)

Struve, O. 1952, The Observatory, 72, 199, ADS (p. 5)

Swain, M. R., Vasisht, G., & Tinetti, G. 2008, Nature, 452, 329, ADS (p. 7)

Teixeira, T. C., Kjeldsen, H., Bedding, T. R., et al. 2009, A&A, 494, 237, ADS (p. 62, 63)

Thalmann, C., Carson, J., Janson, M., et al. 2009, ApJ, 707, L123, ADS (p. 6)

Thorsett, S. E., Arzoumanian, Z., & Taylor, J. H. 1993, ApJ, 412, L33, ADS (p. 5)

Tinetti, G., Vidal-Madjar, A., Liang, M., et al. 2007, Nature, 448, 169, ADS (p. 7)

Udry, S., Bonfils, X., Delfosse, X., et al. 2007, A&A, 469, L43, ADS (p. 38, 55)

Valdivielso, L., Esparza, P., Martín, E. L., Maukonen, D., & Peale, R. E. 2010, ApJ, 715, 1366, ADS (p. 104)

van de Kamp, P. 1963, AJ, 68, 515, ADS (p. 5)

van Kerkwijk, M. H., Rappaport, S. A., Breton, R. P., et al. 2010, ApJ, 715, 51, ADS (p. 10)

van Leeuwen, F. 2007, A&A, 474, 653, ADS (p. 40, 43, 44, 63)

Vaníček, P. 1971, Ap&SS, 12, 10, ADS (p. 27)

Vauclair, S., Laymand, M., Bouchy, F., et al. 2008, A&A, 482, L5, ADS (p. 62, 63)

Vogt, S. S., Butler, R. P., Rivera, E. J., et al. 2010, ApJ, 723, 954, ADS (p. 13, 68, 103)

Walker, G. A. H. 2008, ArXiv e-prints, ADS (p. 5)

Walker, G. A. H., Bohlender, D. A., Walker, A. R., et al. 1992, ApJ, 396, L91, ADS (p. 5)

Walker, G. A. H., Walker, A. R., Irwin, A. W., et al. 1995, Icarus, 116, 359, ADS (p. 13, 27, 62)

Wambsganss, J. 2006, Gravitational Microlensing, ed. Schneider, P., Kochanek, C. S., & Wambsganss, J., 453–+, ADS (p. 8)

Wildi, F., Pepe, F., Chazelas, B., Lo Curto, G., & Lovis, C. 2010, in Society of Photo-Optical Instrumentation Engineers (SPIE) Conference Series, Vol. 7735, Society of Photo-Optical Instrumentation Engineers (SPIE) Conference Series, ADS (p. 105, 106)

Wilken, T., Lovis, C., Manescau, A., et al. 2010, in Society of Photo-Optical Instrumentation Engineers (SPIE) Conference Series, Vol. 7735, Society of Photo-Optical Instrumentation Engineers (SPIE) Conference Series, ADS (p. 105)

Winn, J. N. 2010, ArXiv e-prints, ADS (p. 8)

Winn, J. N., Howard, A. W., Johnson, J. A., et al. 2010, ArXiv e-prints, ADS (p. 7)

Wittenmyer, R. A., Endl, M., Cochran, W. D., et al. 2006, AJ, 132, 177, ADS (p. 62, 68)

Wolszczan, A. 1994, Science, 264, 538, ADS (p. 5)

Wolszczan, A. & Frail, D. A. 1992, Nature, 355, 145, ADS (p. 5)

Worley, C. E. & Douglass, G. G. 1997, A&AS, 125, 523, ADS (p. 74)

Wright, J. T., Marcy, G. W., Butler, R. P., & Vogt, S. S. 2004, ApJS, 152, 261, ADS (p. 90)

Wright, J. T., Marcy, G. W., Butler, R. P., et al. 2008, ApJ, 683, L63, ADS (p. 62)

Zechmeister, M. & Kürster, M. 2009, A&A, 496, 577, ADS (p. 14, 47, 55, 56, 75)

Zechmeister, M., Kürster, M., & Endl, M. 2009, A&A, 505, 859, ADS (p. 14, 58, 62, 71, 81)

Acknowledgement

First of all, I would like to thank Dr. Martin Kürster for his excellent support and guidance. He provided all the valuable data sets analysed in this work. It was a great pleasure for me to work under his supervision. He gave me many useful advice, practised patiently presentations with me, and was always open for questions and discussions.

Prof. Th. Henning and Prof. J. Wamsganß are gratefully acknowledged for being the referees of this thesis.

Hubert Klahr and Mario Trieloff kindly agreed to be members of my examination committee.

I also want to express my graditude to Dr. Michael Endl for the introduction in his Austral code and his hospitality during my stay in Austin, Texas.

I enjoyed always the scientific discussions at the MPIA, especially with Tim Hartung-Schulze, Ralf Launhardt, Johny Setiawan, Viki Jörgens, and Wolfgang Brandner.

I'm thankful to the STAC (Strategic Time Allocation Committee) of the MPIA for generous allocation of FEROS time for follow-up observations. This gave me the opportunity to visit four times the La Silla observatory in Chile.

My former and present room mates Benjamin Moster, Florian Rodler, Kerstin Geißler, Andreas Schruba, Xianyu Zhang, and Marcus Mellein provided a very pleasant office atmosphere.

Ulrich Hiller and Marco Piroth were always very supportive when I had software or hardware problems.

Finally, I thank my wife Bożena and my family for their care and daily support.

Erklärung

Ich versichere, dass ich diese Arbeit selbständig verfasst und keine anderen als die angegebenen Quellen und Hilfsmittel benutzt habe.

Heidelberg, den _____ _____

(Mathias Zechmeister)